AFFDL-TR-78-182
Part I

LEVEL

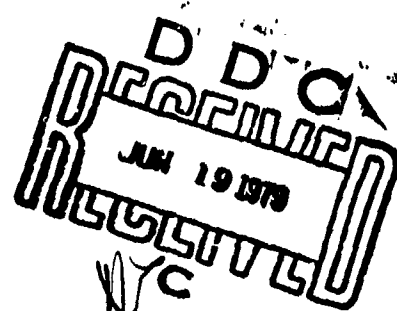$A070128$

FUEL TANK SURVIVABILITY FOR HYDRODYNAMIC RAM INDUCED BY
HIGH-VELOCITY FRAGMENTS:

Part I. Experimental Results and Design Summary

UNIVERSITY OF DAYTON RESEARCH INSTITUTE
300 COLLEGE PARK AVENUE
DAYTON, OHIO 45469

JANUARY 1979

TECHNICAL REPORT AFFDL-TR-78-182, PART I
FINAL REPORT FOR PERIOD SEPTEMBER 1977 – OCTOBER 1978

APPROVED FOR PUBLIC RELEASE – DISTRIBUTION UNLIMITED

AIR FORCE FLIGHT DYNAMICS LABORATORY
AIR FORCE WRIGHT AERONAUTICAL LABORATORIES
AIR FORCE SYSTEMS COMMAND
WRIGHT-PATTERSON AIR FORCE BASE, OHIO 45433

WILLIAM E. HACKENBERGER
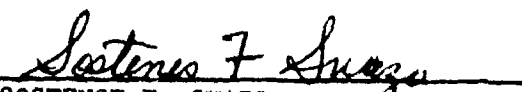Project Engineer/Technical Monitor

SOSTENSE F. SUAZO, Lt Col, USAF
Chief, Flight Vehicle Protection Br.
Vehicle Equipment Division

FOR THE COMMANDER

AMBROSE B. NUTT
Director
Vehicle Equipment Division

REPORT DOCUMENTATION PAGE

READ INSTRUCTIONS
BEFORE COMPLETING FORM

1. REPORT NUMBER	2. GOVT ACCESSION NO.	3. RECIPIENT'S CATALOG NUMBER
AFFDL-TR-78-182, PART I		

4. TITLE (and Subtitle)

FUEL TANK SURVIVABILITY FOR HYDRODYNAMIC RAM INDUCED BY HIGH VELOCITY FRAGMENTS: Part I, Experimental Results and Design Summary

5. TYPE OF REPORT & PERIOD COVERED

Final Report
Sept 1977 - Oct 1978

6. PERFORMING ORG. REPORT NUMBER

UDR-TR-78-115-PT-1

7. AUTHOR(s)

S. J. Bless

8. CONTRACT OR GRANT NUMBER(s)

F33615-77-C-2082

9. PERFORMING ORGANIZATION NAME AND ADDRESS

University of Dayton Research Institute
300 College Park
Dayton, Ohio 45469

10. PROGRAM ELEMENT, PROJECT, TASK AREA & WORK UNIT NUMBERS

Project No. 2402
Task No. 02
Work Unit No. 24020218

11. CONTROLLING OFFICE NAME AND ADDRESS

Air Force Flight Dynamics Laboratory
Air Force Systems Command
Wright-Patterson Air Force Base OH 45433

12. REPORT DATE

January 1979

13. NUMBER OF PAGES

112

14. MONITORING AGENCY NAME & ADDRESS(If different from Controlling Office)

15. SECURITY CLASS (of this report)

Unclassified

15a. DECLASSIFICATION DOWNGRADING SCHEDULE

16. DISTRIBUTION STATEMENT (of this Report)

Approved for Public Release - Distribution Unlimited

17. DISTRIBUTION STATEMENT (of the abstract entered in Block 20, if different from Report)

18. SUPPLEMENTARY NOTES

19. KEY WORDS (Continue on reverse side if necessary and identify by block number)

Hydrodynamic Ram, Fuel Tank Vulnerability, High-Velocity Fragments, Terminal Ballistics

20. ABSTRACT (Continue on reverse side if necessary and identify by block number)

Failure data, displacement data, and pressure data were obtained from laboratory experiments. Panels were made from 7075-T6 and 2024-T3 aluminum and from graphite epoxy; panel thicknesses were 1.6 to 6.35 mm. Protection included 10-mm-ballistic foam and stiffeners. Projectiles were 5.6-g and 11.7-g spheres and cubes.

Failures were always catastrophic, and failure thresholds were always abrupt. When cracks formed, they ran across the panels,

DD FORM 1473 EDITION OF 1 NOV 65 IS OBSOLETE

20. ABSTRACT (cont'd)

except when stiffeners were present. In thin panels, cracks
initiated at the corners of the perforation when cubical fragments
were used. The entrance panel damage was primarily induced by
the shock wave generated by the impact. The very high shock
pressure resulted in impulsive loading of the panels that caused
prompt crack formation. Cracks were propagated by the displace-
ment field. The dependence of failure on impact parameters could
be approximately represented as $V^2 D/W$ = constant, where V is pro-
jectile velocity, D is projectile diameter, and W is panel thick-
ness. Stiffeners and foam suppressed catastrophic crack formation.

Results were compared with finite difference (CRALE) and finite
element (NONSAP) calculations. CRALE was able to calculate
pressure caused by shock and drag forces on the projectile. A
simplified loading model based on the details of the CRALE results
was developed. When NONSAP was driven by the simplified loading
model, neither displacement nor failure thresholds were correctly
predicted. The error in displacement was attributed to neglect
of late-time water resistance to panel slow down and rebound.

Design data that included failure criteria and pressure loading
were generated for all configurations studied. The failure data
were based on experimental results, but numerical results were
used to aid interpolation and extrapolation. The pressure loading
functions were based on an analytic fit to the numerical results.
Failure of stiffened panels was defined by stiffener crushing.

PREFACE

The program described in this report was carried out for the Survivability/Vulnerability Branch of the Flight Vehicle Equipment Division (AFFDL/FES) of the Air Force Flight Dynamics Laboratory (AFFDL), Wright-Patterson AFB, Ohio. Most of the work was done under Contract F33615-77-C-2082. The Work Unit Title was "Aircraft Fuel Tank Wall Responses to Hydrodynamic Pressures", Number 24020218. Mr. William E. Hackenberger was the monitor for that contract. The experiments with graphite epoxy panels were mostly sponsored under Contract F33615-76-C-3076, Request 45. Mr. Andre Holten, AFFDL, was the Technical Monitor for that effort.

Many members of the staff of the University of Dayton Research Institute contributed to this program. Dr. Stephan Bless served as Principal Investigator. The experiments were executed under the supervision of Mr. Michael Nagy. Mr. Andrew Piekutowski was responsible for the improved moiré fringe set-up and analysis. Dr. John Barber was responsible for technical oversight, and Mr. Hallock Swift was Project Supervisor.

Accession For

NTIS GRA&I
DDC TAB
Unannounced
Justification

By
Distribution/
Availability Codes
Avail and/or
special

iii

TABLE OF CONTENTS

LIST OF ILLUSTRATIONS

LIST OF ILLUSTRATIONS (cont'd)

LIST OF ILLUSTRATIONS (cont'd)

LIST OF ILLUSTRATIONS (cont'd)

x

LIST OF TABLES

SYMBOLS AND UNITS

The primary units used in this report are a combination of cgs and SI units that is commonly used in impact physics. The unit of pressure in the bar, defined as 10^6 dyne/cm^2. One bar is very nearly one atmosphere, so that pressure, expressed in bars, is numerically equal to the ratio of actual pressure to initial pressure. A list of conversions to SI and English units appear below.

Quantity	This Report	SI	English
velocity	km/s (mm/ s)	1 km/s	3281 ft/s
stress (pressure)	bars (kbars)	0.1 MN/m^2	14.5 psi
length	mm (cm, m)	1 mm	0.039 in.
mass	g	10^{-3} kg	15.43 grains
density	g/cm^3	1000 kg/m^3	62.4 lb/ft^3
area impulse	bar-s	10^5 kg/ms	14.5 psi-s

Shot configurations are referred to by abbreviations in this report. The key to this nomenclature is given in Table III of the text.

The following symbols are used in equations:

a	acceleration
A	presented area of the projectile
A_h	area of the impact hole
A_H	Hugoniot pressure increment per increment in impact velocity
C	shock speed in water
C_p	shock speed in projectile
d	diameter of the impact hole
D	diameter of a spherical projectile, edge dimension
F	failure constant of a cubical projectile
I	impulse
L_p	panel width
P	pressure
P_H	Hugoniot pressure
P_m	maximum pressure
r	radial coordinate in a cylindrical coordinate system centered on the impact
R_p	radius of a spherical projectile of mass equal to that of the actual projectile
t	time, shock
u	particle velocity
u_H	peak shock particle velocity from 1-D impact
u_z	displacement displacement in z direction
V	impact velocity
V_F	velocity at which panel failure occurs
W	panel thickness
z	axial coordinate in a cylindrical coordinate system centered on the impact, positive into the tank
δ	small displacement
ϵ	strain
ϵ_Θ	hoop strain
ρ	projectile density

ρ_t target panel density

σ_r radial stress

σ_θ hoop stress

SECTION I

INTRODUCTION

The design of fuel tanks for combat aircraft must take into account hydrodynamic ram phenomena. Fuel system hits are the largest single cause of aircraft loss in combat, and hydrodynamic ram is the primary damage mechanism when liquid-filled structures are penetrated by projectiles.

Hydrodynamic ram phenomena are varied and depend on threat and target parameters. In particular, there are three essentially different classes of threats: gun-launched KE projectiles, gun-launched HE projectiles, and high-velocity fragments. The effects of these projectiles are different for each of the three types of target subjects: entrance panels, side panels, and exit panels. In general, relatively slow and massive gun launched KE projectiles pose the greatest threat to exit panels. HE projectiles, depending on where they detonate, may impose severe loads on any panel. On the otherhand, high-velocity fragments principally damage entrance panels; exit panel damage only occurs when a relatively large number of fragments strike a relatively shallow tank.

Hydrodynamic ram phenomena have been subjected to vigorous study in recent years. A summary of most results through 1976 can be found in Reference 1.

Herein we report experimental and analytical results concerning damage of entrance panels by high-velocity fragments. The principal objectives of the program were to develop a design methodology and prepare design guidelines for fuel tank entrance panels. The threats considered were cubes and spheres ranging in mass from 5.6 g to 11.6 g (90 to 180 grains). Target panels were representative of present and planned designs, viz. plain, foam-backed, and stiffened 2024-T3 and 7075-T6 aluminum.

1

Panel thickness varied from 1.6 mm (1/16-inch) to 6.35 mm
(1/4-inch.)

The technical approach consisted of carefully coordinated
numerical analyses and experiments. In the analyses, a finite
difference code was used to calculate the pressure at the
liquid-panel interface. The derived loading functions were
then used to drive a finite element model of the entrance
panel. The result has been a greatly improved physical under-
standing of the panel damage mechanism and predictions of panel
failure and displacement.

The experiments were designed to calibrate and validate
the numerical models, as well as to provide "hard" data on
which to base design curves. The targets were instrumented
in order to obtain pressure and displacement data for compari-
son with code calculations.

The University of Dayton was responsible for program
management, conduct of experiments, interpretation of experi-
mental and numerical results, and generation of design data.
California Research and Technology, Inc. (CRT) was responsible
for the numerical modelling.

Part I of this report was prepared by the University.
Section II of Part I describes the experiments from a functional
point of view, and Appendix A and Reference 2 present a further
description of the laboratory and data analysis techniques.
Section III summarizes and discusses the results of the experi-
ments. Section IV summarizes the analytical results and
compares them with the experiments. Section V presents a
synthesis of the experimental and numerical work in order to
produce design guidelines. Section VI presents a summary of
results and conclusions. A series of graphs is included to
aid designers of damage-tolerant fuel tanks.

Part II of this report describes the numerical approaches
in detail. In Part II, the numerical data are analyzed and
compared with the experiments in order to obtain an improved
physical understanding of hydrodynamic ram phenomena.

SECTION II
EXPERIMENTAL CONFIGURATION

The experiments consisted of single impacts of gun-
launched projectiles into water-backed panels. Most shots
were well instrumented; data were obtained for pressure behind the
panels, dynamic displacement, and failure modes. The projectiles
were cubes and spheres. Details of the experimental apparatus
and data reduction techniques are given in Appendix A. Below
we describe the features of the experiments most relevant to
the interpretation of results.

2.1 BALLISTICS

The dimensions of the projectiles are given in Table I.
The tolerance on the mass was ±0.05 g. Sabots were serrated
Lexan®. Flash radiographs were used to measure velocity and
to verify the integrity and orientation of the projectiles
prior to impact. Rotation of the cubical projectiles during
free flight was minimal.

2.2 TARGET CONSTRUCTION

The targets were panel. fastened over a cut out in the
front of a 0.8 m^3 water-filled tank. Figure 2.1 provides a
drawing of the structure of the tank. One side of the tank
and the rear panel were 1.6-mm-thick aluminum, and the other
side was 12.7-mm aluminum. The top was open, and the bottom
rested on a 12.7-mm plywood sheet. The front of the tank,
minus the target panel, is shown in Figure 2.2. The mounting
plate was 12.7-mm-thick aluminum. The edge dimension of the
cut out was 51 cm. The mounting holes were 3/8 inch, and the
distance between bolt centers was 63.5 cm.

In all of the shots prefaced by FD, except those against
the graphite epoxy panels, the target panels were aluminum
sheets bolted directly to the mounting plate. The edge

3

TABLE 1.   PROJECTILE DESCRIPTIONS

Large Projectiles	Weight[*] (g)	Edge or Diameter (mm)
Cube	11.67	11.41
Sphere	11.89	14.25
Small Projectiles		
Cube	5.66	8.97
Sphere	5.59	11.08

[*]11.67 g = 180 grains
 11.89 g = 183 grains
  5.66 g = 87 grains
  5.59 g = 86 grains
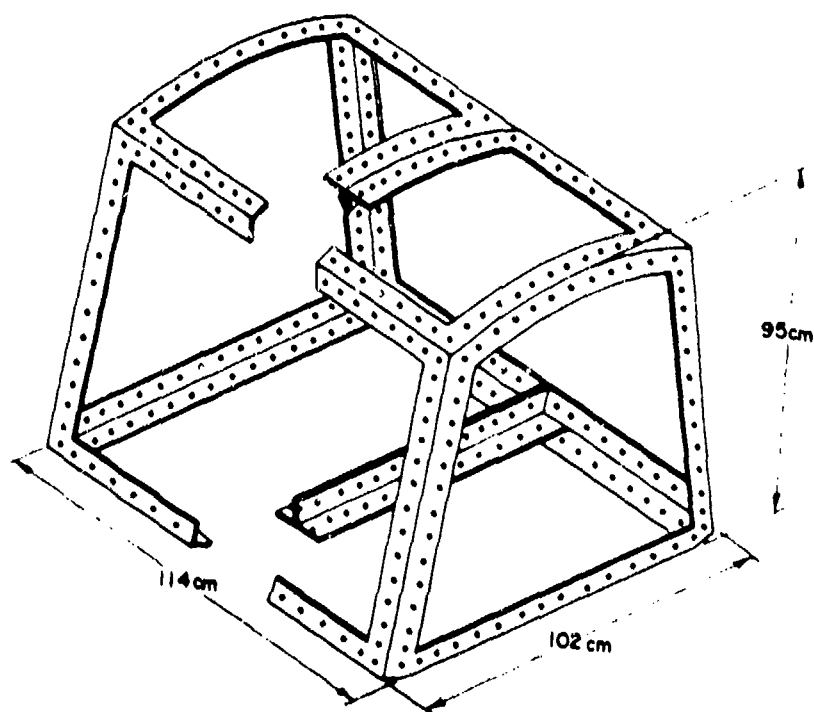
Figure 2.1.   Frame of target tank.
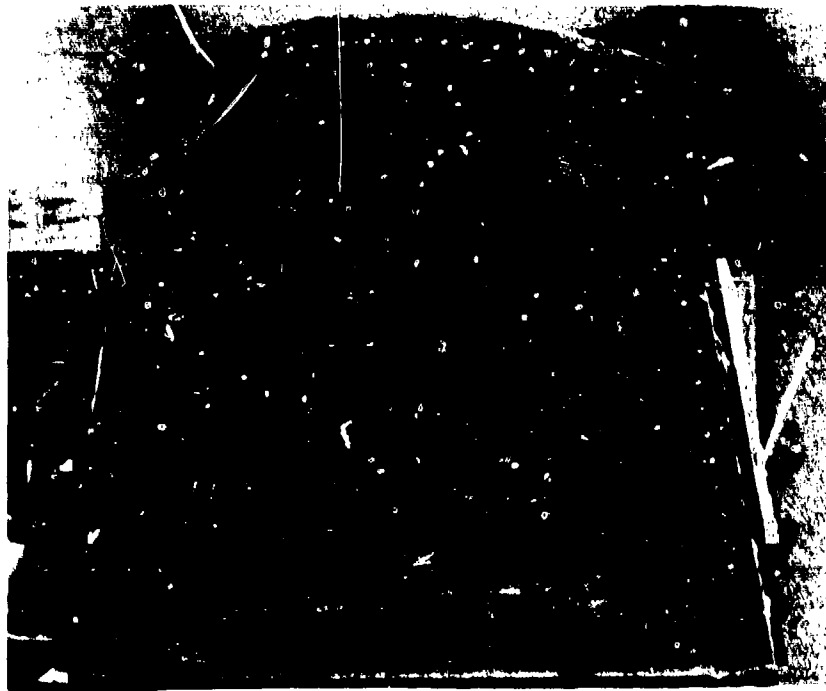
Figure 2.2. Photograph of front of target tank without the target panel.

dimension of these target panels was 69 cm. In shots labelled FTC and in the FD graphite epoxy shots, the panels were rigidly clamped on the edges.

Some of the aluminum panels were reinforced with stiffeners. Figure 2.3 shows a drawing of the stiffener geometry, and Figure 2.4 shows a panel with the stiffeners applied. The panels were mounted 13.8 cm apart with 4.8-mm-diameter, solid round-head aluminum rivets on 25.4 mm centers. The junction between the stiffener edge and the panel was caulked with RTV. End caps were placed on the stiffeners to keep water out. Water seepage into the stiffeners was also alleviated by drilling drainage holes on the bottom of the front of the panel (except in Shots 34 and 35).

Many panels were protected by application of 10 mm of closed-cell foam (Avco Thermarest AX5052). The adhesive conformed to MIL-S-88020 and 2, class B-2. It was manufactured by Products Research and Chemical Corporation, Item PR-1422 B-2. It was applied with a 1/8-inch trowel. Foam was only applied to the aluminum basic plate; when stiffeners were present the foam did not cover the rivets on the stiffener skin.
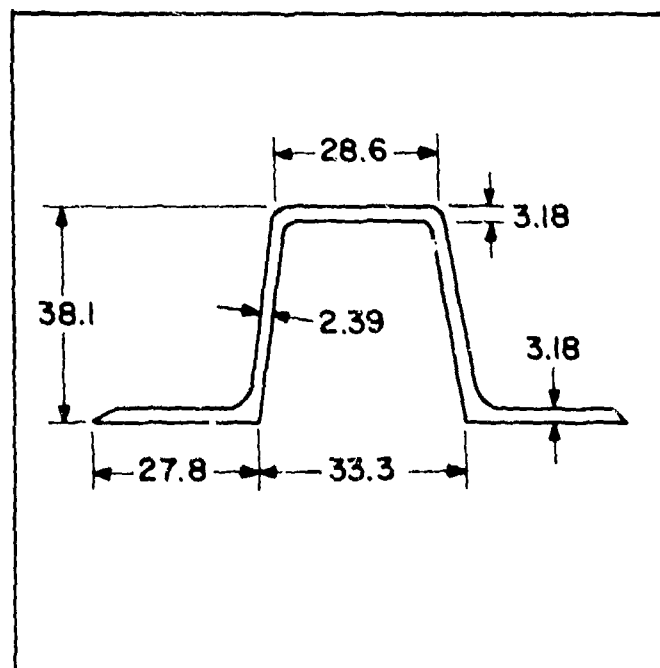
Figure 2.3.   Stiffener geometry.   Material is 6063-T6 aluminum.
Dimensions are in mm.

Figure 2.4.   Illustration of construction of stiffened panel.

6

The graphite epoxy panels were supplied by AFFDL, and their density was determined to be 1.49 g/cm^3. The following description was supplied by Mr. R. Achard of AFFDL/FBS:

The graphite panels were fabricated as 4 ft. x 6 ft. plates, 24 plies and 32 plies, respectively, in two autoclave runs. The nominal lay-up for the panels was $[0/\pm45/90]_{3S}$ for the 24 ply panel and $[0/\pm45/90]_{4S}$ for the 32 ply panel. These panels were fabricated from Hercules 3501/AS material using the standard curing cycle which was as follows: The material was set up on a flat plate with bleeder on both sides, the bleeder being separated from the graphite/epoxy prepreg by separator plies of Teflon coated glass. The assemblage of bleeder, separators and uncured graphite epoxy was enclosed in a vacuum bag and subsequently full vacuum of 28 inches mercury was applied. The panel was heated in the autoclave to 225°F in approximately 70 minutes under full vacuum. At 225°F, 85 psi autoclave pressure was applied, and the full vacuum maintained for one hour. After the one hour hold at 225°F, the vacuum bag was vented to atmosphere and the part heated to 350°F in approximately 50 minutes. At 350°F the part was maintained for one hour. This completed the cure. Subsequently, the part was cooled to below 150°F under pressure and then removed from the autoclave. Both panels were dimensionally checked and found to be warp free and to have a per ply thickness of .0055 for the 24 ply laminate and .0054 for the 32 ply laminate.

The cured 4 ft. x 6 ft. panels were
subsequently cut into 2 ft. x 2 ft. squares
using a band saw with a silicone carbide
blade. Fiberglass frame tabs (.16 in thick
x 2 in wide) were then bonded to the panels
using room temperature curing two-part epoxy
cement. The panels were subsequently delivered
for test.

2.3 INSTRUMENTATION

Three types of terminal effects measurements were made
for most shots. Pressure at several points within the fluid
was measured with small tourmaline transducers. These trans-
ducers are described in Appendix A; they possessed a frequency
response of almost 1 MHz. The locations of the transducers
are given in Table II.

TABLE II.   TRANSDUCER LOCATIONS

Identity	r (mm)	z (mm)
T1	75	6
T2	100	6
T3	200	6
T4	100	100
T5	100	200

Dynamic panel displacement was determined with a moiré
fringe apparatus as described in Reference 2. A description of
the revised system and the analysis techniques is also
provided in Appendix A.   The moiré fringe system possessed
a maximum resolution of 0.2 mm, and it viewed a little more
than half the target panel.

2.4 NOMENCLATURE

Throughout this report we use a set of abbreviations in
order to easily describe specific shot configurations. The

8

abbreviations are defined in Table III. The first symbol indicates the panel material and thickness. The second symbol indicates the projectile shape and size. The third symbol indicates the presence or absence of foam protection. Impact velocity is indicated by its value, in km/s written after the symbols. For example, 7L1.60 represents a 6.35-mm-thick 7075-T6 panel struck by a 11.7-g cube at 1.60 km/s.

TABLE III. NOMENCLATURE

First Symbol

      7 = 1.6-mm-thick 7075-T6 panel

      2 = 1.6-mm-thick 2024-T3 panel

      $\underline{7}$ = 6.35-mm-thick 7075-T6 panel

      $\underline{2}$ = 6.35-mm-thick 2024-T3 panel

      $\hat{\underline{2}}$ = 1.6-mm-thick 2024-T3 panel with "hat" stiffeners

      G = 3.18-mm-thick graphite epoxy panel

      $\underline{G}$ = 4.8-mm-thick graphite epoxy panel

Second Symbol

      L = 11.7-g cube projectile

      S = 5.7-g cube projectile

      L´= 11.7-g spherical projectile

      S´= 5.6-g spherical projectile

Third Symbol

      F = 10-mm ballistic foam

      Blank = no foam

SECTION III
EXPERIMENTAL RESULTS

Fifty-seven shots were fired during this program. Nine of these did not yield data for various reasons. The configurations tested, the instrumentation used, and the primary results are listed in Table IV. The first columns of the table give the shot number and impact configuration (see Table III for an explanation of the abbreviation code.) The next five columns explicitly describe the shot configuration. The next column reports the diagnostics, and the last column gives the results. In all but the stiffened panel, "Failed" refers to catastrophic crack formation. The shots designated FD were performed under Contract F33615-77-C-2082, and those designated FTC were under Contract F33615-76-C-3076. The types of data obtained were failure modes, fluid pressures, and panel displacements. The observations are discussed in detail in the following paragraphs.

The cube projectiles fired against thick panels were frequently recovered as many fragments. The threshold for fragmentation of the larger projectiles (11.7 g) was between 1.42 km/s and 1.47 km/s. Comparison of data from pairs of shots that bracketed a panel failure threshold showed a slight tendency for reduced damage to the projectile just above the failure threshold. Foam had little effect on projectile fragmentation. Projectiles fired against thin aluminum targets (1.6 mm) did not fragment.

3.1 FAILURE

The primary results of this program are failure data. Other types of data serve as diagnostics to aid in the understanding, interpolation, and extrapolation of the failure data. The scope of impact parameters that were to be examined was

10

TABLE IV. DATA SUMMARY

Shot No.	Configu- ration	Projectile Mass (g)	Target Material	Target Thickness (mm)	Foam Thickness (mm)	Impact Velocity (km/s)	Diag- nostics	Results
FD1	7L	11.66	7075-T6	6.35	0	1.82	D	Failed
FD2	7L	11.66	7075-T6	5.35	0	1.42	D	OK
FD3	7L	11.66	7075-T6	6.35	0	1.42	P,D	OK
FD4	7L	11.66	7075-T6	6.35	0	1.47	P,D	OK
FD5	7L	11.66	7075-T6	6.35	0	1.60	P,D	OK
FD6	7L	11.66	7075-T6	6.35	0	1.69	P	Failed
FD7	7L	11.66	7075-T6	6.35	0	1.59	D	OK
FD8	7L	11.66	7075-T6	6.35	0	1.63	P,D	OK
FD9	7LF	11.66	7075-T6	6.35	10	----	----	Sabot failure
FD10	7LF	11.66	7075-T6	6.35	10	----	----	Sabot failure
FD11	7LF	11.66	7075-T6	6.35	10	1.78	P,D	OK
FD12	7LF	11.66	7075-T6	1.6	10	1.75	P,D	Failed
FD13	7LF	11.66	7075-T6	1.6	10	1.58	P,D	OK
FD14	7LF	11.66	7075-T6	1.6	10	1.67	P,D	Failed
FD15	7S	5.66	7075-T6	1.6	0	1.98	P,D	Failed
FD16	7SF	5.66	7075-T6	1.6	10	1.99	P,D	OK
FD17	2L	11.66	2024-T3	6.35	0	----	----	sabot failure
FD18	2L	11.66	2024-T3	6.35	0	----	----	Sabot failure
FD19	7S	5.66	7075-T6	6.35	0	1.95	P,D	OK
FD20	7S	5.66	7075-T6	1.6	0	----	----	Incomplete powder burn
FD21	7S	5.66	7075-T6	1.6	0	1.82	P,D	Failed

TABLE IV. DATA SUMMARY (CONT'D)

Shot No.	Configuration	Projectile Mass (g)	Target Material	Target Thickness (mm)	Foam Thickness (mm)	Impact Velocity (km/s)	Diagnostics	Results
FD22	7S	5.66	7075-T6	1.6	0	1.74	P,D	Failed
FD23	7S	5.66	7075-T6	1.6	0	1.35	P,D	Failed
FD24	7S	5.66	7075-T6	1.5	0	----	----	Sabot failure
FD25	GS	5.59*	gr-ep	4.76	0	1.46	P,D	Failed
FD26	GSF	5.59*	gr-ep	3.18	10	1.69	P,D	OK
FD27	7S	5.66	7075-T6	1.6	0	1.24	----	Failed
FD28	7S	5.66	7075-T6	1.6	0	0.92	----	OK
FD29	7S	5.66	7075-T6	1.6	0	1.06	----	Failed
FD30	2L	11.66	2024-T3	6.35	0	1.62	P	OK
FD31	2L	11.66	2024-T3	1.6	0	1.32	P	Failed
FD32	2LF	11.66	2024-T3	1.6	10	----	----	Sabot failure
FD33	2L	11.66	2024-T3	1.6	0	1.30	----	Failed
FD34	2L	11.66	2024-T3*	1.6	0	1.49	----	Failed†
FD35	2L	11.66	2024-T3*	1.6	0	1.20	----	Failed†
FD36	2L	11.66	2024-T3*	1.6	0	----	----	Sabot failure
FD37	2LF	11.66	2024-T3*	1.6	10	1.56	P	Failed†
FD38	2S	5.66	2024-T3*	1.6	0	1.19	P	OK
FD39	2LF	11.66	2024-T3*	1.6	10	1.35	P	Failed†

*These panels had stiffeners.

†Failure for stiffened panels was defined as more than 5 rivets popped and 15 mm permanent displacement on any one stiffener.

12

TABLE IV. DATA SUMMARY (CONT'D)

Shot No.	Configuration	Projectile Mass (g)	Target Material	Target Thickness (mm)	Foam Thickness (mm)	Impact Velocity (km/s)	Diagnostics	Results
FD40	2S	5.66	2024-T3*	1.6	0	1.33	P	OK
FD41	2S	5.66	2024-T3*	1.6	0	1.35‡	P,D,E	Failed †
FD42	2L	11.66	2024-T3*	1.6	0	0.08	-----	No perf.
FD43	#2L	11.66	2024-T3*	1.6	0	1.12	P	OK
FD44	2LF	11.66	2024-T3	1.6	10	1.68	-----	OK
FTC1	7S	5.59*	7075-T6	3.18	0	1.55‡	D	Failed
FTC2	2S	5.59*	2024-T3	3.18	0	1.55‡	D	OK
FTC3	GS	5.59*	gr-ep	3.18	0	1.51‡	P	Failed
FTC4	GS	5.59*	gr-ep	3.18	0	0.96	D	OK
FTC5	GS	5.59*	gr-ep	3.18	0	1.28	D	Failed
FTC6	GS	5.59*	gr-ep	3.18	0	1.01	D	OK
FTC7	GS	5.59*	gr-ep	3.18	0	1.18	D	Failed
FTC8	GS	5.59*	gr-ep	4.76	0	1.11	D	OK
FTC9	GS	5.59*	gr-ep	4.76	0	1.36	D	K
FTC10	GS	5.59*	gr-ep	4.76	11	1.63	D	Failed
FTC11	GSF	5.59*	gr-ep	4.76	11	1.95	D	OK
FTC12	GSF	5.59*	gr-ep	4.76	11	1.98	D	OK
FTC13	GSF	5.59*	gr-ep	3.18	11	1.18	D	OK

*Spherical projectile
†These panels had stiffeners. Failure for stiffened panels was defined as more than 5 rivets popped and 15-mm permanent displacement on any one stiffener.
‡No x-ray obtained. Uncertainty in velocity is ±8%, -1%.
‡Same panel as FD42.

5.6-g to 11.2-g (90 to 180 grain) mass fragments at velocities between 1.4 km/s and 2.0 km/s. The lower velocity limit was later extended in order to observe critical failure phenomena in thin target panels. The failure data obtained for each configuration are given in Table V. For each configuration, this table lists the relevant shots, the experimental limits, or the failure threshold velocity.

3.1.1 Modes of Failure

In most instances, failure was characterized by a distinct threshold velocity. Below the threshold, the only damage to the target panel was the primary perforation and some permanent plastic deformation. Above the threshold, cracks formed that ran to the edges of the panel.

In the plain aluminum panels, failure occurred as relatively straight cracks. Crack patterns were similar in 2024-T3 and 7075-T6 panels. In thin (1.6 mm) panels struck by cubes, the cracks started at the corners of the square perforation hole in the panel. There were two cracks at velocities just below the threshold. As velocities increased, three, then four cracks formed. The orientation of the crack system was the same as that of the thin panels struck by cubical projectiles. These observations are illustrated in Figures 3.1, 3.2, and 3.3, which show aluminum panels struck at velocities below the failure threshold, a little above the threshold, and well above the threshold. The cracks in these panels ran straighter than those reported prev ously in similar panels failed by spherical projectiles[2].

In thick panels (6.35 mm), no more than two cracks were observed. For example, Figures 3.4 and 3.5 illustrate the failure in a 6.35-mm-thick 7075-T6 panel struck by a 11.7-g projectile at 1.82 km/s (configuration 7L1.82).

Foam-backed aluminum also failed catastrophically. When failure occurred, the cracks were not straight as in plain panels. Figure 3.6 illustrates the "S" pattern formed by the cracks in a foam-backed 7075-T6 panel.

14

TABLE V.   SUMMARY OF FAILURE DATA

Configuration	Shots	Results
7L	FD1-8	$V_F = 1.66 \pm .03$
7LF	FD11	$V_F > 1.95$
7S	FD19	$V_F > 1.95$
7SF	----	Est. $V_F > 2.0$
7L	----	Est. $V_F < 0.99$
7LF	FD12, 13, 14	$V_F = 1.62 \pm .05$
7S	FD15,21,22,23,27, 28,29,FTC1	$V_F = 0.99 \pm .06$
7SF	FD16	$V_F > 1.99$
2L	FD30	$V_F > 1.62$
2LF	----	Est. $V_F > 2.0$
2S	----	Est. $V_F > 2.0$
2SF	----	Est. $V_F > 2.0$
2L	FD31,33,FT6,FTA7,9	$V_F < 1.30$
2LF	FD44,FTA11	$V_F > 1.68$
2S	FT5,5A,5B; FTC2 FTA3,4,5,6,10	$V_F = 2.08 \pm .13$
2SF	FTA12	$V_F > 2.38$
GS	FTC8,9,10 FD25	$V_F = 1.47 \pm .05$
GSF	FTC10,11	$V_F > 1.36$
GS	FTC4,5,6,7	$V_F = 1.09 \pm .08$
GSF	FTC13, FD26	$V_F > 1.69$
$\hat{2}$L	FD34,35,36,43	$V_F = 1.16 \pm .04$
$\hat{2}$S	FD38,40,41	$V_F = 1.34 -.01, +.11$
$\hat{2}$LF	FD37,39	$V_F < 1.35$
$\hat{2}$LF	----	Est. $V_F = 1.34$

NOTES: FT and FTA shots were reported in AFML-TR-77-11.
          FTC shots were done under Contract F33615-76-3076
          Request 45.
          FT,FTC, and FD25 and 26 used spherical projectiles;
          other shots used cubes.

15

Figure 3.1.   Panel from Shot FD28 (7S0.92), showing damage at
just below the failure threshold in thin 7075-T6
panels.
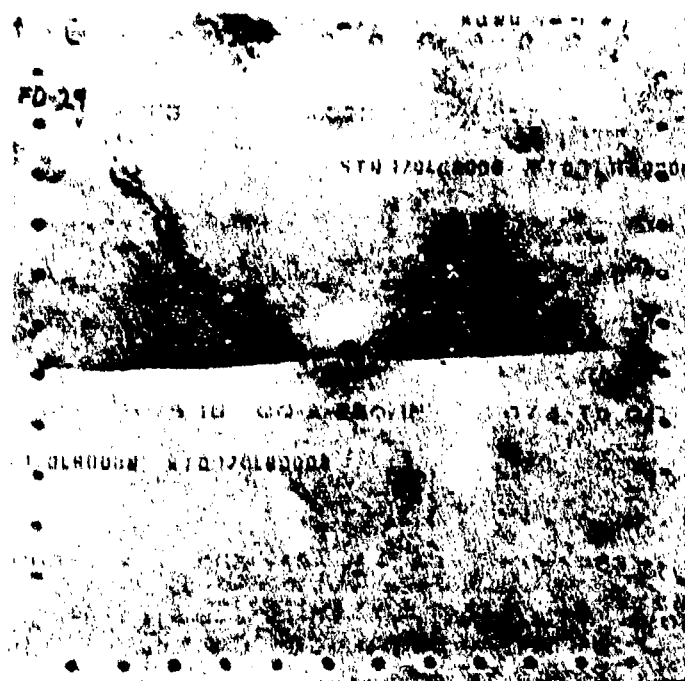
Figure 3.2.   Panel from Shot FD29 (7S1.06), same as Fig. 3.1
except a little above the failure threshold.
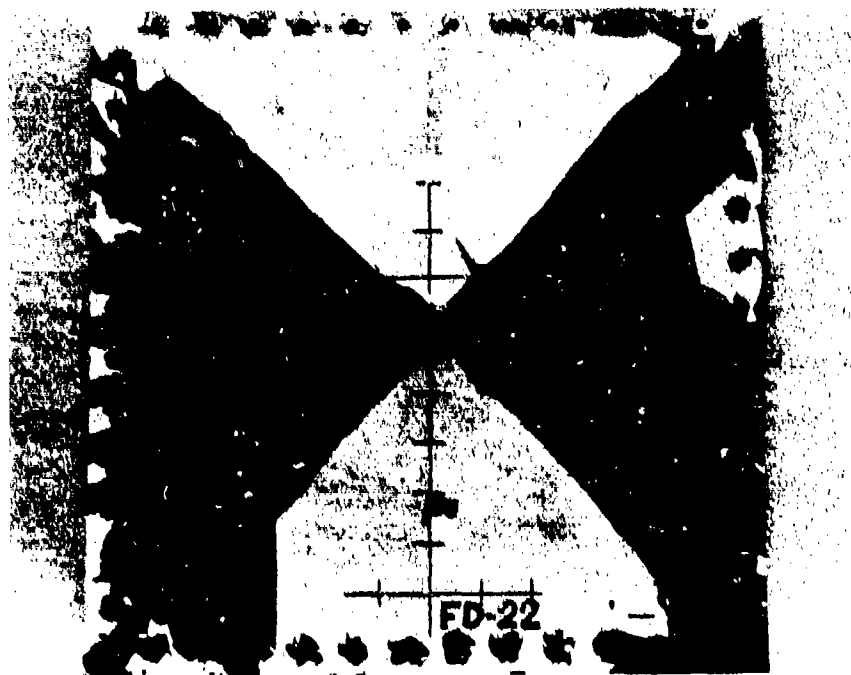
Figure 3.3. Panel from Shot FD22 (7S1.74); like Fig. 3.2 but well above the threshold velocity.
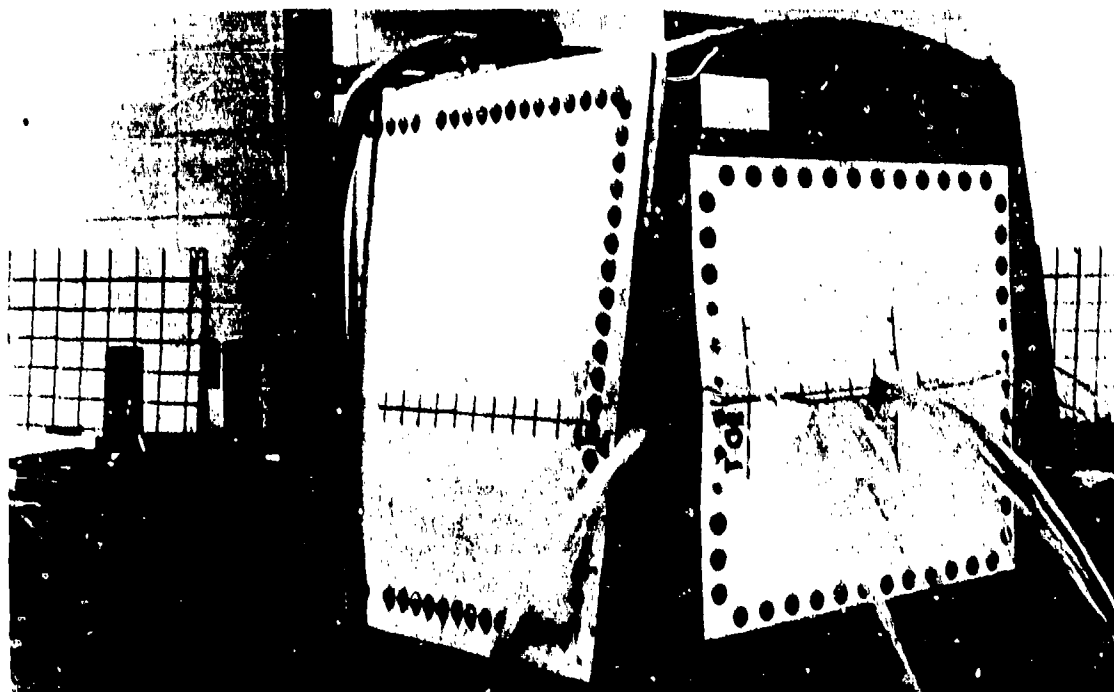
Figure 3.4. Panel from Shot FD1 (7L1.82), showing crack pattern in thick 7075-T6 panel struck well above failure threshold.
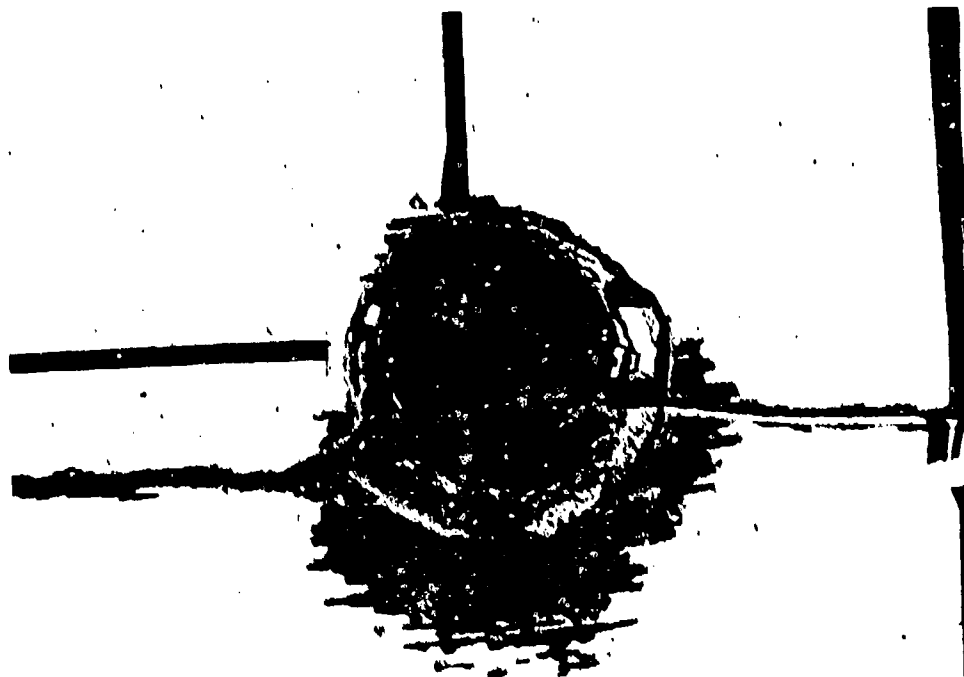
Figure 3.5.   Close-up of impact area in FD1, showing front surface spall and cracks.

Figure 3.6.   Panel from FD12 (7LF1.75), illustrating crack pattern in a foam-backed panel.

The graphite epoxy panels also exhibited sudden failure thresholds; however, the crack system followed the 0/45/90 layup of the fibers. The crack first ran horizontal and then branched to follow the fiber directions. Figure 3.7 illustrates a typical failure of a graphite epoxy panel.

Definition of failures in the stiffened panels was not so straightforward. The damage that occurred included cracking of the panel, crushing of the stiffeners, and "popping" of rivets. The cracks in the panel were always stopped by the stiffeners. Cracks that started to travel vertically between stiffeners travelled only a relatively short distance before turning into a stiffener and stopping. Figure 3.8 illustrates these features of the failure The panel in the figure was massively torn near the impact site, but the cracks did not run more than about ten projectile diameters. Addition of foam alleviated the entrance panel failure. Foam had no discernable effect on stiffener crushing and rivet failure, as shown in Figures 3.9 and 3.10. However, the foam was not attached to the stiffeners themselves (see Section 2.2).

Figure 3.7. Failure in a graphite epoxy panel.

19
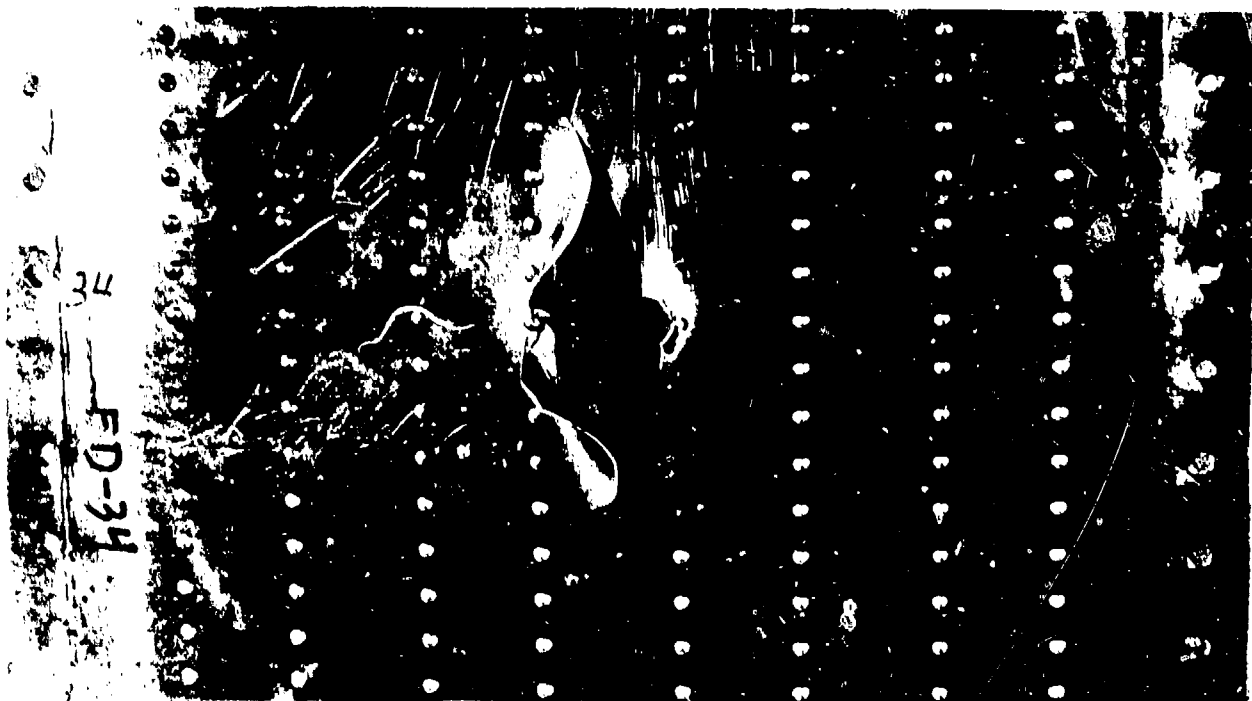
Figure 3.8.   Panel from Shot FD13 ($\widehat{2}$L1.49), showing how
              stiffeners prevented massive tearing.
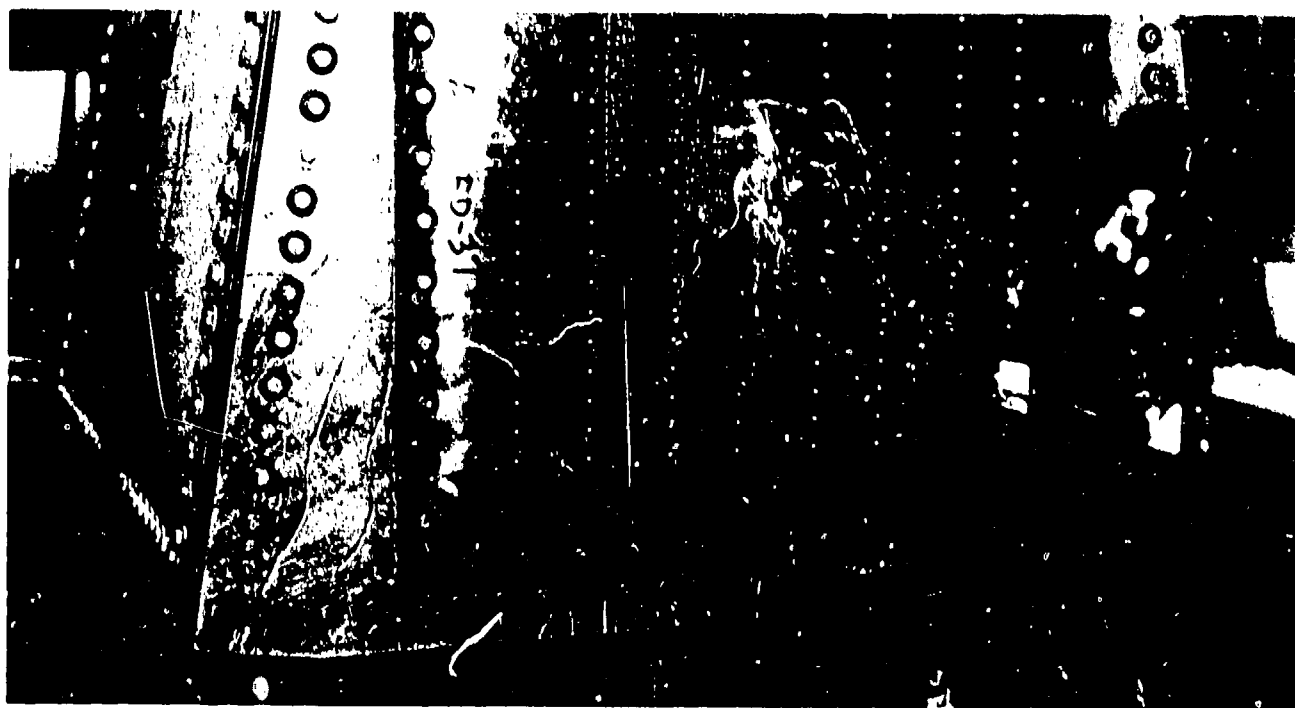
Figure 3.9.   Panel from Shot FD37 ($\widehat{2}$LF1.56).   The foam had
              little effect on the rivet failures. Note: foam
              did not cover rivets (see Section 2.2).

20
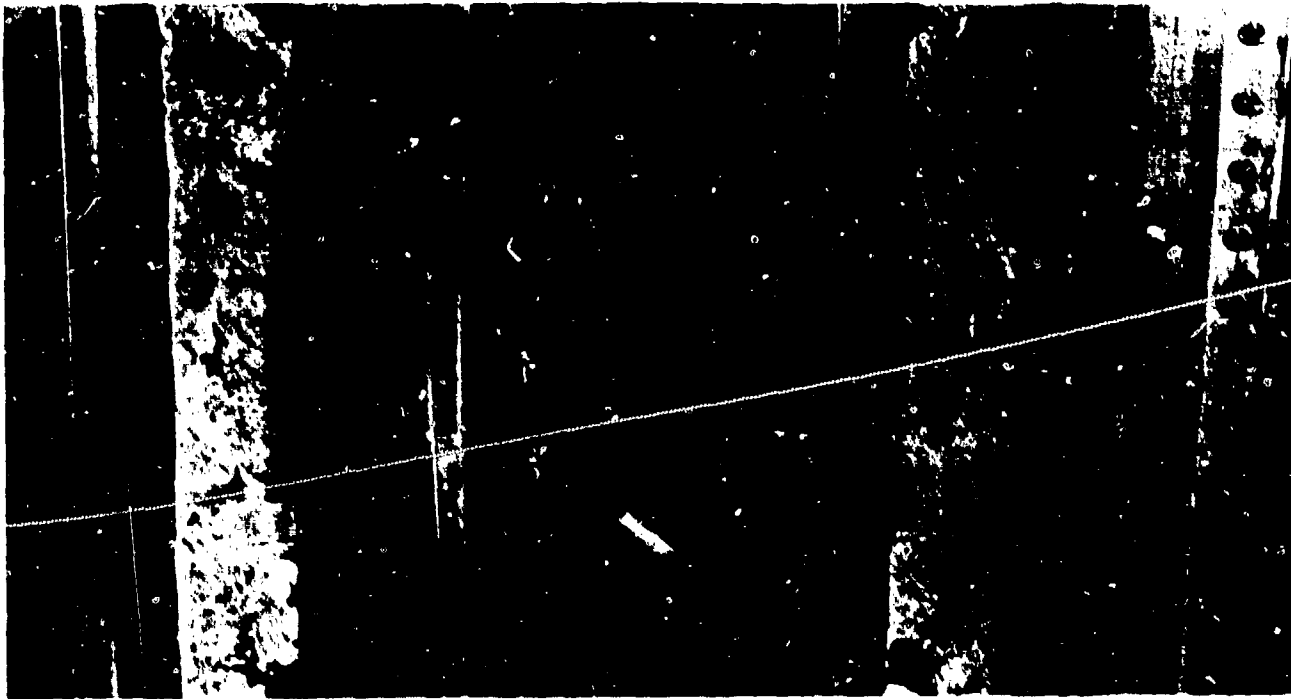
Figure 3.10.   Rear of panel from Shot FD37, showing crushing
               of stiffeners.

    There was an excellent correlation between the final de-
flection* of a stiffener and the number of rivets popped. At
10-mm displacement or less, no rivets popped; at 15-mm displace-
ment or more, 8 or more rivets popped. This phenomenon provided
a convenient way to define failure, since the number of rivets
failed was always none or more than seven. According to this
definition, a "failed" stiffened panel was one whose ability to
support compressive loads had been severely reduced by damage to
one or more reinforcing elements. No stiffened panel failed
in such a way as to cause massive liquid leakage (as occurred
in unstiffened panels) or serious degradation of the tensile
properties of the structure.

    Some insight into the failure mechanism resulted from Shot
FD35, in which one of the stiffeners next to the impact site
accidentally filled with water. That stiffener was not deformed

---

*Final deflection of a stiffener was measured by laying a
straight edge along the top of the stiffener and measuring the
maximum distance between the straight edge and stiffener surfaces.

21

and no rivets were popped. This result indicates that rivet
failure was due to stiffener collapse (e.g., motion in the
x-direction), not panel displacement.

The velocity of propagation and the time of initiation of
the cracks were determined for a few representative cases. For
the bare thin 7075-T6 panels (namely FD15, 7S1.59), the velo-
city steadily decreased. For the first few frames after impact,
the velocity was $\sim$300 m/s; however, beyond about 150 mm from
impact, it slowed to about 200 m/s. The delay time between
impact and crack initiation for both thin and thick bare panels
could not be resolved; i.e., these events were simultaneous
within an uncertainty of about 100 μs. For example, Figure 3.11
shows the first frame after impact in Shot FD23. (This is within
180 μs after impact.) The cracks have already grown to a length
of over 60 mm. Crack initiation was not always prompt in
failures of foam-backed 1.6-mm 7075-T6 panels. The cracks
started between 360 μs and 720 μs after impact, and in Shot FD14
they started between 0 and 350 μs after impact.

3.1.2 Perforation Data

The size of the perforation hole in the target
panels was dependent on impact velocity. The data for 7075-T6
aluminum are given in Table VI. Where the hole was not round,
we used an equivalent diameter, computed from $\sqrt{4A_h/\pi}$, where
A_h was the hole area.

The data are displayed graphically in Figure 3.12
in which d/W (hole diameter scaled by panel thickness) is
plotted against impact velocity. Plotted in this format, the
data fall into two groups, with the thick panel data lying
below the thin panel data. For thin panels, $\partial d/\partial W|_{W,D} > 0$,
as one would expect. However, for the thick panels, the
dependence of d on W is so small that it is only marginally
detectable from the figure.

The hole diameter in the thin panels was substan-
tially decreased by the presence of foam. Compare 7S and 7SF.
The hole formation proceeded by a crater growth process that
was terminated by release waves from the aluminum/foam interface.

22
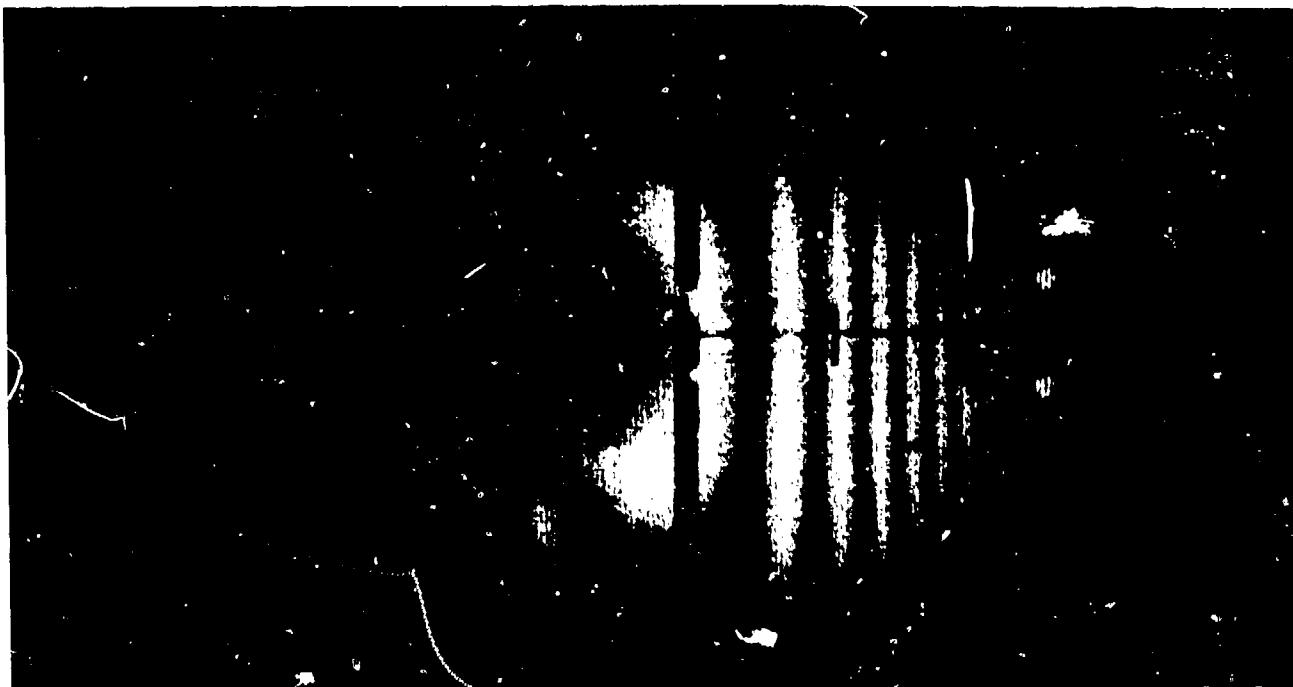
Figure 3.11.   Second frame after impact in Shot FD23 (7S1.35).
Camera speed was 5.5 frames/ms, and horizontal
crack is already clearly visible.
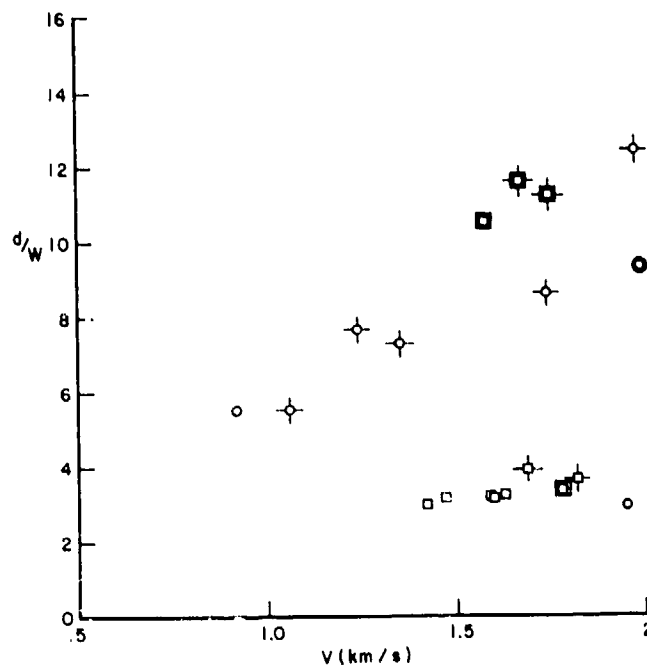
Figure 3.12.   Hole diameter scaled by panel thickness versus
impact velocity.   Square symbols show thick
panels and round symbols show thin panels.
Nested symbols indicate foam.   Radial lines
indicate failure.

TABLE VI. HOLE SIZE DATA

Shot No.	Configuration	V	d	$\frac{d}{w}$
1	7L	1.82	23.4	3.69
2	"	1.42	18.3 {19.0	2.99
3	"	1.42	19.7	
4	"	1.47	20.1	3.17
5	"	1.60	20.2	3.18
6	"	1.69	24.9	3.92
7	"	1.59	20.6	3.24
8	"	1.63	20.6	3.24
9	7LF	----	19.66	3.10
10	"	----	18.96	2.99
11	"	1.78	21.50	3.39
12	7LF	1.75	18.07	11.29
13	7LF	1.58	16.82	10.54
14	7LF	1.67	18.60	11.63
15	7S	1.98	19.97	12.48
16	7SF	1.99	15.02	9.39
17	2L	----	17.76	2.80
18	"	----	17.11	2.69
19	7S	1.95	18.47	2.95
22	7S	1.74	13.84	8.65
23	7S	1.35	11.66	7.29
27	7S	1.24	12.31	7.69
28	7S	0.92	8.86	5.54
29	7S	1.06	8.86	5.54

24

For thin panels, hole size correlated with failure, all else being equal. The thin panels failed when d/W exceeded about unity. Hole size varied little on the thick panels. The data support the statement that failure occurred when d/W exceeded about 1.65.

In two out of three cases (see Figure 3.12), maximum hole size occurred at velocities slightly higher than the failure threshold velocities. This may be analogous to a well-known phenomenon of conventional terminal ballistics: the maximum energy deposition in a target plate occurs at the limit velocity. This is consistent with the trend that projectile fragmentation had a slight maximum at velocities just below failure threshold velocity.

Do large holes induce radial cracks at the impact site? If they do, then analysis of hole formation might lead to a useful failure prediction. The mechanism by which foam protects panels from gross damage would also be clarified. Even if large holes do not induce failure, a failure prediction algorithm might be based on a prediction of hole size and an empirical correlation. However, a relatively simple analysis can show that hole size is not causally related to fracture. Consider, for example, a thin plate with a round hole; and let the plate be subjected to a radial tension P far from the hole. This situation is analogous to the early-time loading in a target panel; the water pressure acts on an annular region around the hole, while the region immediately adjacent to the hole experiences no external loading because of the cavity behind the projectile. The stress in the panel at the hole boundary in this approximation is given by

$$\sigma_r = P \ (1-d^2/r^2) \tag{1}$$

$$\sigma_\theta = P \ (1+d^2/r^2) \tag{2}$$

Thus, the hoop stress at the hole, σ_θ (r=d), is equal to 2P, regardless of d. In other words, the hole size does not influence the maximum tensile stress at its boundaries. (Of course, the hole shape will affect the stress distribution. That is why cracks initiate at the corners of the square holes.

3.2 PRESSURE DATA

Free-field pressure data were obtained in most shots. The form of the pressure time curves was strongly influenced by panel geometry; however, it was only weakly dependent on projectile size. In this section we present the data together with some analysis. Additional analysis is contained in Section IV in which the data are compared with the numerical results.

We first discuss the data for pressure variations behind thick (6.35 mm) aluminum panels. The set of data available pertains to the 11.67-g cubical projectiles. Most attention was directed to the r = 100 mm station, and usable data were obtained for that transducer in every shot. Figures 3.13 - 3.17 show how the measured pressure pulse varied with impact velocity. For reference, Figure 3.18 is a sketch that illustrates individual features common to all the traces. These are labelled as follows:

> E1 - a small precursor signal
>
> P1 - first sharp peak associated with first significant arrival
>
> P2 - second peak, often composed of several subpeaks
>
> P3 - third broad peak
>
> R2 - initial sharp fall that marks the end of P2
>
> R3 - sharp fall from third peak value
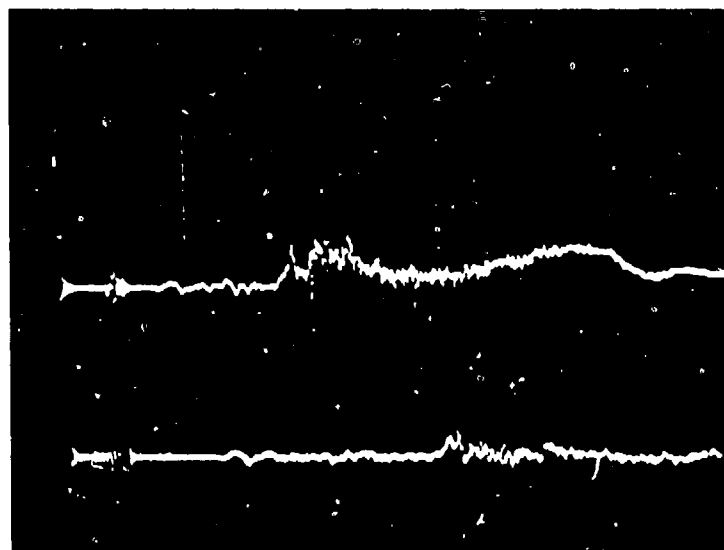
Figure 3.13. Upper trace is r 100 mm pressure transducer from Shot FD3. Note: Scale marks indicate 50 µs and 0.41 kbar (6 ksi). Lower trace is r 200 mm transducer at the same sweep speed.
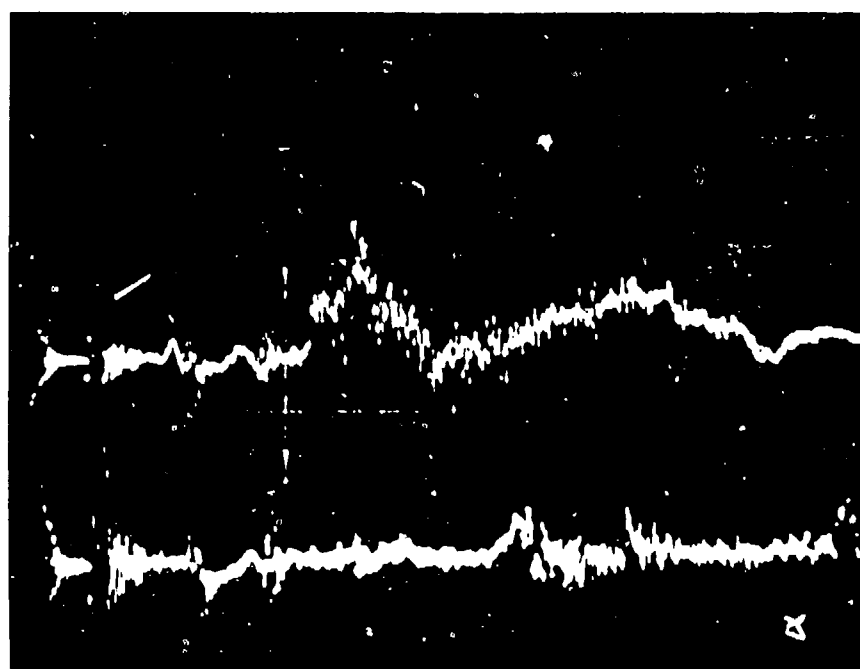
Figure 3.14. Upper trace is r=100 mm pressure transducer from Shot FD4. Note: Scale marks indicate 50 µs and 0.41 kbar (6ksi). Lower trace is r=200 mm transducer at the same sweep speed.
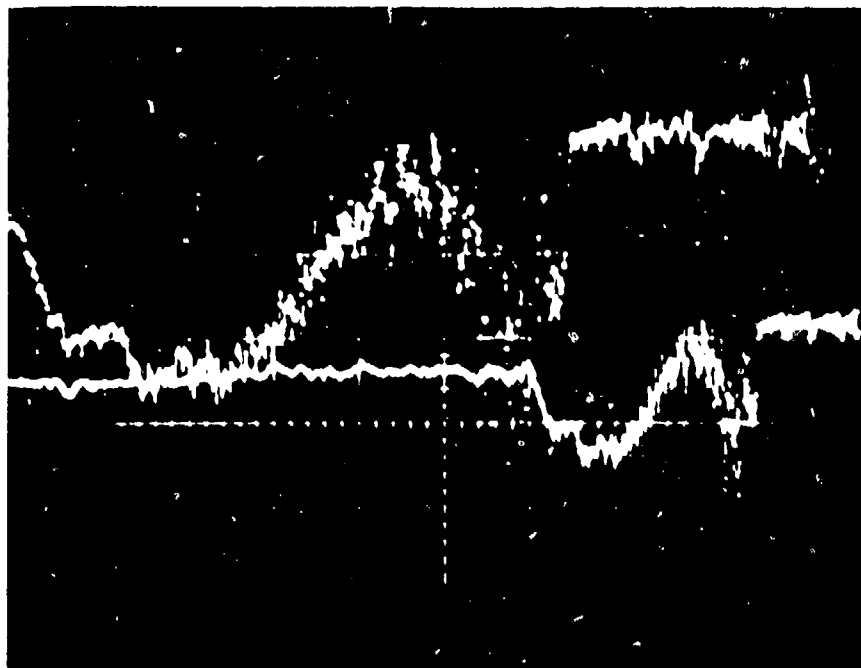
Figure 3.15.   Record for r=100 mm transducer from Shot FD5.   Note:
Upper trace sweep is 50 μs/division; lower trace
sweep is 20 μs/division.   Upper trace amplification
is 105 bar/division (1.53 ksi/division);
lower trace amplification is 52.8 bars/division
(766 psi/division).
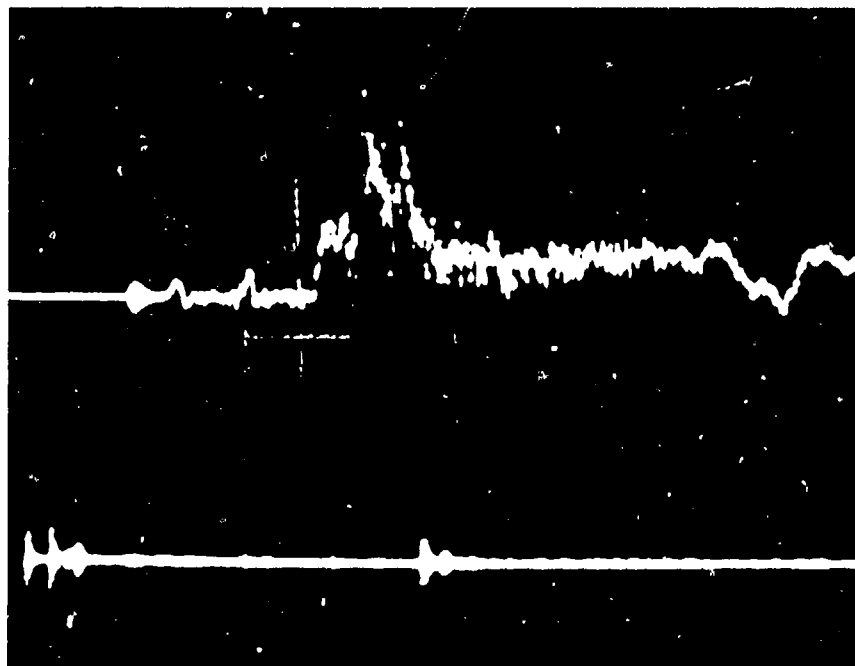
Figure 3.16.   Record from r=100 mm transducer from Shot FD8.
Note: Scale marks indicate 50 μs and 0.41 kbar
(6 ksi).

28
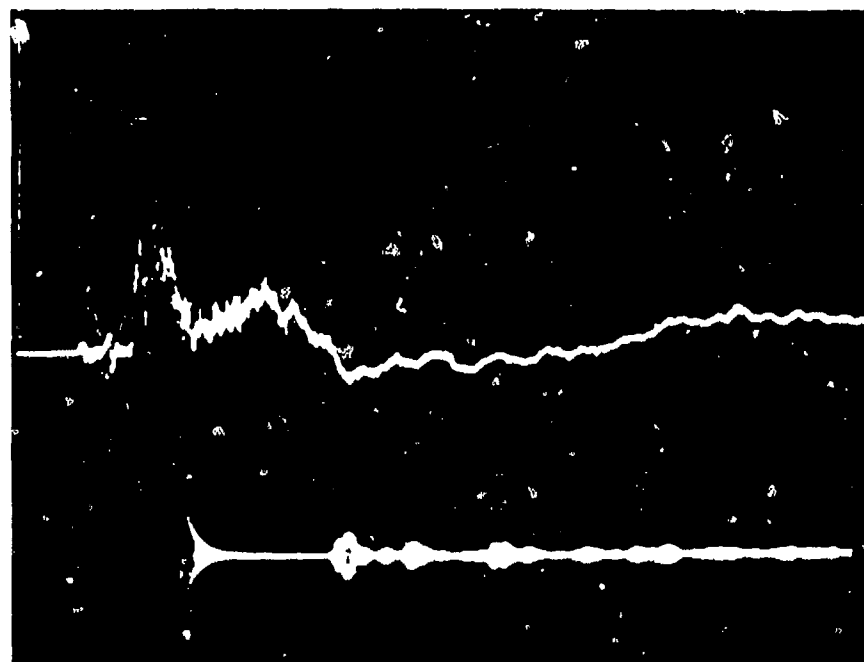
Figure 3.17.   Record from r=100 mm pressure transducer from
                Shot FD6.   Note: Scale marks indicate 50 μs and
                0.41 kbar (6 ksi).
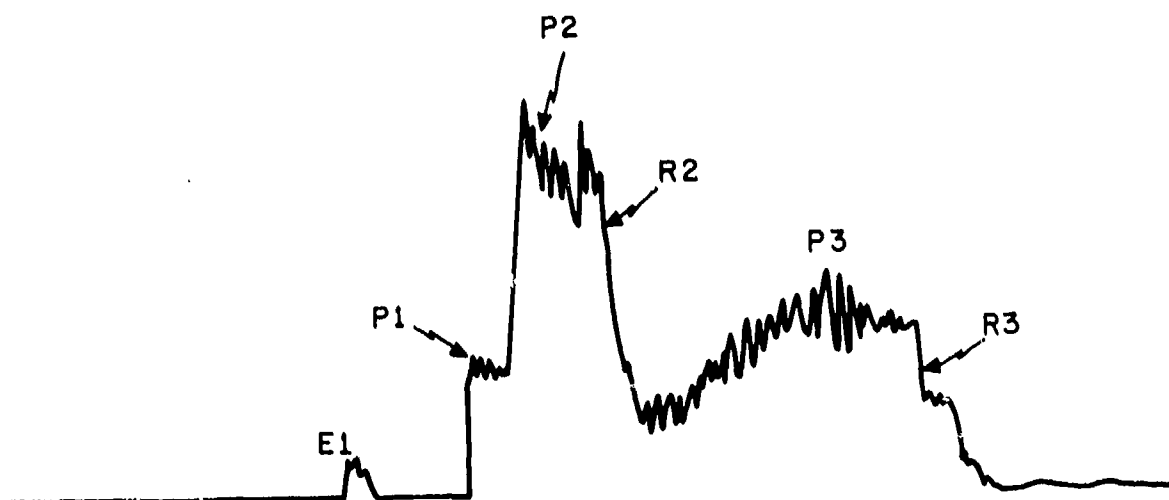
Figure 3.18.   Sketch of general form of r=100 mm pressure
                records.

29

Figure 3.19 illustrates typical data from an r = 75 mm transducer. The details of these traces were also very consistent in the shots for which good data were obtained, namely FD3, 4, 5, and 8. In FD3 and 4, two side-by-side transducers were placed at this station, and the resulting pressure traces were essentially identical. All the r = 75 mm data show three arrivals of similar amplitudes at intervals of about 10 μs.

Data obtained from the pressure records are summarized in Tables IV, V, and VI. Table VII contains the arrival time data for the r = 100 mm station. The uncertainty in the instant of impact prevents an accurate estimate of absolute arrival times. The P1, R2, and R3 arrival times were measured from the first detectable signal. The P2 arrival was measured from half way up the first rise in pressure for that pulse; this is the most widely accepted procedure for determining shock arrival times. Relative arrival times are very consistent, but no correlations with velocity were discovered. The average and standard deviation for relative arrival times are 8.66 ± 0.75 μs for P2 - P1, 90.36 ± 4.54 μs for R3 - P2, and 99.02 ± 3.83 for R3 - P1. Our interpretation of these events is that E1 arises from the elastic wave that runs out in the aluminum plate, and P1 results from energy that is coupled to the aluminum by the shock in the water. (see Section 4.1). P2 is the wave that results from the strong shock that propagates ahead of the projectile through the aluminum and into the water, where it produces an approximately hemispherical pressure wave. We believe the third pressure pulse is caused by the drag force on the fluid after the projectile and wall fragments entered the water. The most solid argument for this interpretation is the relatively late arrival of this pulse, typically 40 μs after P1, and its long duration; since the projectile takes less than 5 μs to perforate the target plate, this pressure must be caused by the projectile-fluid drag force. The variability of the P3 amplitude is presumably caused by variations in the way that the projectile broke up. The end of the P3 pulse is probably caused by the arrival of the cavity at the transducer.

30

Table VIII contains the data for peak pressure behind 6.35-mm-thick aluminum panels. The decay of the P1 pressure with range is shown graphically in Figure 3.20. In this figure we note that the value at r - 20 cm for FD8 is highly anamolous. We believe the recorded scope setting is probably erroneous. The limited data set suggests an r^{-2} fall-off. The impulses obtained by integrating the pressure traces are given in Table IX. Some of the error brackets are assymmetric; they resulted from uncertainties concerning base line shifts in the pressure records[*]. The impulse variations with range are discussed more fully in Section IV.

Figure 3.21 shows the result of adding foam (configuration 7LF) to the thick panels. Two of the peaks have been suppressed at both radii. This supports the assertion that the first peak is caused by a shock wave in the aluminum, since the foam decouples the aluminum from the water.

The pressure traces in thin panels also did not contain multiple arrivals. Figure 3.22 shows what happens when the thick panel is replaced by a thin one, e.g., configuration 7S. The waves associated with propagation in the aluminum are absent or greatly attenuated. All pressure traces from the extensive 7S series of shots had the form of Figures 3.23 and 3.24. The pressure pulses must be mainly the result of the interaction of the projectile and water.

Figure 3.23 shows the effect of adding foam to this configuration (e.g., 7SF). The arrival is sharper, since the small signals caused by waves in the panel have been eliminated. The duration has also been slightly reduced; however, the peak and impulse have been only slightly affected.

---

*When base line shifts occurred, it was assumed that they were linear, starting at the P1 arrival and ending at the conclusion of P3. Apparently both positive and negative shifts occurred. Negative shifts can be caused by high temperatures. The cause of positive shifts has not yet been determined.
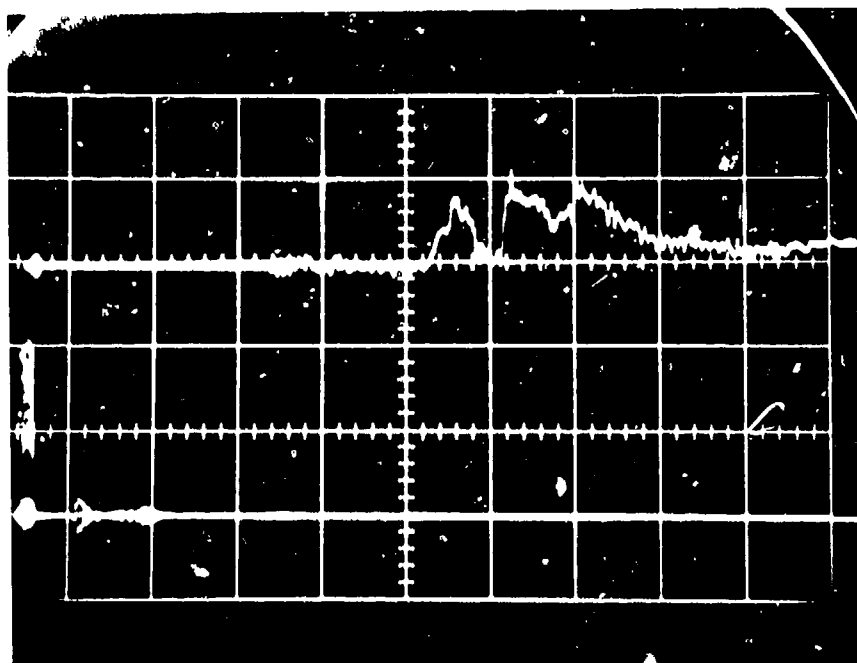
Figure 3.19.   Record from r = 75 mm pressure transduce₁ from
              Shot FD8.   Note: Sweep speed is 10 μs/division,
              and amplification is 258 bars/division (3.75 ksi/
              division).   (The amplification setting is suspect
              in this record.

TABLE VII.   SUMMARY OF ARRIVAL TIME DATA AT r = 100 mm, z = 6 mm
            FOR 6.35-mm PLAIN 7075-T6 ALUMINUM PANELS STRUCK BY
            11.66-g CUBES.   TIMES ARE μs AFTER BEGINNING OF TRACE.*

Shot No.	Impact Velocity (km/s)	Esti-mated Impact	P1 Arrival	P2 Arrival	R2 Arrival	R3 Arrival
FD3	1.42	13.4	68.3 ± 0.5	77.2 ± 0.5	89.3 ± 0.6	1₆5.2 ± 0.5
FD4	1.47	13.0	62.4 ± 0.5	70.2 ± 0.5	88.1 ± 0.6	164.4 ± 0.5
FD5	1.60	11.9	56.3 ± 0.8	64.6 ± 0.8	76.7 ± 0.9	159.4 ± 0.8
FD8	1.63		71.1 ± 0.2	80.7 ± 0.3	92.2 ± 0.3	165.7 ± 0.3
FD6	1.69	14.1	64.8 ± 0.5	73.7 ± 0.8	91.0 ± 0.8	162.3 ± 0.8

*The instant of impact was not well enough determined to be useful
as a time reference for arrival time comparisons.

TABLE VIII. SUMMARY OF PEAK PRESSURE DATA FOR 6.35-mm PLAIN
7075-T6 ALUMINUM PANELS STRUCK BY 11.66-g CUBES.
TRANSDUCERS WERE 6 mm BEHIND TARGET PANELS.
(NOTE 1 ksi = 0.069 kbar).

Shot No.	u_o (km/s)	Radius (cm)	First Peak (ksi)	Second Peak (ksi)	Third Peak (ksi)
FD3	1.42	7.5	2.65 ± 0.25	2.61 ± 0.26	1.92 ± 0.17
		10	1.59 ± 0.16	1.72 ± 0.16	1.64 ± 0.13
		20	---	0.363 ± 0.36	---
FD4	1.47	7.5	2.45 ± 0.30	2.37 ± 0.16	1.57 ± 0.13
		10	1.08 ± 0.05	1.78 ± 0.15	1.11 ± 0.05
		20	---	0.302 ± 0.019	---
FD5	1.60	7.5	4.58 ± 0.20	3.43 ± 0.30	3.33 ± 0.20
		10	1.49 ± 0.09	2.24 ± 0.20	2.31 ± 0.38
FD8	1.63	7.5	2.91 ± 0.12	2.95 ± 0.12	3.33 ± 0.25
		10	1.17 ± 0.10	2.70 ± 0.17	0.59 ± 0.05
		20	---	$6.90 \, {}^{+\,1.0}_{-\,0.4}$	---
FD6	1.69	10	1.86 ± 0.08	2.06 ± 0.20	1.32 ± 0.12
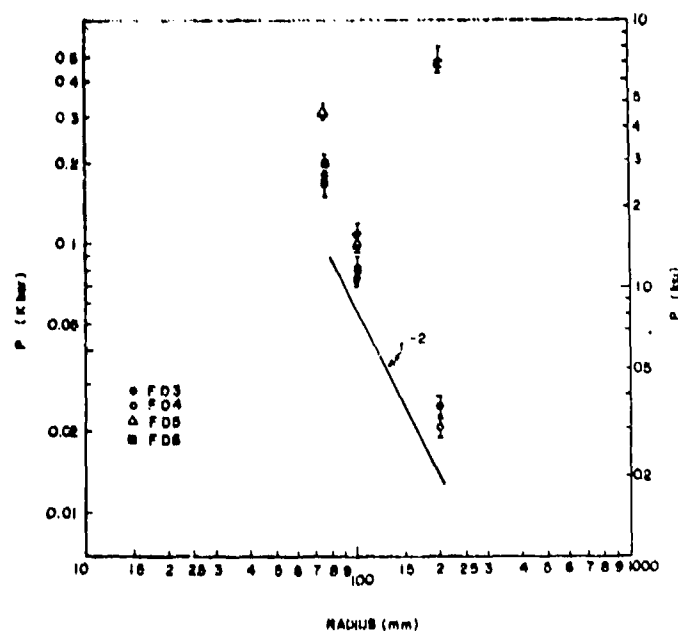
Figure 3.20. Decay of P_1 with range for 7L configuration.

33

TABLE IX. SUMMARY OF IMPULSE RESULTS AT r = 100 mm, z = 6 mm
FOR 6.35-mm 7075-T6 PLAIN PANELS STRUCK BY 11.66-g
CUBES. UNITS ARE $\cdot$as (10^{-6} bar-s)

Shot No.	Impact Velocity	Impulse in P1 and P2 Peaks	Time at End of P2*	Impulse in P1, P2, and P3 Peaks	Time at End of P3*
FD3	1.42	2210 + 270	34.4	6180 + 480	103.6
FD4	1.47	1830 + 60	29.5	4910 + 90	106.7
FD5	1.60	2860 +300 / −140	36.4	10650 +4300 / −100	130.0
FD8	1.63	2910 + 80	27.7	5800 + 60	105.0
FD6	1.69	2790 +180 / −50	35.9	8330 +1980 / −180	124.0

*Measured in µs after P1 arrival.
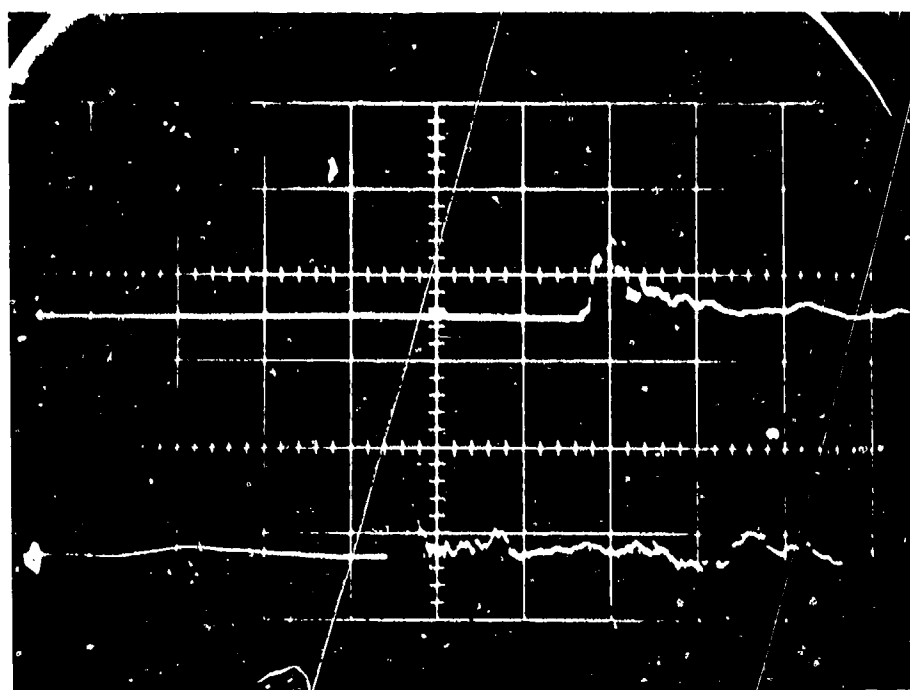
Figure 3.21. Upper trace: Pressure data from Shot FD11 (con-
figuration 2LF, at r=7.5 cm. Note. 10 µs div;
758 bars div. Lower trace: Pressure data at
r 10 cm. 20 µs div; 100 bars div.
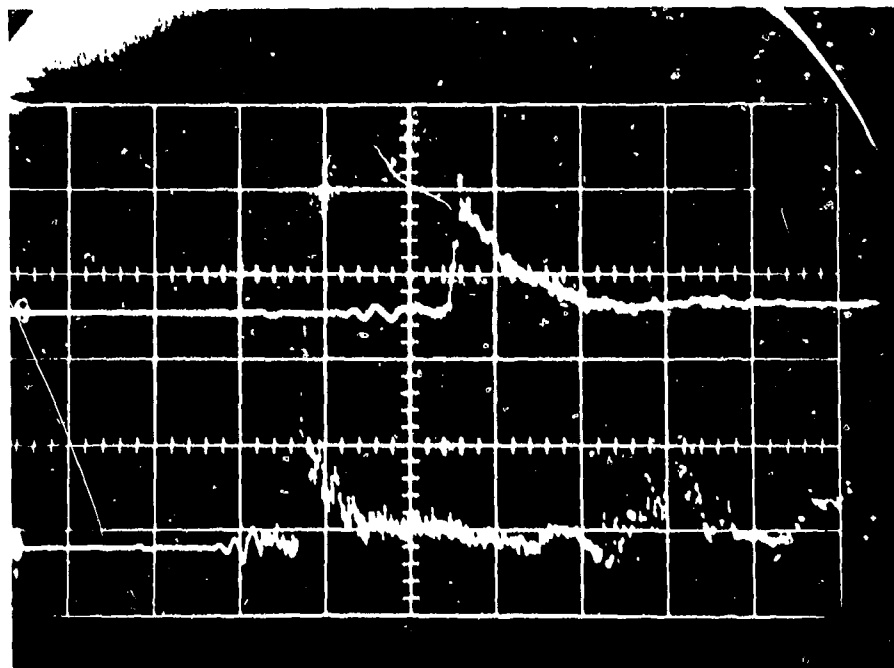
Figure 3.22   Upper trace: Pressure data from Shot FD15
(7S1.98), at r = 75 mm.   10 µs/div; 258 bars/
div. Lower trace: Pressure data atr = 100 mm.
20 µs/div; 106 bars/div.
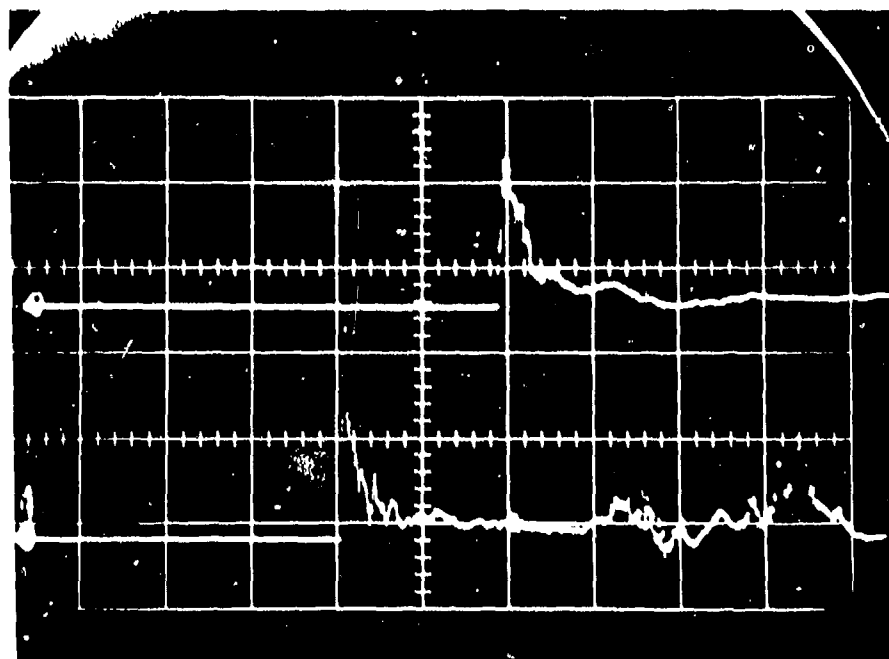
Figure 3.23.   Upper trace: Pressure data from Shot FD16
(7SF1.99), at r = 75 mm.   10 µs/div; 258 bars/
div. Lower trace: Pressure data at r = 100 mm.
20 µs/div; 106 bars/div.
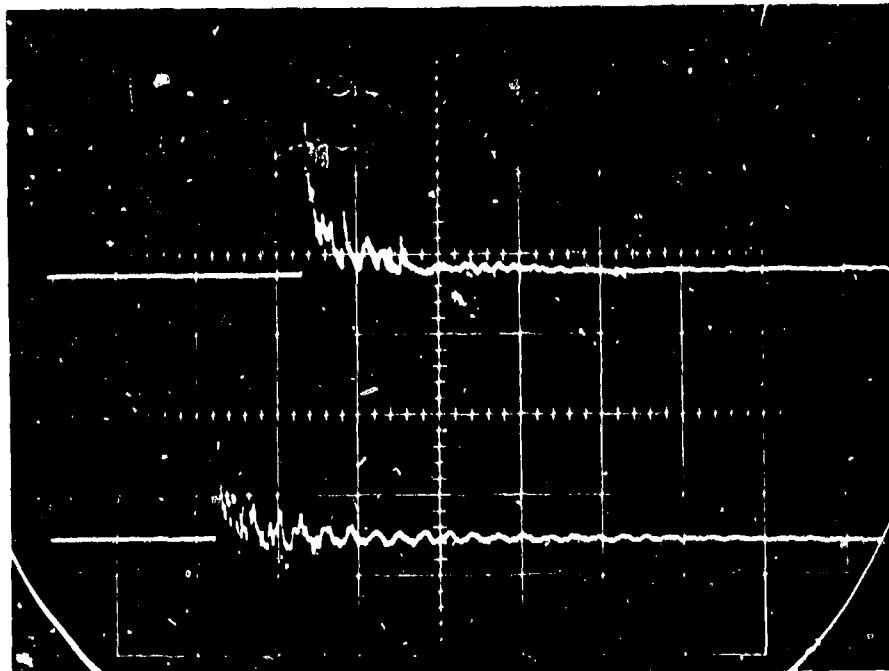
Figure 3.24. Pressure records from Shot FD22 (7S1.74), 50 µs/
division. Note: Upper trace: T_5 transducer, 85
bars/division. Lower trace: T_4 transducer, 657
bars/division.

Table X summarizes the measurements of peak pressure in
Shots FD11 through FD19. We tried plotting the data of
Table X in various formats to help reveal latent empirical
relationships. No outstanding global relationships were iden-
tified. At r = 10 cm, peak pressure varied remarkably little
with configuration or impact velocity; the mean of all the
data was 147 bars, and the standard deviation was only 20 per-
cent. The r = 7.5 cm data contained only slightly more velocity
dependence. For example, at r = 7.5 cm, foam had very little
effect on peak pressure (e.g., Shots 15 versus 16, or 13 and 14
versus 8 and 6). One trend was that at 7.5 cm in plain panels
for similar projectiles, thin panels experience higher pres-
sures than thick ones. This trend is reversed at r = 10 cm.
As observed previously, failure had little effect on peak
pressure.

TABLE X. SUMMARY OF PEAK PRESSURE DATA
(1 ksi=69 bars=6.9 MN/m²)

Configuration	Shot No.	U_0(km/s)	r(cm)	P_1(ksi)	P_2(ksi)	t_1(μs)	t_2(μs)	Failure
<u>7LF</u>	FD11	1.78	7.5	3.60 ± 0.2		1.97 ± 0.15		N
			10	1.52 ± 0.16	1.10 ± 0.85	0.85 ± 0.28	5.22 ± 0.28	N
7LF	FD13	1.58	7.5	3.07 ± 0.21	1.19 ± 0.10	1.13 ± 0.07	4.58 ± 0.14	N
			10	1.93 ± 0.25	1.08 ± 0.16	2.26 ± 0.28	7.34 ± 0.28	
	FD14	1.67	7.5	3.22 ± 0.2	2.45 ± 0.4	1.90 ± 0.14	4.37 ± 0.14	Y
			10	1.69 ± 0.32	1.05 ± 0.09	1.69 ± 0.28	9.03 ± 0.28	
	FD12	1.75	7.5	5.62 ± 0.40	2.62 ± 0.10	1.69 ± 0.14	5.71 ± 0.07	Y
			10	2.40 ± 0.40	1.70 ± 0.16	1.27 ± 0.28	5.93 ± 0.56	
7S	FD15	1.98	7.5	4.05 ± 0.4	3.25 ± 0.2	1.91 ± 0.14	4.37 ± 0.14	Y
			10	2.10 ± 0.4	1.32 ± 0.16	0.99 ± 0.56	9.17 ± 0.56	
7SF	FD16	1.99	7.5	4.73 ± 0.4	1.19 ± 0.40	0.99 ± 0.14	4.30 ± 0.28	N
			10	2.04 ± 0.4	0.76 ± 0.16	0.85 ± 0.56	7.48 ± 0.28	
<u>7S</u>	FD19	1.95	7.5	2.01 ± 0.20	2.70 ± 0.20	1.90 ± 0.28	10.15 ± 0.14	R
			10	1.61 ± 0.4	2.87 ± 0.40	2.26 ± 0.56	18.33 ± 0.28	
					2.44 ± 0.4		17.2 ±0.56	

Configuration nomenclatures are explained in Table I.

P_1 and P_2 refer to first and second peaks.

t_1 and t_2 are time intervals between the arrival of the main signal and the peak pressures.

37

Pressure pulses at the T4 and T5 transducer positions,
which were respectively 10 and 20 cm behind the panel, were
relatively unaffected by the panel construction. Representa-
tive data are shown in Figures 3.24, 3.25, and 3.26. In the
7S and GS records, the main arrival is preceded by shock. The
central frequency of the shock is above the transducer fre-
quency response, so the amplitudes on the traces are not
quantitive. The shock duration was only a few microseconds,
while the main pulse duration was $\sim$40 μs at T_4 and $\sim$75 μs at
T_5. The pressure decayed by a factor of about 4 between those
two gauges; the ratio of radial distance was 1.58. The shock
spike was missing in the data from foam-backed panels (Figure
3.26). There are two possible causes for the spike reduction:
(1) the more immediate shock relief at the foam/fluid interface,
and (2) the fact that the impact stress resulting from steel
striking water is less than the impact stress resulting from
steel striking aluminum which strikes water.
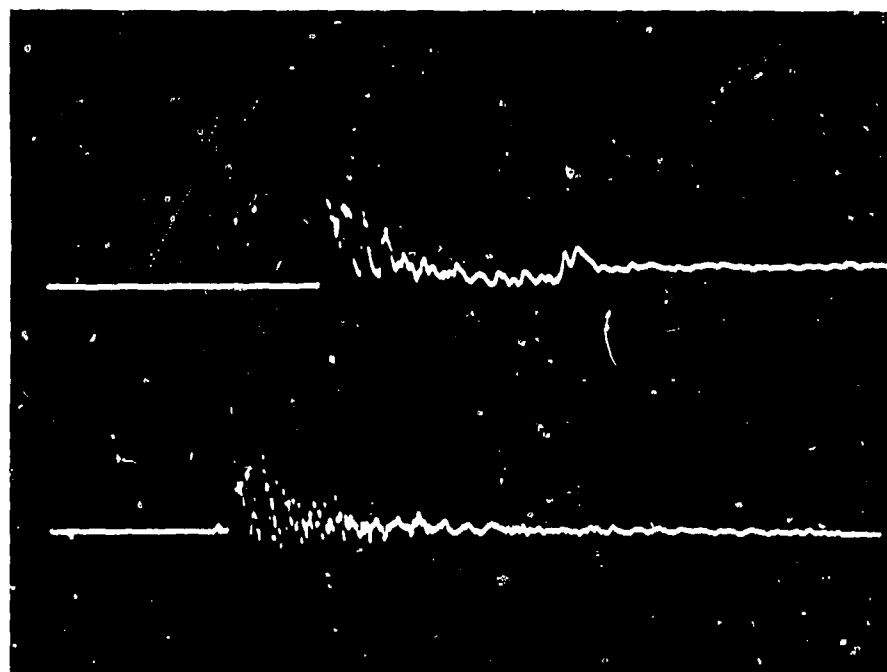
3.25. Pressure records from Shot FD25 (GS1.46), 50 μs/division.
       Note: Upper trace: T_5 transducer, 43 bars/division. Lower
       trace: T_4 transducer, 657 bars/division. Picture magni-
       fication is the same as Figure 3.24.
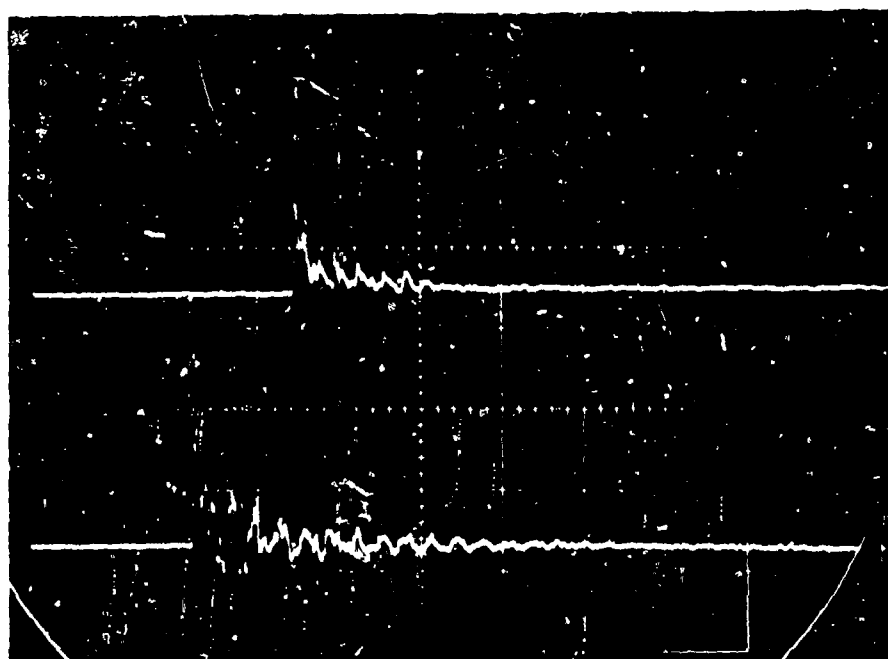
Figure 3.26. Pressure records from Shot FD16 (7SF1.99), 50 μs/division. Note: Upper trace: T_5 transducer, 170 bars/division. Lower trace: T_4 transducer, 657 bars/division.

3.3 DISPLACEMENT DATA

Moiré fringe data were taken for most shots. In general, the data were analyzed for shots in which no failure occurred. In this way, data for peak displacement were obtained that could be compared with the calculations.

3.3.1 Discussion of Thick Aluminum Data

CRT did only one calculation of panel displacement. The calculation corresponded to Shot FD8; hence, the shot was analyzed in more detail than any other shot. Shot FD8 was made with the 7L configuration at a velocity just below the failure threshold. The first eight frames from the moiré fringe record are shown in Figure 3.27.

Figure 3.28 shows the shape of the panel (along a horizontal line) until maximum displacement occurred. The duration of the obscuration due to impact flash was only about 0.5 ms. In places where broad fringes resulted in ambiguous data, dashed lines show alternate interpretations. The maximum

Figure 3.27.   Moiré fringe record from Shot FD8.   The interframe time was 160 μs.
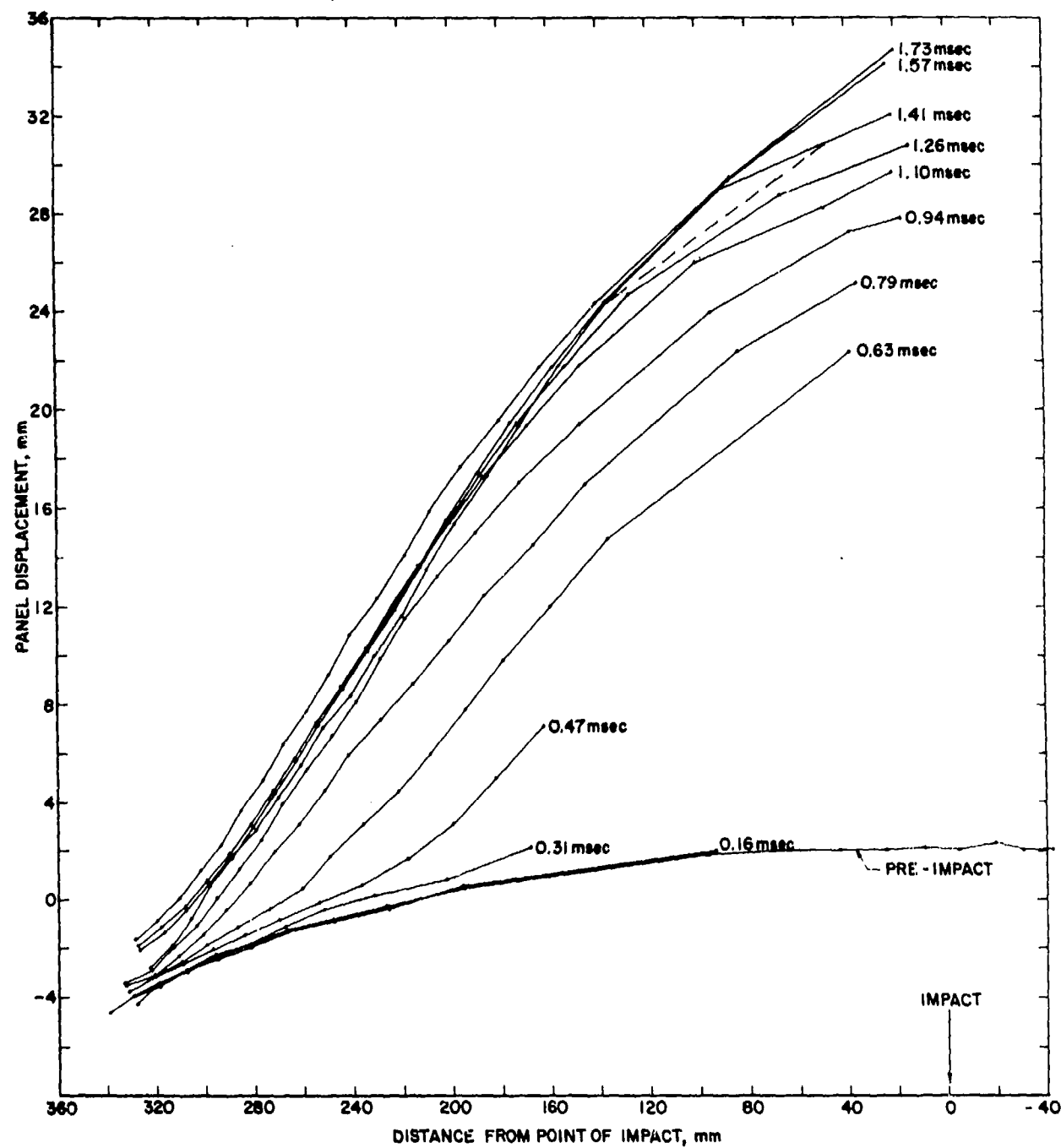
Figure 3.28.   Shape of panel in FD8, up to peak displacement.

41

displacement (with respect to the initial position) was about
35 mm and occurred at about 1.73 ms after impact.

For Shot FD8, the rebound of the panel after
peak displacement was analyzed. This analysis was made possible
by the computer code developed for fringe data reduction
(described in the Appendix). Figure 3.29 shows the shape of
the panel at various times between peak deflection and maximum
rebound. At maximum rebound (7.5 ms), the deflection of the
center of the panel was more than 10 mm below the edges.
During the rebound, as well as during the initial outward
motion, the fastener region steadily moved outward. At maxi-
mum rebound, this region had been displaced almost 7 mm from
its initial position. Considerable care was required for proper
analysis of the fringe photographs when fastener movement
occurred. Figure 3.30 shows the recovery of the panel at
various times after rebound. Negligible additional movement
at the fasteners occurred during this time.

From these data the time-history of the deflection
at various positions can be deduced. This time-history is
shown in Figure 3.31 for three positions: 25 mm to the left
of impact ($r = 25$ mm), 170 mm to the left of impact (halfway
between the impact and the fasteners), and 280 mm to the left
of impact (over the O-ring seal, 18 mm to the right of the
fastener center lines). The initial velocity of the panel near
the impact point was at least 32 m/s.

The deflection at the fasteners was larger than
had been anticipated. The major component of this motion appears
to have been the outward movement of the 25-mm-thick aluminum
backing plate to which the test panel was bolted. No permanent
set appeared in this plate. Therefore, most of the motion must
have been caused by a bulk forward motion of the entire tank.
Net forward displacement of the tank after the shot was noted
in most of the shots. A 10- to 20-mm displacement was typical,
and the displacement was greatest when failure does not occur.

42
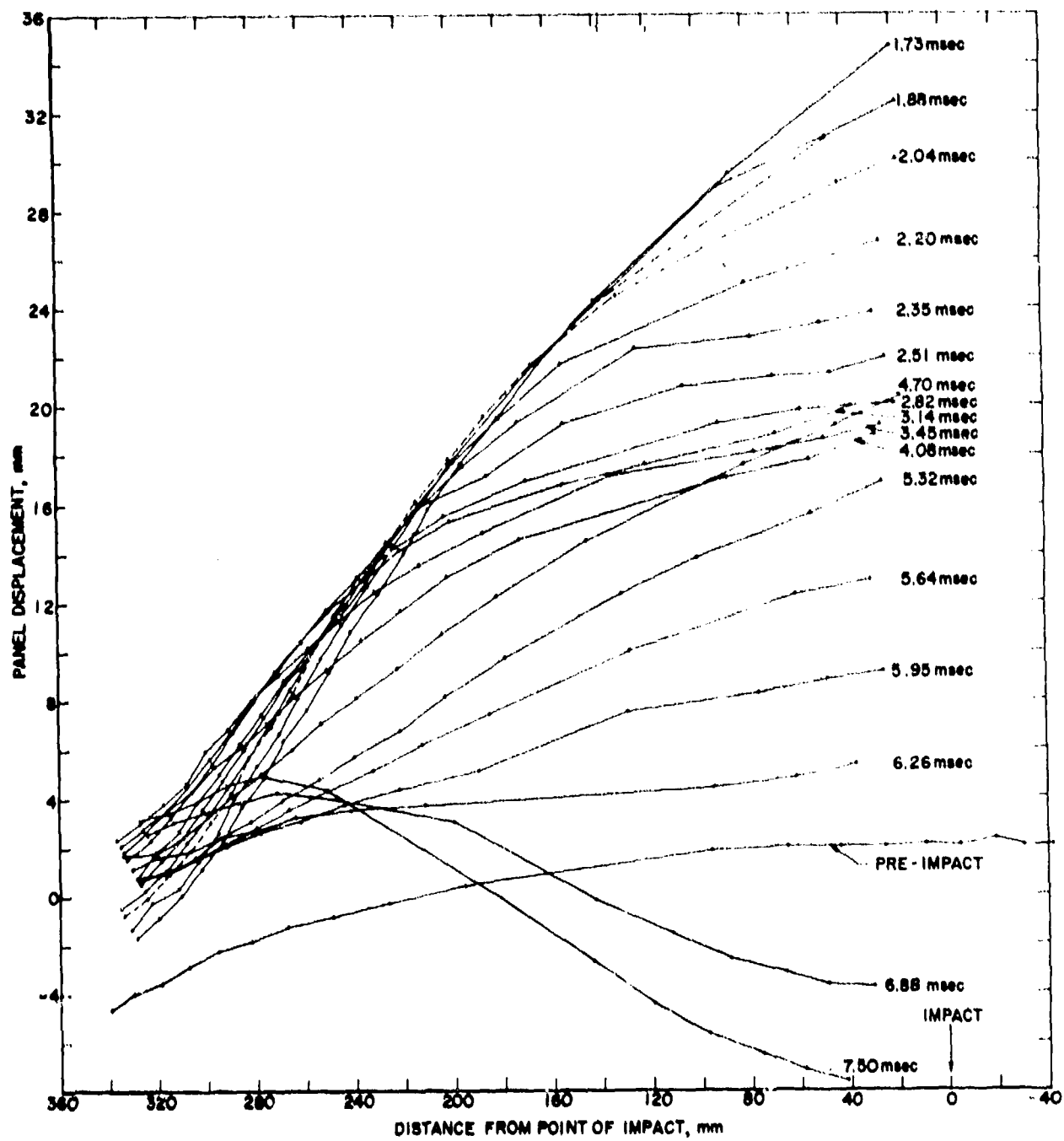
Figure 3.29.   Shape of panel in FD8, from peak displacement to
                maximum rebound.

43
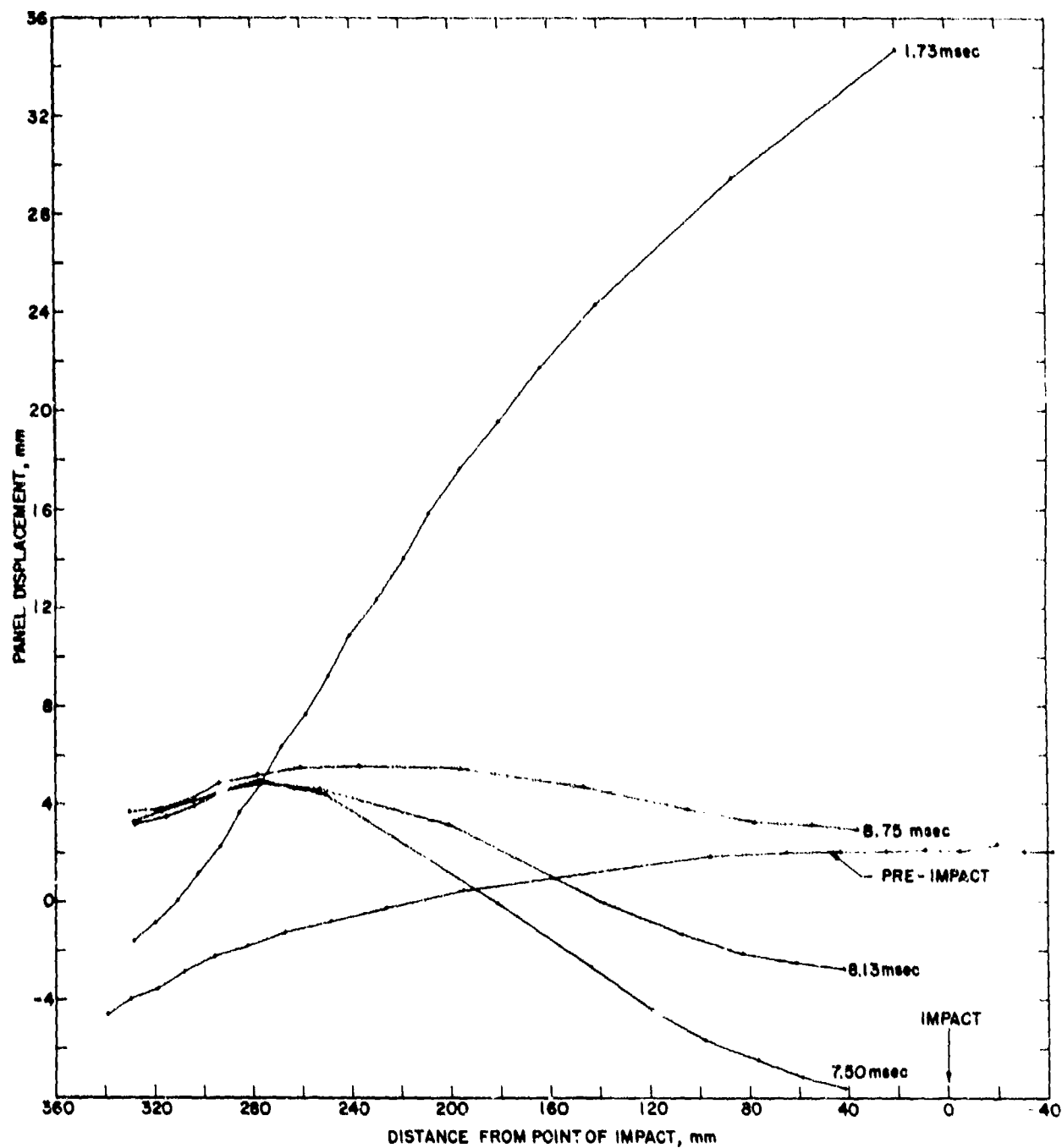
Figure 3.30. Shape of panel in FD8, after maximum rebound.

44
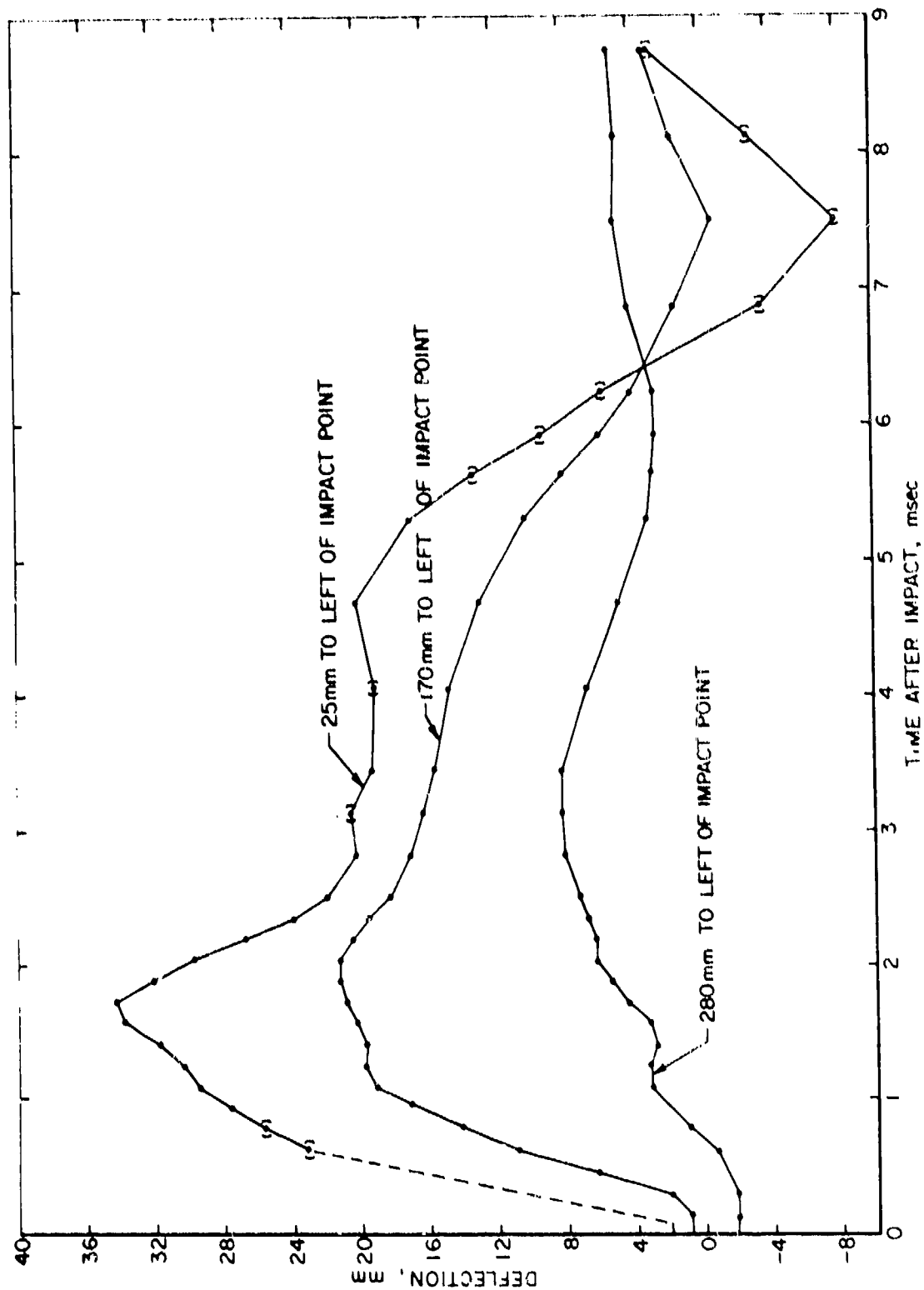
Figure 3.31. Time history of FD8 panel at various positions.

45

Other causes of panel movement at the fasteners could have been bolt stretching and bulging between the fasteners. The fringe records showed no evidence of bulging between the fasteners. However, some bolt stretch was indicated by the condition of the bolts after the shots and by the fact that a tilt of about five degrees developed in the panel in the region to the left of the O-ring seal. (The initial tilt due to hydrostatic bulge was about two degrees.)

During certain time intervals in Shot FD8, water spurted out the sides of the panel at a velocity of ~140 m/s. This leakage could have happened only when the panel had been pushed a sufficient distance beyond the O-ring seal at $r = 280$ mm. Table XI provides a summary of these observations. The appearance or disappearance of the water leakage correlated roughly with the deflection of the panel at the O-ring (see also Figure 3.31); however, it did not correlate well with the tilt of the panel near the O-ring. This indicated either that the movement of the aluminum base plate was relatively small at these times or else that the times of maximum local displacement coincided with times of maximum local water pressure and that chiefly the water pressure caused the defeat of the O-ring.

The deflection of the panel at the edges necessitated a correction of the data when they were compared to the numerical predictions. For example, the peak displacement in FD8 may be expressed as

- 35 mm, relative to the preshot surface (taking into account the initial hydrostatic bulge).
- 40 mm, relative to the plane defined by the pre-impact position of an unbulged panel.
- 35 mm, relative to an unbulged panel whose edges coincide with the deflected panel at the time of peak deflection.
- 30 mm, relative to a hydrostatically bulged panel whose edges coincide with those of the deflected panel.

46

TABLE XI. OBSERVATION OF WATER LEAKAGE FROM SIDES OF FD8 PANEL

	Frame No.	Time (ms)	Displacement* (mm) d_1	d_2
Water Appears	17	2.67	6.2	6.7
Water Stops	29	4.55	6.3	4.3
Water Appears	47	7.37	4.2	1.7
Water Stops	65	10.18	---	---

*d_1 is the displacement at the O-ring, measured from the initial position.

d_2 is the displacement at the O-ring, measured from the horizontal line through the instantaneous position of the edge of the panel.

d_1 and d_2 are at the time that water started over the O-ring.

3.3.2   Displacement Data from Other Configurations

Displacement data available for othe configurations are illustrated in Figures 3.32 through 3.38. When using these figures, consult the caption and note whether the displacement is plotted relative to a vertical plane or relative to the pre-impact surface. Additional data for peak displacement in the graphite epoxy panels are given in Table XII. Figure 3.39 illustrates panel motion when failure occurs; movement is a great deal more rapid than in an intact panel.

The uncertainty in displacement for the FD shots was only about ±0.25 mm. The uncertainty in the FTC shots was somewhat greater, about ±1 mm.

3.3.3   Variation in Displacement

Although the data are not conclusive, it appears that for unstiffened panels the only parameter that had a large effect on displacement was panel material. The graphite epoxy panels and the stiffened panels underwent substantially less displacement than the bare aluminum panels. Our data do not

47
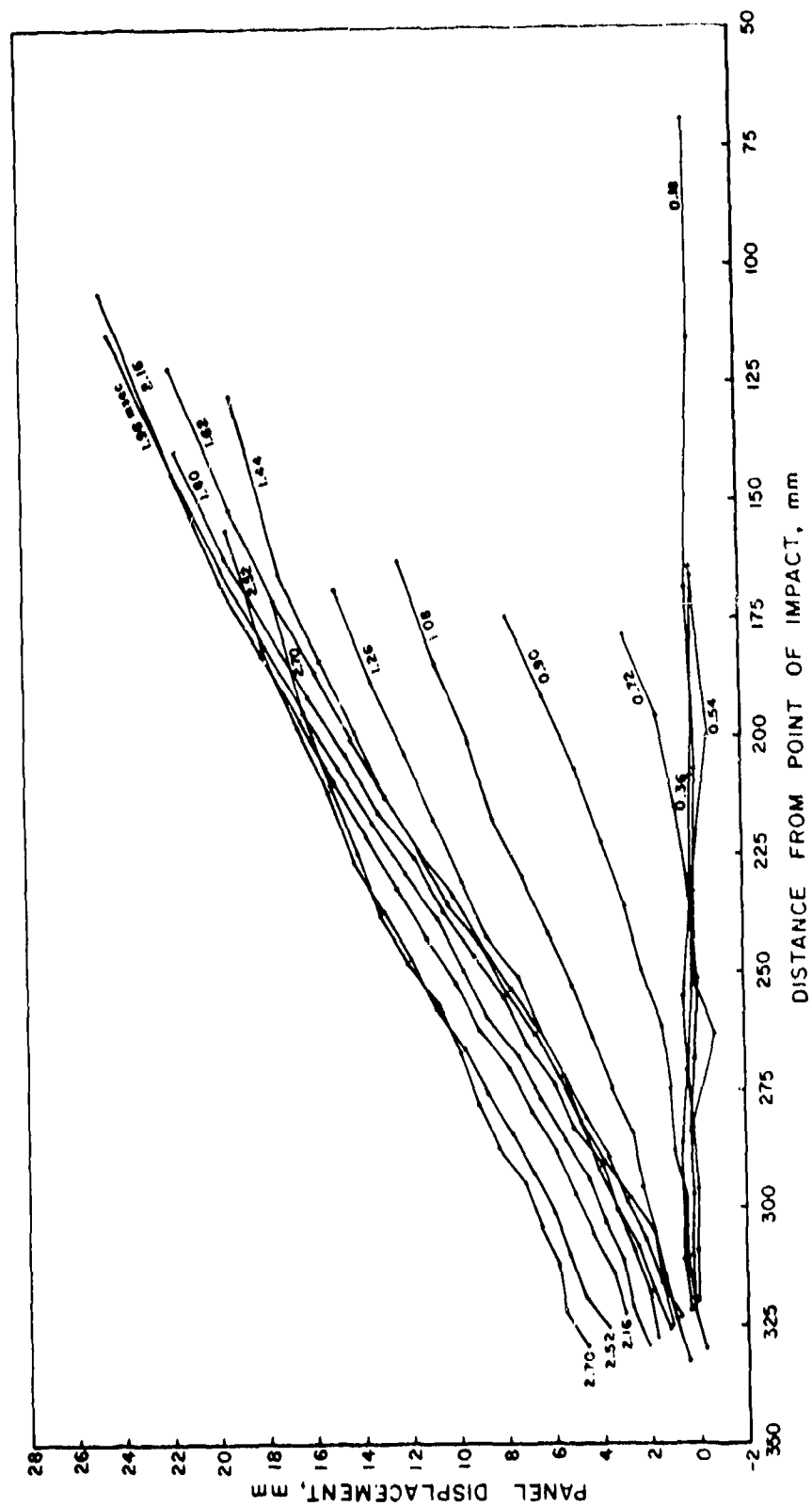
Figure 3.32. Displacement (relative to pre-impact surface) data from Shot FD11 (7LF).
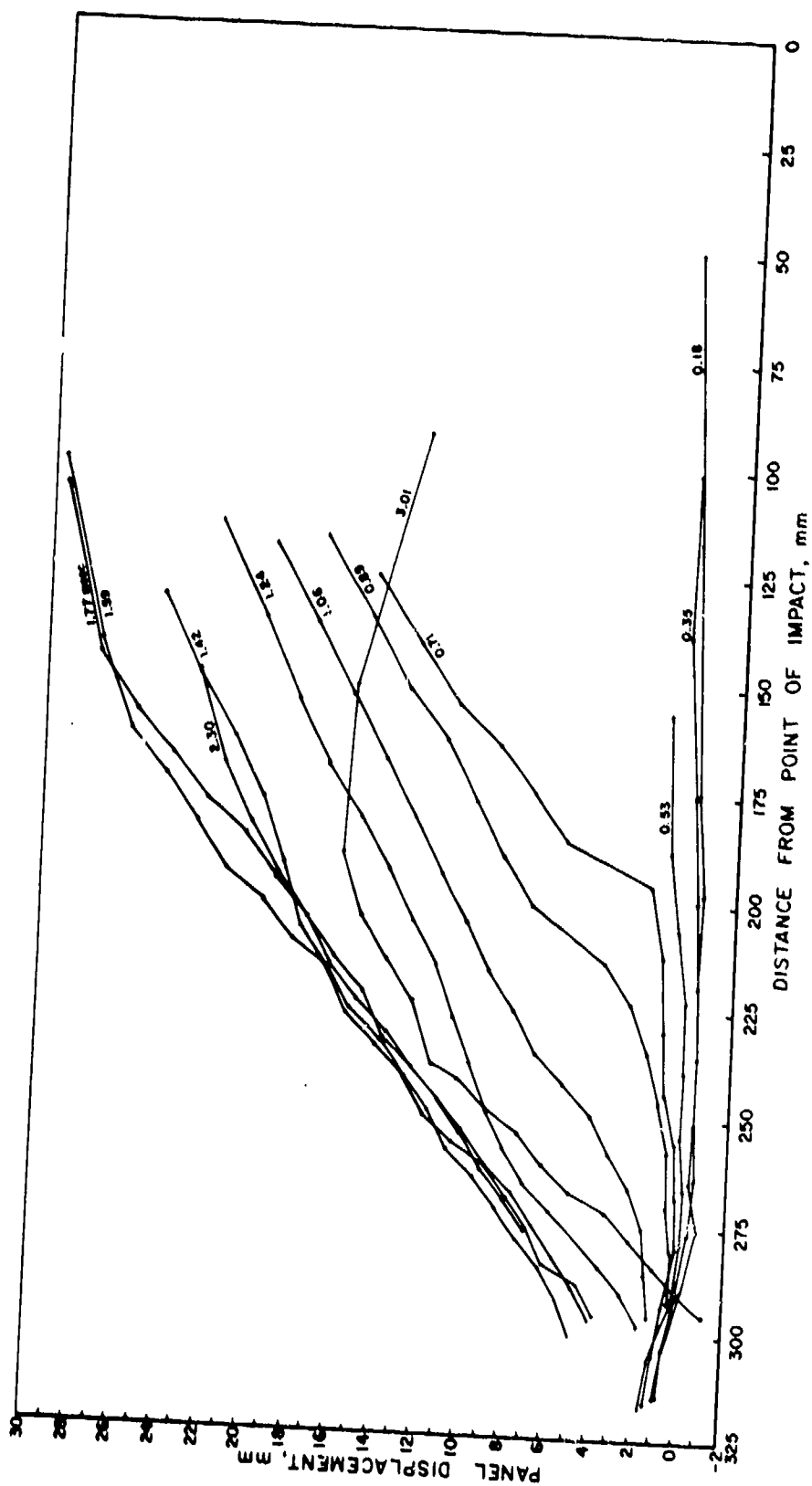
Figure 3.33. Displacement (relative to preimpact surface) data from Shot FD16 (7SF).

49
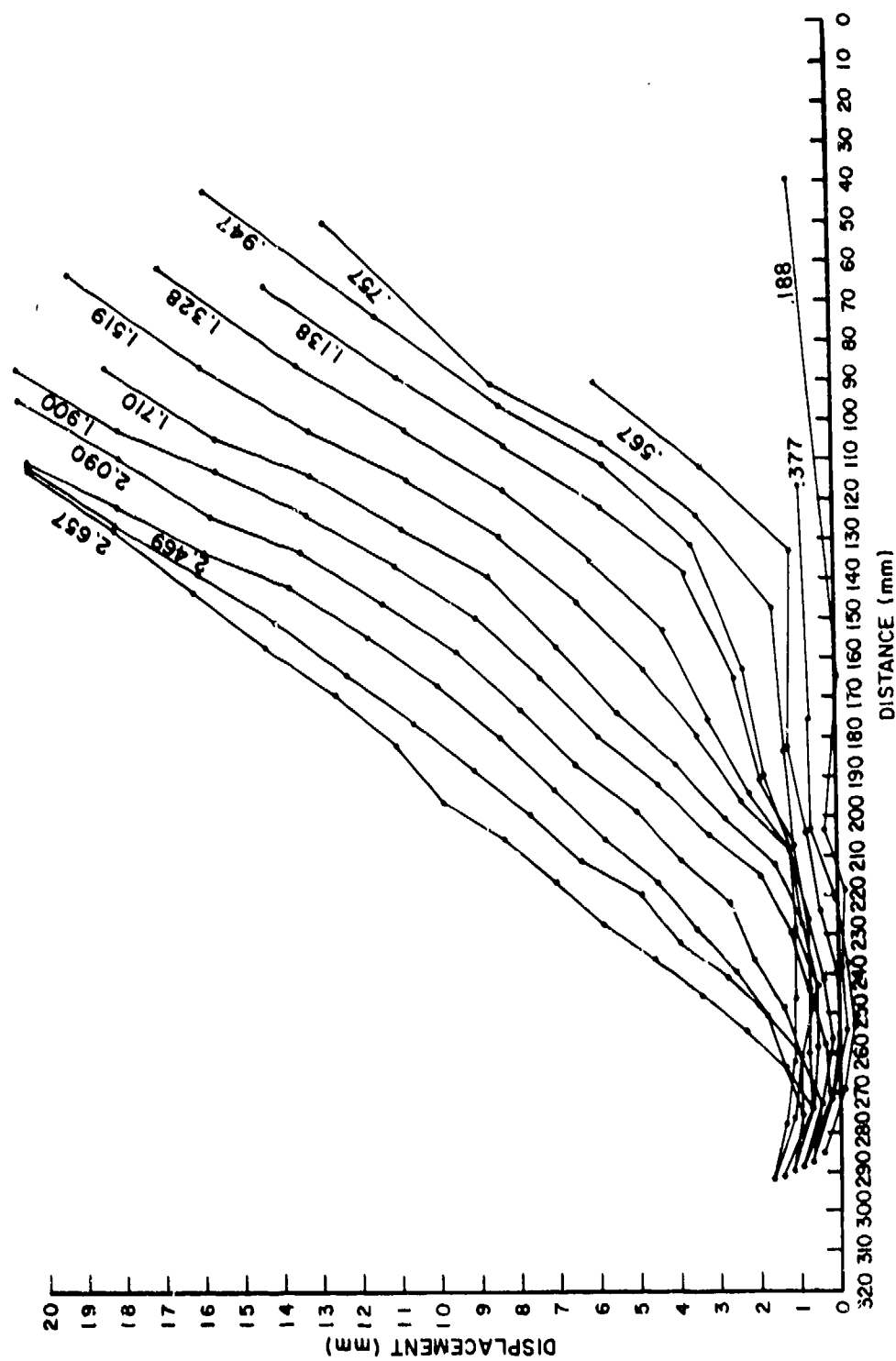
Figure 3.34. Displacement (relative to preimpact surface) data from Shot FD41 (ŜS1.35)
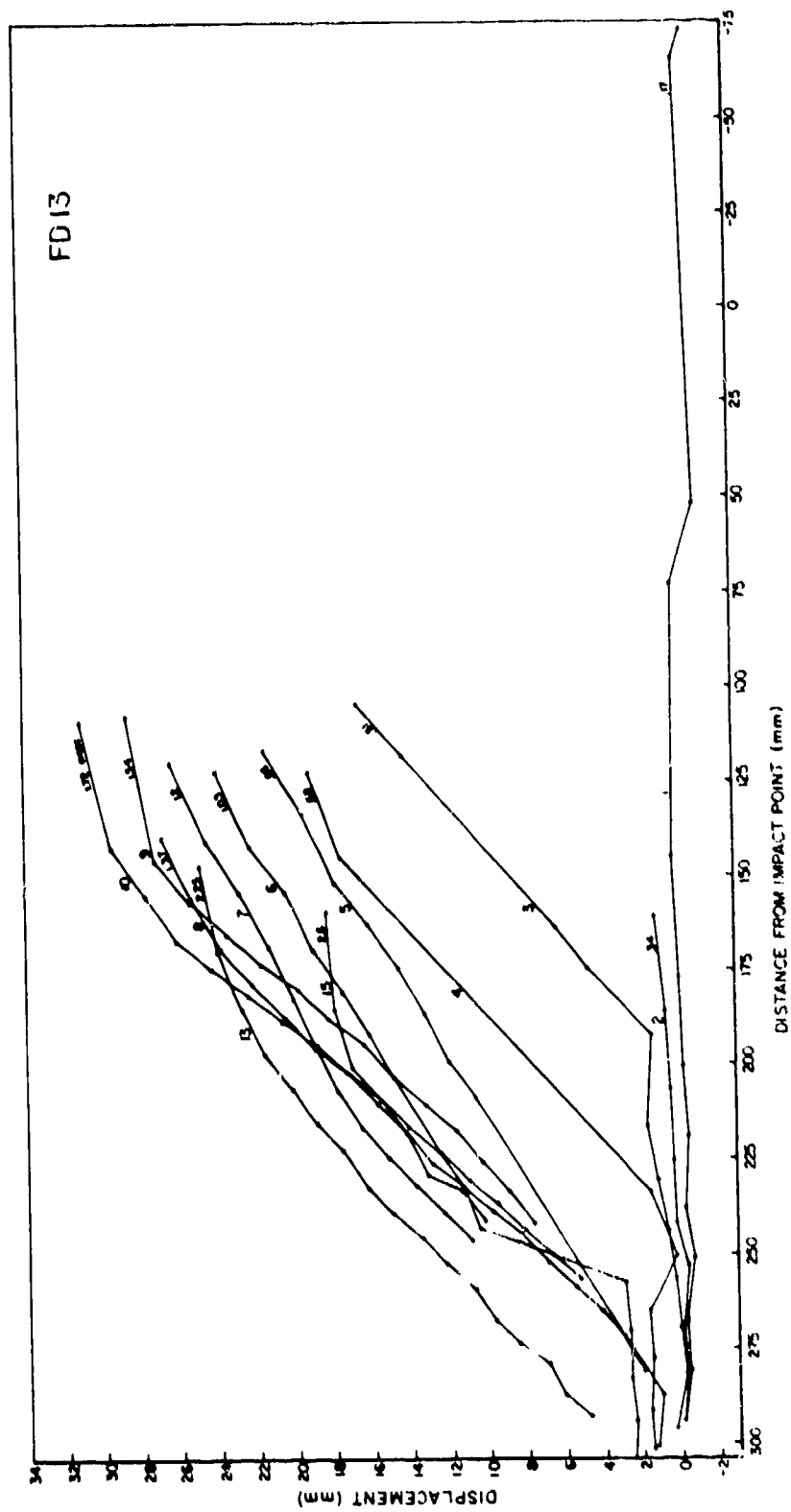
Figure 3.35. Displacement (relative to preimpact surface) from Shot FD13 (7LF1.58).

Figure 3.36. Displacement (relative to preimpact surface) from Shot FD26 (GSF1.69).

52
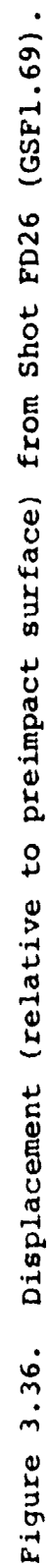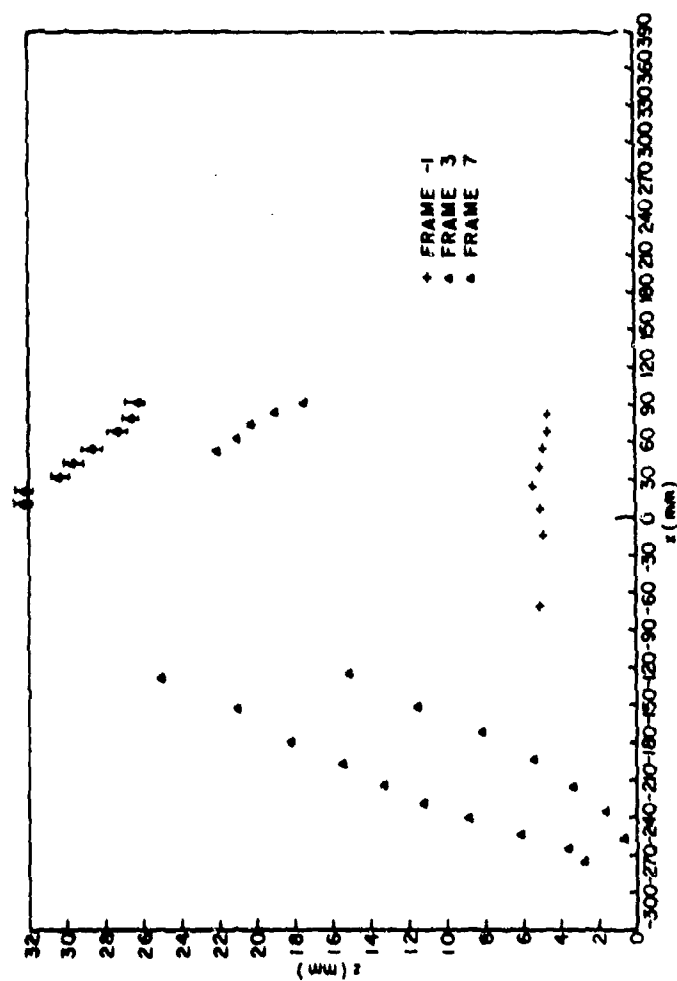
Figure 3.37. Displacement of panel in Shot FTC2 (2S1.55) at selected times before impact (frame-1) 0.645 ms (frame 3) and 1.29 ms (frame 7).

53
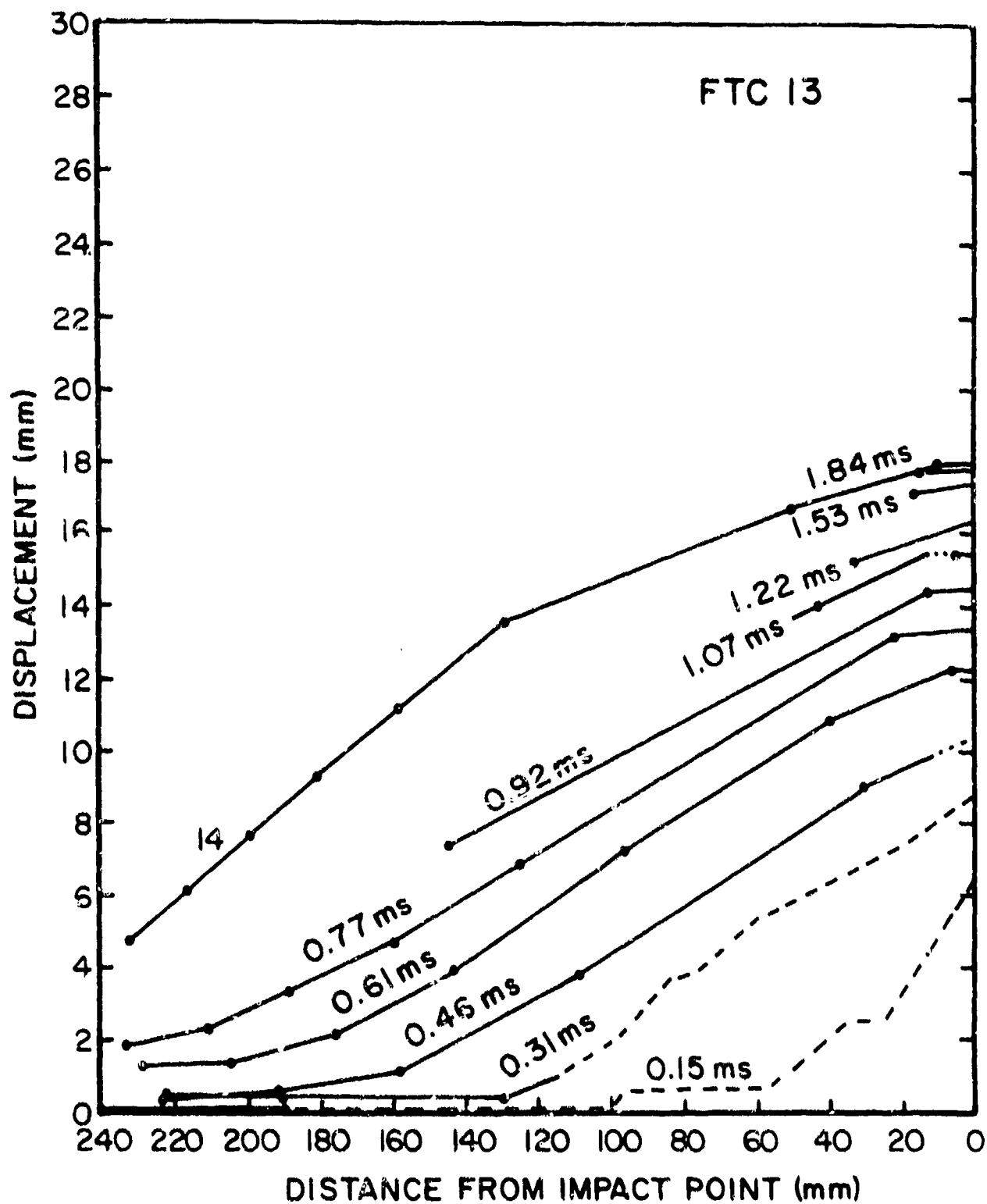
Figure 3.38. Displacement (relative to preimpact surface) from Shot FTC13 (GSF1.18). Numbers indicate frames after impact; average interframe time was 0.153 ms.

54

TABLE XII.   DATA FOR PEAK DISPLACEMENT (RELATIVE TO PREIMPACT SURFACE) IN GRAPHITE EPOXY PANELS.   PROJECTILE WAS 5.67-g SPHERE

Shot No.	Panel Thickness (mm)	Foam Thickness (mm)	Impact Velocity (km/s)	Peak Displacement (mm)	Time of Peak Displacement (ms)
FTC4	3.18	0	0.96	12	1.4 - 1.5
FTC6	3.18	0	1.01	16	1.5 - 1.8
FTC8	4.76	0	1.11	22	
FTC9	4.76	0	1.36	22	1.4 - 1.5
FTC11	4.76	11	1.65	21	1.5 - 1.8
FTC12	4.76	11	1.98	26	1.7 - 2.0
FTC13	3.18	11	1.18	17	1.4 - 2.1
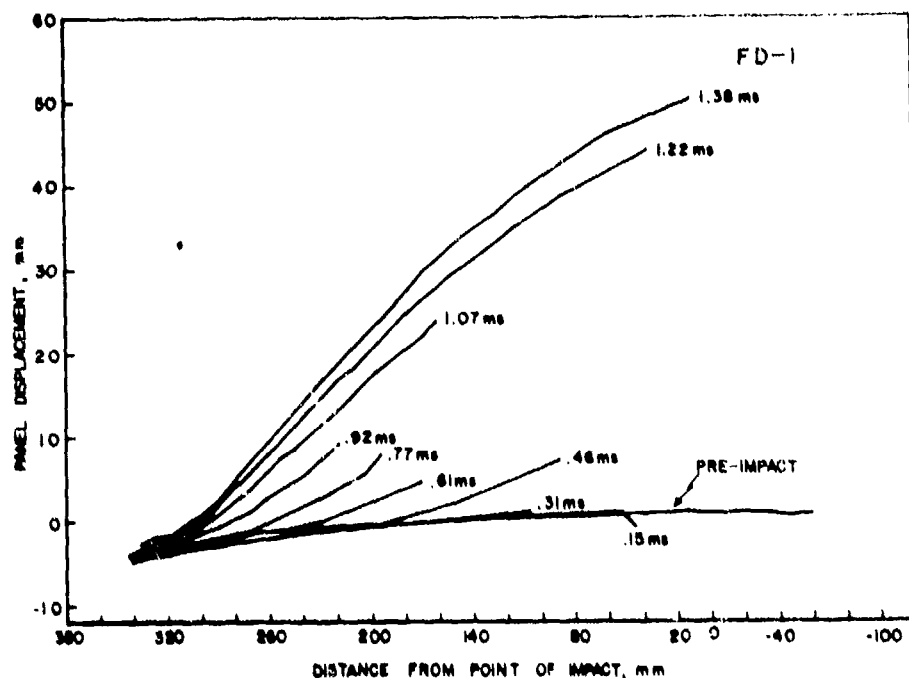
Figure 3.39.   Panel displacement along the torn flap in Shot FD1 (see Figure 3.4 for post-shot view).

allow a direct comparison of displacements from two impacts
differing only in thickness. The effect of panel thickness and
strength may be suggested by a comparison of data from FTC2
(1.6-mm-thick 2024-T3 aluminum) and from FD8 (6.35-mm-thick
7075-T6 aluminum). These shots were fired at similar velocities,
although for FTC2 a 5.7-g sphere was used and for FD8 a 11.7-g
cube was employed. The displacements in these two shots were
almost within experimental error of one another: 33 mm in FTC2
and 31 mm in FD8. The time of peak displacement was only about
200 μs later in the thick 7075-T6 panel than in the thin 2024-T3
panels. Although the maximum displacement was less in the
graphite epoxy panels, the early-time shapes of these panels
were nearly the same as those of aluminum panels, as can be
seen from Figure 3.40. Figure 3.41 illustrates the early-time
motion of a foam-backed graphite epoxy panel. The initial
velocity was ∿40 m/s.
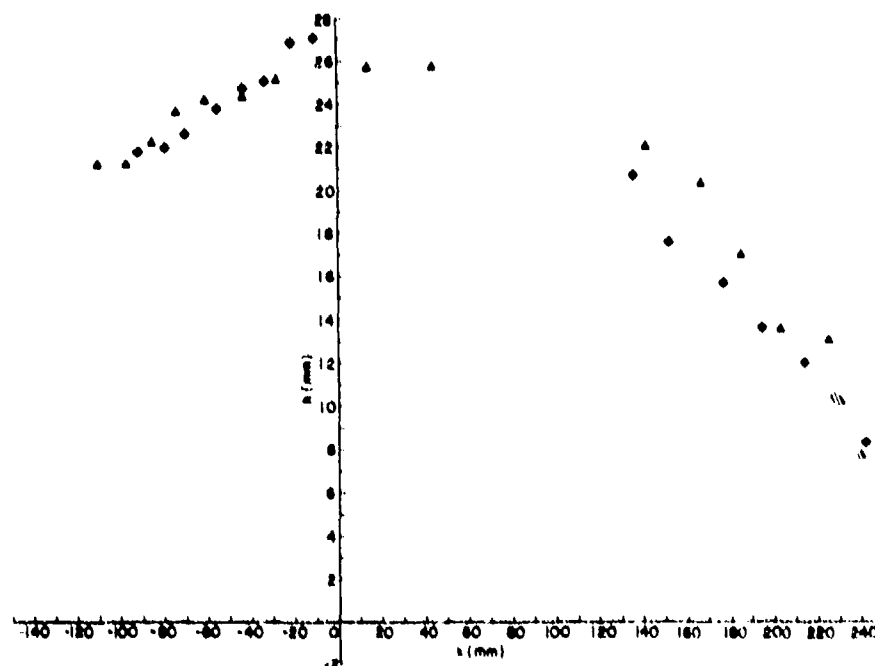
Figure 3.40. Comparison of relative displacement of graphite/
epoxy panel of FTC12 at 1.79 ⊦ .03 ms with
aluminum panel of FTC2 at 1.29 ∔ .08 ms.

56
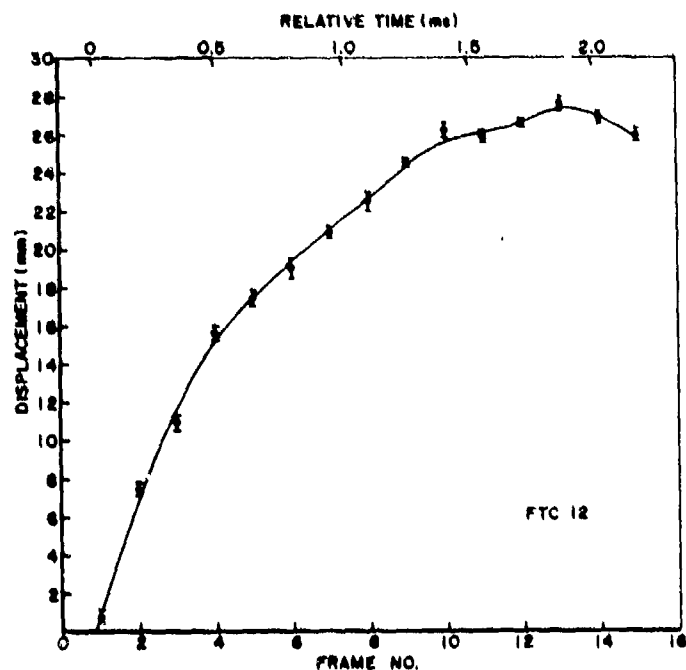
Figure 3.41. Displacement at impact point for Shot FTC12.

        Foam had little effect on peak displacement. For
example, shots FD8 and FD11 had peak displacements within 7.5
percent of one another at r = 125 mm. However, the foam panel
moved slower; it reached its peak at about 1.98 ms, compared
to 1.73 ms for the aluminum panel. Similar observations can
be made regarding FTC9 and FTC11; the foam did not produce a
measurable reduction in peak displacement.

        Few data are available for the dependence of peak
displacement on impact velocity because high velocities caused
the panels to fail. In the GS shots, peak displacement increased
5 mm between V = 1.11 and V = 1.36 km/s. However, the relative
insensitivity of displacement with respect to other parameters
noted implies that at higher velocities the displacement of
aluminum panels would not vary much with velocity.

        On Shot FD41, two strain gauges were bonded onto
the front of the stiffened panel (configuration 2S1.35). A
hoop strain gauge was placed at r = 69 cm and a radial strain
gauge, at r = 78 mm. The records are presented in Figure 3.42.

57
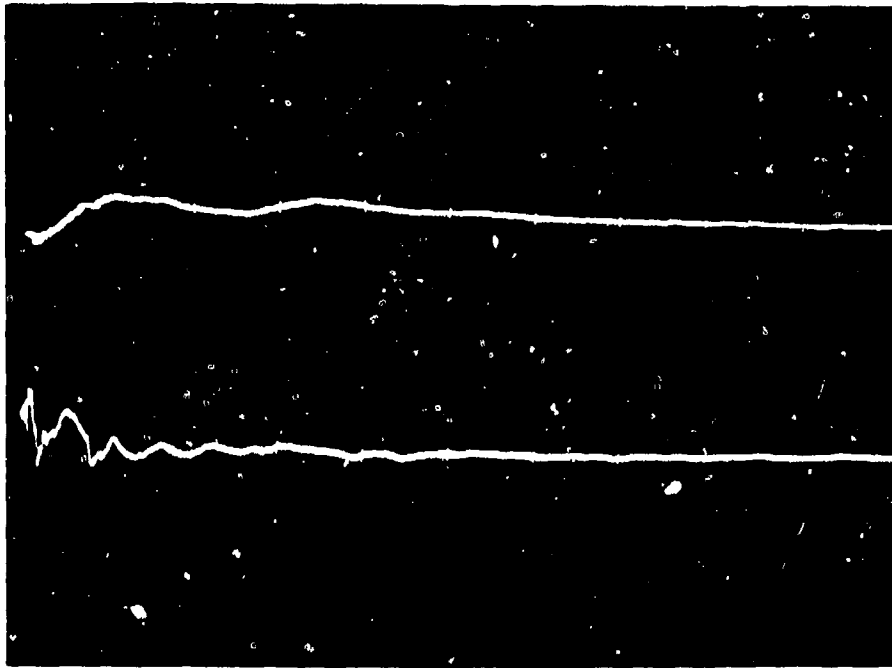
Figure 3.42. Strain record (Shot FD41 (2̂S). Top trace, hoop
             strain; bottom trace, radial strain. Sweep is
             0.5 ms/div. Scale is 1 percent strain/div.

The hoop strain record shows an arrival at ∿50 μs
and attainment of maximum strain at about 0.5 ms. The maximum
hoop strain was about 0.5 percent. Strain maximum occurred
later than the time of maximum displacement (shown in Figure
3.43), which was at 2.7 ms. There was a plateau in hoop strain
at ε_Θ = 0.4 percent at 0.22 ms after impact. The maximum strain
expected is of order 2 (maximum deflection/panel radius)^2 ∿2
percent. We conclude that a bond failure probably occurred,
and measured ε_Θ is unreliable. The radial strain gauge shows
ringing, as has been observed by other investigators who have
strain gauged panels.[1] The radial strain transient occurred
too fast to be resolved on the oscillograph; the final radial
strain, achieved in about 0.5 ms, was also about 0.4 percent.
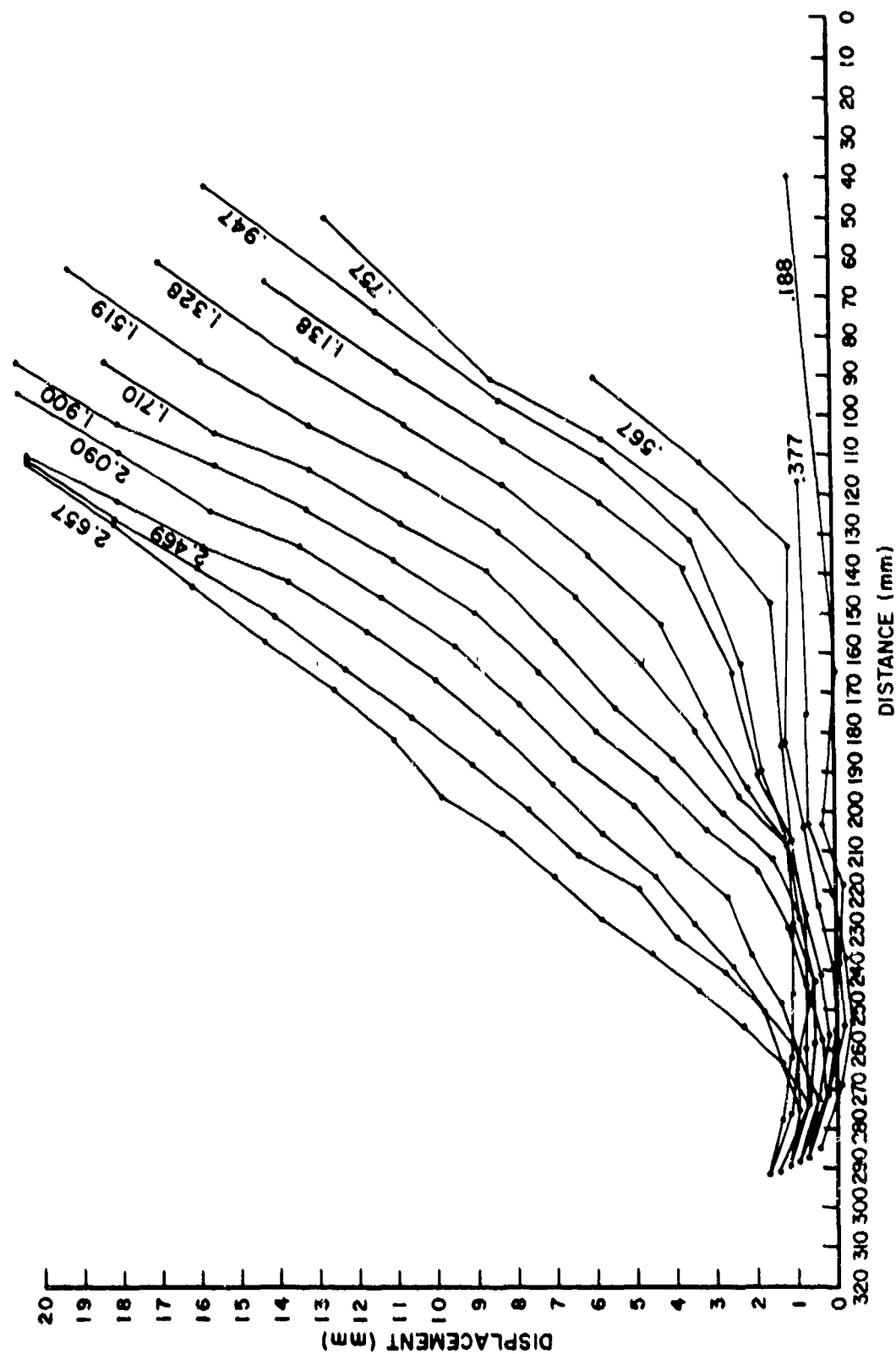
Figure 3.43. Displacement (relative to preimpact surface) at various times for Shot FD41 (2s1.35).

SECTION IV
SUMMARY OF ANALYTICAL RESULTS

Finite difference and finite element analyses of hydro-
dynamic ram phenomena were performed by CRT under subcontract
to the University. Details of the numerical approach and
results are described in Part II of this report. In this
section we summarize and comment upon what we believe to be the
most important features of the CRT numerical analysis.

The goals of the numerical effort were as follows:

(A) Refine techniques for calculating entrance-
     panel loading functions, using the CRALE
     finite-difference code.

(B) Refine techniques for calculating entrance-
     panel structural response, using the NONSAP
     finite-element code.

(C) Use the results of A to generate design data
     for entrance-panel loads.

(D) Use the results of A through C to refine
     techniques of predicting failure thresholds
     and to apply prediction techniques to
     generate design data for failure of panels
     penetrated by threats of interest.

(E) Use the results of A and C to develop design
     data for entrance-panel displacement.

We originally intended to generate design data using
numerical techniques almost exclusively. The main purpose of
the experiments was to provide validation of the numerical
techniques. Specifically, we felt that code credibility could
best be established by demonstrating the code's ability to
predict failure thresholds, pressure profiles, and displacement

60

histories. These quantities were measured for key configura-
tions, and CRT was not informed of experimental results until
after predictions had been submitted to the University.

The success of the numerical approaches was mixed. Tasks
A, B, and C were satisfactorily accomplished. Task D was not
successful; however, the results of Task D were very valuable
in interpolating and in extrapolating the limited experimental
data set to provide design data for failure thresholds. Task
E was partially successful; however, at this time it is still
more accurate and convenient to base design data on the experi-
mentally measured displacements.

4.1 RESULTS OF PRESSURE PREDICTIONS

The analytical predictions of pressure were based on an
axially-symmetric finite-difference representation of the
entrance panel and water. The projectile was modelled as a
rigid sphere. The arrival times and general form of the pre-
dicted pressure pulses were satisfactory. In the initial
calculations, the peak pressures were much too low. Figure 4.1
illustrates a typical comparison of the numerical and experi-
mental results. The calculated peak pressures were often a
factor of two below the experimental data. However, the
calculated impulse values were reasonably accurate (see below).
In order to provide loading functions for finite-element
calculations were approximated by more convenient and simple
analytical models. The model was fit to the pressure at
$z = 6$ mm. In the model, pressure is a function of time, t; and
radius, r, given by a triangular shaped function that arrived
in time, T_1, peaked at T_2, and decayed exponentially beyond
T_3 with a decay constant equal to T_4 as shown in Figure 4.2.
The maximum pressure was given by

$$P_m = 3.0 \ D^2 W^{.25} VR^{-(2+.4W)} \tag{3}$$

where P_m is in kbar (and the other units are cm and µs) and
the times were given by
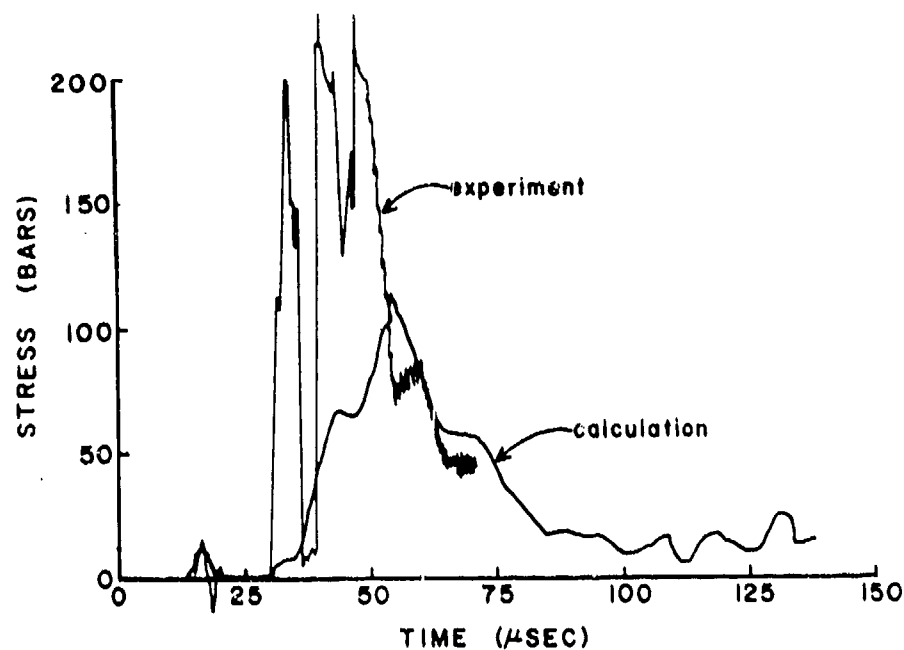
Figure 4.1. Comparison of measured and predicted pressure
profile for the r = 75 mm pressure station from
Shot FD8.
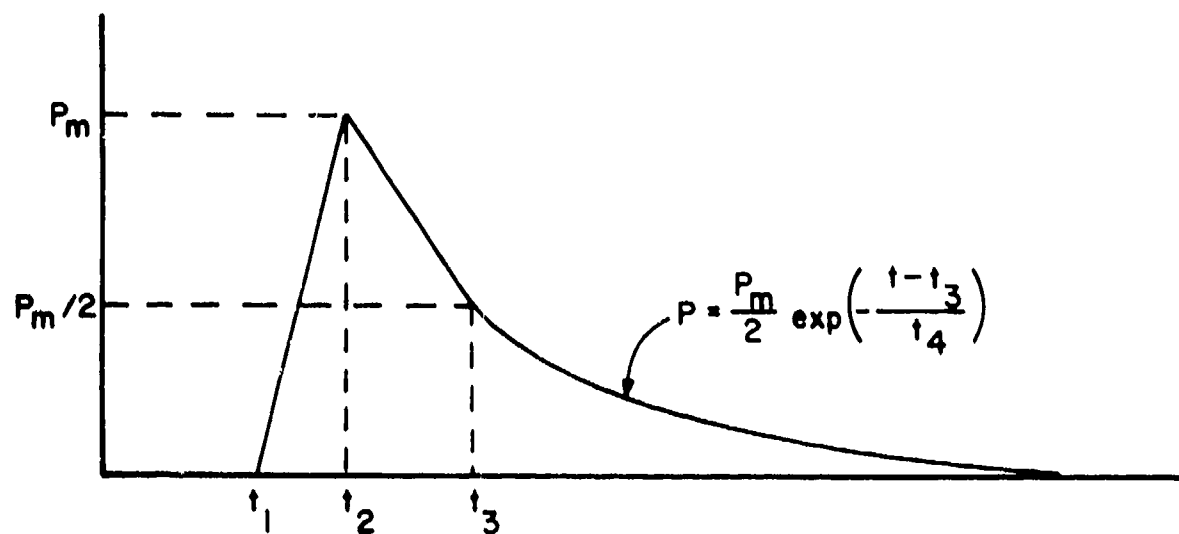
Figure 4.2. Form of loading pressure in analytic model.

$$t_1 = 5 \ (r - D/2) \tag{4}$$

$$t_2 = (6.4 + 2.1W) \ (r - D/2) \tag{5}$$

$$t_3 = t_2 + 12.6W \tag{6}$$

$$t_4 = \frac{2}{P_m} \ [I_{max} - I \ (t < t_3)] \tag{7}$$

$$I \ (t < t_3) = 0.5 \ P_m \ [t_2 - t_1 + 1.5 \ (t_3 - t_2)] \tag{8}$$

where I_{max} is the total impulse, in bar-s, given by

$$I_{max} = 0.0165 \ D^{.8} \ W^{.45} \ V^2 \ e^{-.365R} \tag{9}$$

The function described by equations (3) through (9) was compared with the experimental data. Figures 4.3 and 4.4 show typical comparisons for thick and thin panels. The numerical pulse arrival times durations, and impulses are in satisfactory agreement with the data.

The data are compared with the predicted impulses in Figure 4.5. The 7S1.35 configuration was chosen as a base, and data from other configurations that differed from 7S1.35 in only one parameter are "mapped" using the scaling implied in Equation 9. Table XIII explains the symbols used in this and subsequent figures. The solid line in the figure shows the loading function used by CRT to derive the structural response model (Equation 9). The dashed line illustrates constant impulse beyond $r = 10$ cm, as assumed in some of the finite element calculations.
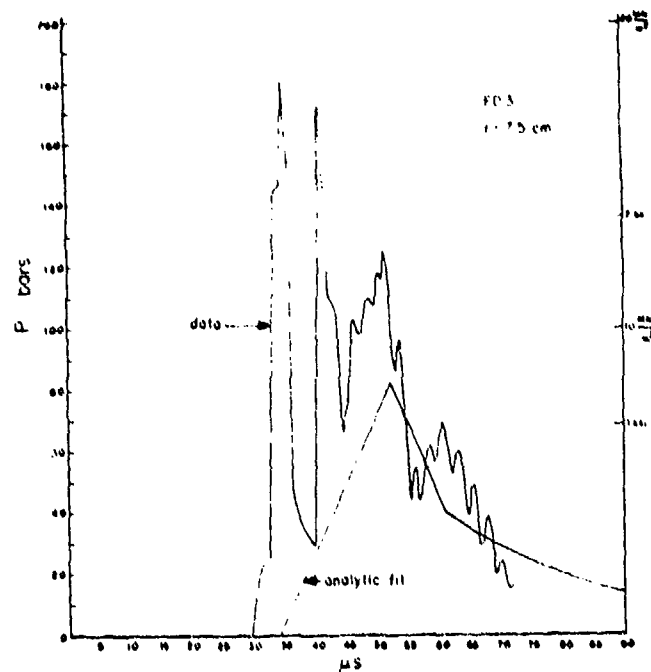
Figure 4.3.   Comparison of experimental and model pressure
histories for FD3, 7L1.42, at r = 7.5 cm.
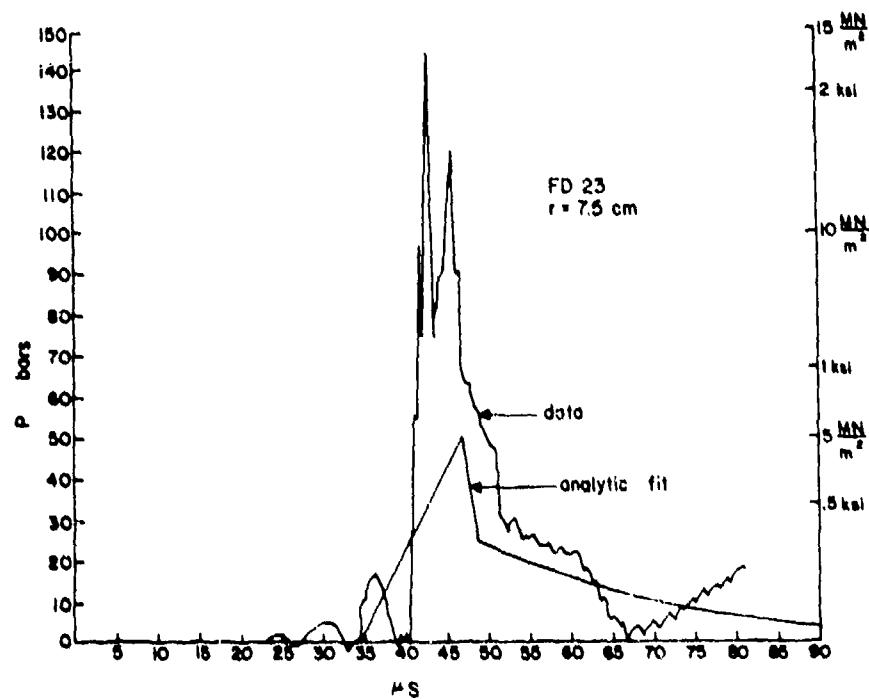
Figure 4.4.   Comparison of experimental and model pressure
histories for FD23,7S1.35   at r = 7.5 cm.

64
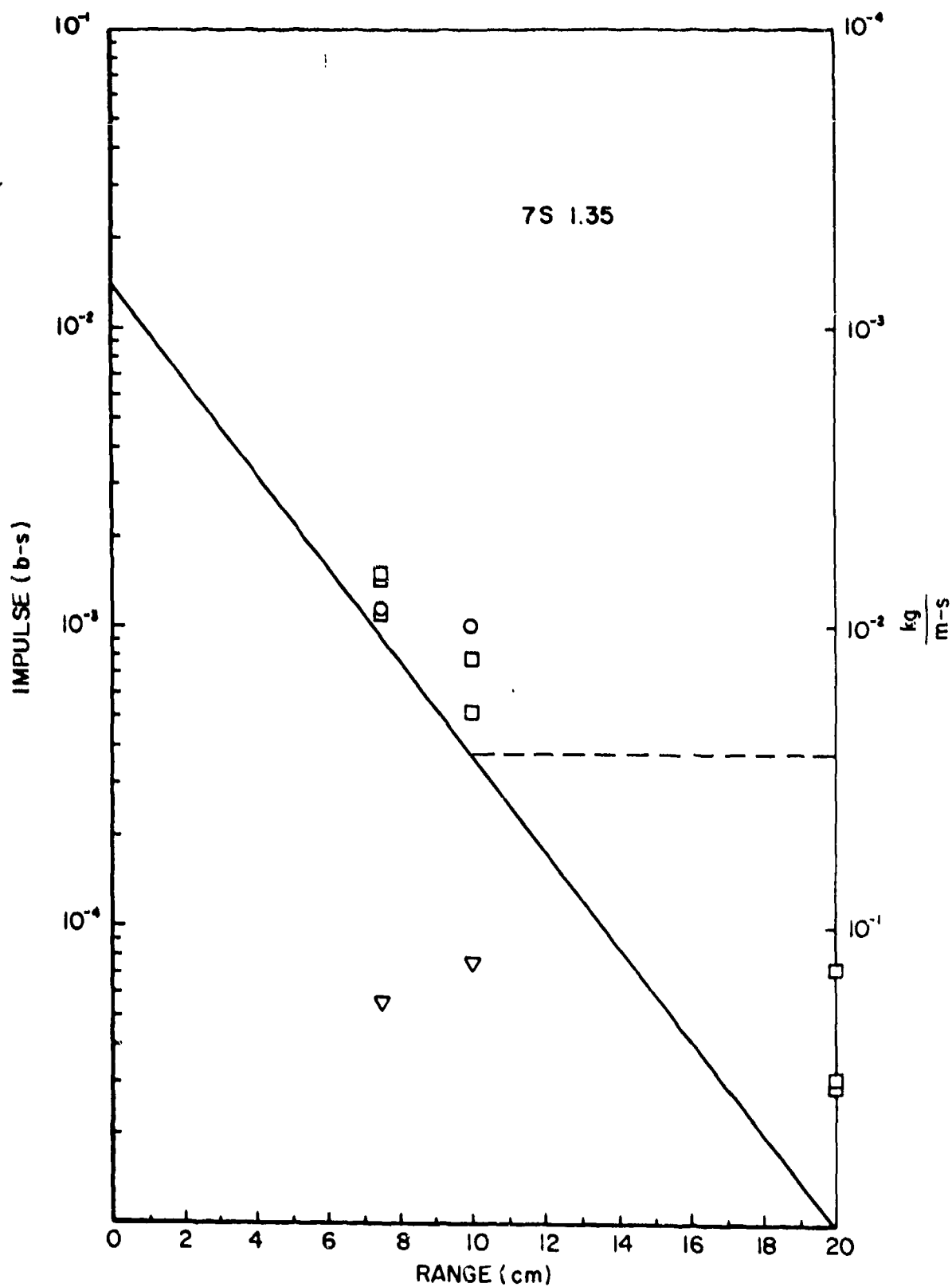
Figure 4.5. Comparison of analytical model (Equation 9) and experimental data for impulse in the 7S1.35 configuration. Note: See Table XIII for explanation of symbols.

TABLE XIII.   EXPLANATION OF SYMBOLS USED IN FIGURES 4.5, 4.7, AND 4.8

   ◯ Datum from shot that was base configuration

   ▢ Datum from shot that differs from base only in impact velocity

   △ Datum from shot that differs from base only in projectile size

   ▽ Datum from shot that differs from base only in panel areal density

   ✳ Numerical value from finite difference calculation

The analytic model falls close to the measured values (being low by a factor of less than two at 7.5 to 10 cm). At 30 cm the data fall between the two models used by CRT. The impact velocity scaling of the model (V^2) seems to fit the data satisfactorily; however, the panel thickness scaling seems to use an exponent that is too high. When the impulse measured in a thick panel shot (in this case Shot FD19, 7S1.95) was scaled to a thin panel configuration, the results were much lower than those actually observed in thin panel shots. Better scaling would be achieved with an exponent of -1. When the 7L data were compared with Equation 9, they were found to fall below the prediction by a factor of two or three. Perhaps as much as half of this descrepancy may be due to the truncation of the experimental record due to the presence of noise. Thus, the model overpredicts impulse by a factor 1.5 to 2. For many applications this is unacceptable. Thus, an improved model was also developed, as discussed below.

The data do not justify the assumption that impulse is constant beyond 8 cm.

After the first model was formulated, CRT completed additional calculations for other configurations and repeated some

earlier ones with finer zoning. CRT also analyzed the varia-
tion of pressure pulses with distance behind the target panel
(z). Consideration of these calculations and additional
experimental data led CRT to revise the analytic loading model.
The revised model is formulated for z = 1 mm. In this model,
pressure rose linearly to a maximum value, P_m and then decayed
with a time constant t_3. The model is defined by the following
equations

$$P_m = 3.68 \; \delta \; V \; (R´/R_p)^{-\alpha} \tag{10}$$

$$\alpha = 1.15 + 0.6 \; \exp \; (-0.72 \; \rho_t W) \tag{11}$$

$$I = 0.03 \; \delta \; V \; \exp \; (-\beta R´/R_p) \tag{12}$$

$$\beta = 0.185 + 0.35 \; \exp \; (-0.63 \; \rho_t W) \tag{13}$$

$$t_2 = W/V + 6.25 \; (R - R_p) \tag{14}$$

$$t_1 = t_2 - (2W/0.63 + 1) \tag{15}$$

$$t_3 = \min \begin{cases} I/P_m - 0.5 \; (t_2 - t_1) \\ 10 \end{cases} \tag{16}$$

$$\delta = \sqrt{R \; \frac{1}{r}} \tag{17}$$

$$R´ = \begin{cases} r & r \le 10 \\ 10 & r > 10 \end{cases} \tag{18}$$

The units used in these equations are centimeters for
length, g/cm^3 for density, kbar for pressure, and bar-seconds
for impulse. (Conversion factors are provided in the Preface.)
The behavior of Equations 10 - 18 is relatively simple. Impulse
decreases exponentially with range for r < 10 cm. The pressure
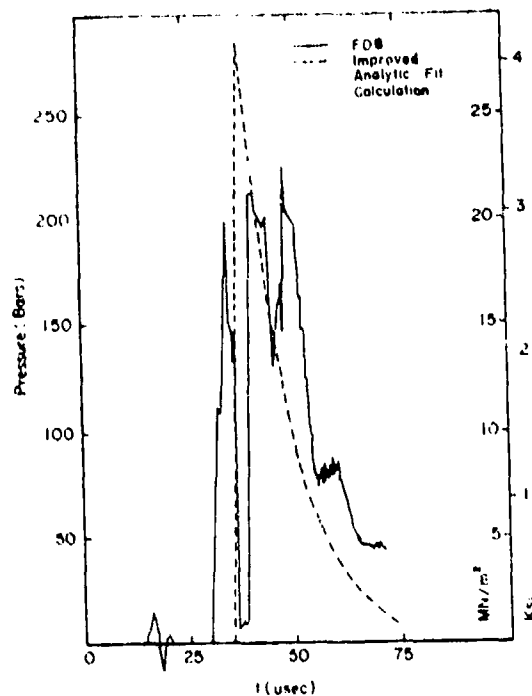
Figure 4.6. Comparison of experimental data from FD8 (7L1.63) at r=75 mm with improved analytic fit and with calculatioₙ ᴊ.

decays approximately as r^{-1} as would be expected from a point source in an infinite medium: however, the decay constant is a function of panel areal density, since that parameter affects pressure relief. Beyond r - 10 cm, pressure and impulse decay as $r^{-1/2}$ (as they do from a cylindrical source in aɴ infinite medium). The transition in decay rates was justified from observatioɴs of the pressure field in the water as a function of time. We inferred that beyond ᴜ10 cm the initial shock wave was no longer responsible for peak pressure.

Part II of this report contains a thorough comparison of the model defined in Equations 10 - 18 with numerical data from eight different runs. The model adequately described tне results of the individual calculations. Fit to experimental dat⍺ wᴀs also improved, as illustrated in Figure 4.6. Small discrᴇpancies can be explained by the fact that the numerical data are computed for z = 6 cm (at tне position of the trans-ducer), but the analytic model is formulated for ⍰ = 1 mm.

Since panels respond as if loaded impulsively, impulse is the most critical parameter for judging numerical models. Predicted and observed impulses are compared in Figures 4.7 and 4.8. Again, the notation of Table XIII applies. Equation 12 is graphed as a solid line, and the dashed line shows the approximate corrections for translation to $z = 6$ mm. For both thick and thin panels, the model impulses were about one half the measured ones at $r = 7.5$ and 10 cm. At 20 cm the model overpredicted impulse by a factor of about two. The scaling relationships implied by Equation 12 were used to prepare these figures. The linear velocity scaling of Equation 12 worked slightly better than the quadratic velocity scaling of Equation 9. The scaling for projectile size (in Figure 4.7) was rather good. However, the areal density scaling in Figure 4.8 was still inaccurate.

The numerical results reveal much of the structure of the pressure field behind the impacted panels. The effect of panel thickness on pressure is particularly interesting. Both the calculations and the experiments show that thick panels give rise to multipeaked pressure pulses. As explained in Part II of this report, the calculations show how later pulses are caused by the coupling of pressure waves in the water with stress waves in the plate. Energy in the water seems to couple to a wave in the panel and essentially "tunnels" through the aluminum to reappear ahead of what was initially the wavefront in the water. This leads to a region around $r = 10$ cm in which impulse becomes nearly independent of range. The anamolous-appearing experimental data in Figure 4.7, which shows larger impulses at $r = 10$ cm than at $r = 7.5$ cm, were probably caused by this effect.

The modelling of perforation in the finite element code is relatively crude. The aluminum is only three zones thick and peels away from the impact site. As a consequence, the numerical calculations probably underestimate the strength of the initial shock waves in the water. These waves were caused

69
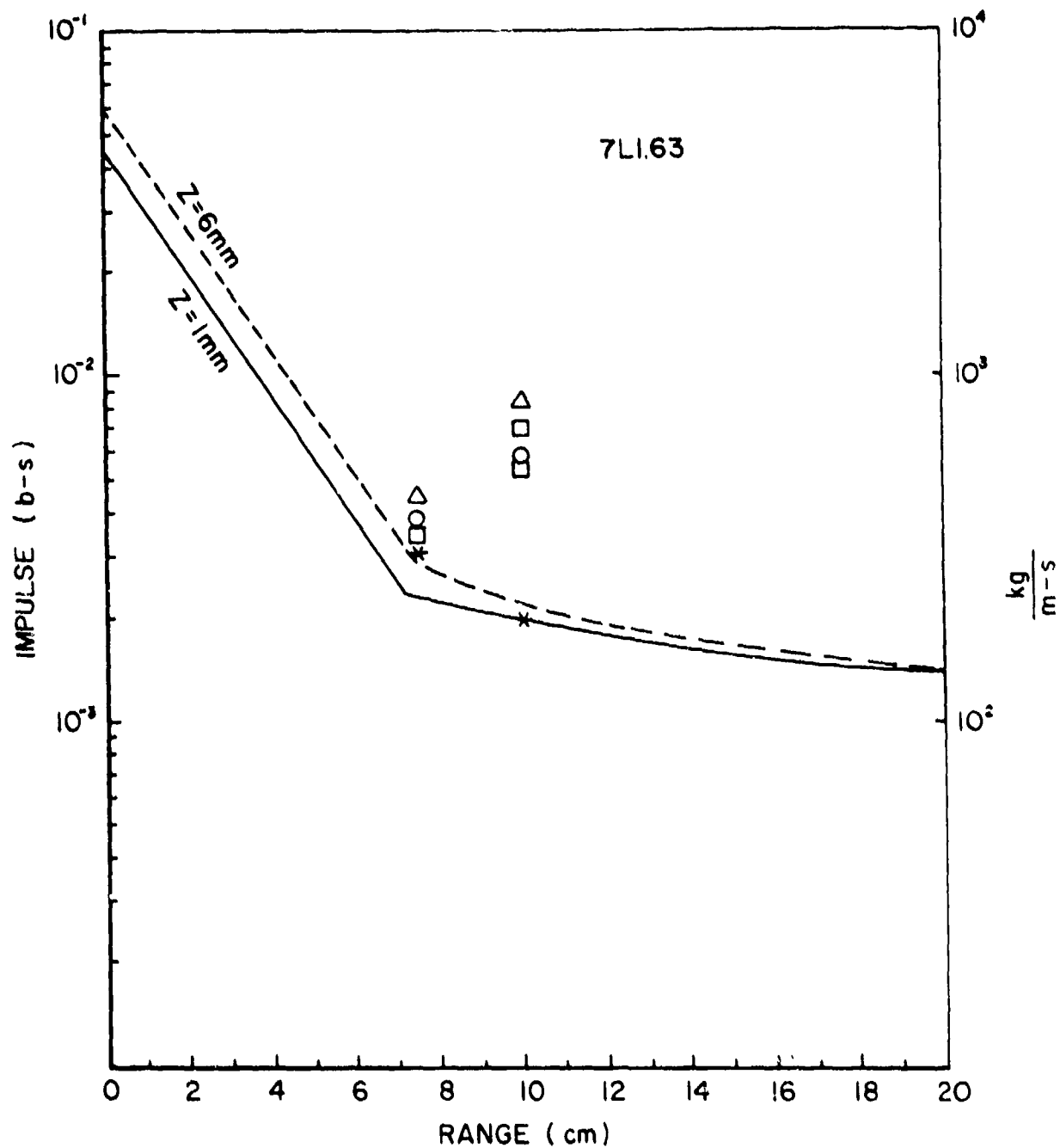
Figure 4.7. Model impulse (equation 12) compared with experimental data, normalized to 7L1.63 configuration (Symbols are explained in Table XII).

70
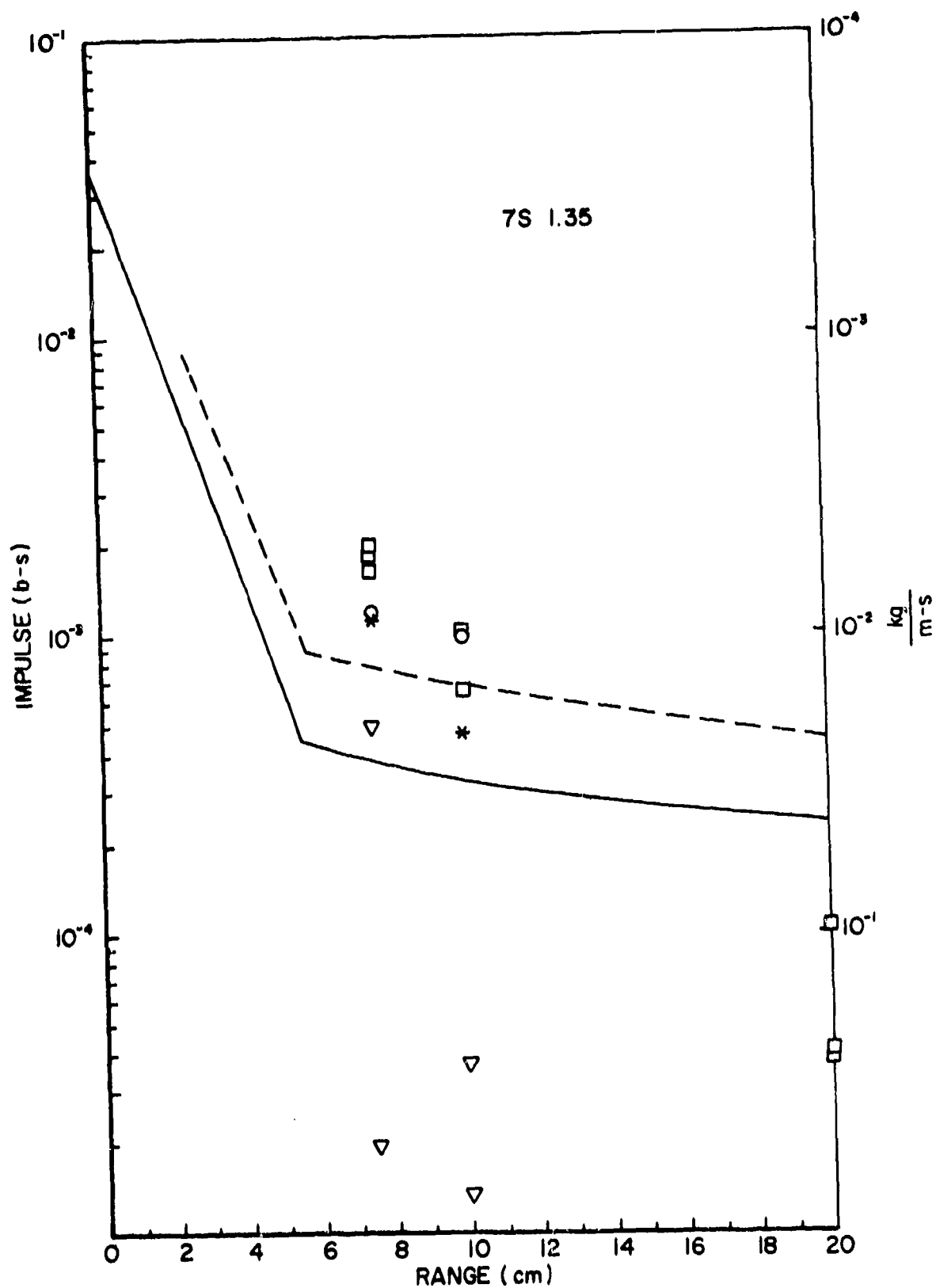
Figure 4.8. Model impulse (equation 12) compared with experimental data, normalized to 7S1.35 configuration.

by impact stresses in the aluminum; their duration was amplified by the formation of a broad shock front in the water by shear and spall failure of a "plug" of aluminum that was often wider than the projectile. The first experimental peak in Figure 4.6 is believed to be associated with this process.

The calculation for a foam-backed panel indicated that near the panel peak pressures were reduced by a factor two, near the impact site and were similar to a non-foam panel at greater ranges. This is consistent with the data in Table X. Details of the calculations are presented in Part II.

4.2 DISPLACEMENT

The NONSAP structural response code was driven with the loading function described in Equations 3 through 9.

The numerical results were compared with the experiments. This comparison was an excellent way to check the code, because displacement was the primary variable in the code. The numerical results, presented in Part II of this report, were not fully satisfactory.

The case examined was 7L1.63, which corresponds to Shot FD8. This was a valuable test case, since it was just below the failure threshold for 6.35-mm-thick 7075-T6 panels.

Figure 4.9 shows a comparison of the experimental and numerical results. The actual peak displacement was more than twice the predicted value. In addition, the calculated panel shapes were qualitatively wrong; the analysis predicted that an inflection would be present at 1.2 ms and a rebound at 1.6 ms. Neither was observed.

Two sources for the discrepancy were diagnosed. The first concerned neglect of the late-time effect of the water behind the panel. The typical duration of the loading function was only 75 μs. At later times, there was no forcing function input to the NONSAP code. In reality, a late-time pressure was exerted on the panel equal to $1/2 \, \rho \, (\dot{w} - u)^2$, where $\dot{w}$ is the panel velocity and u is the z-component of the water velocity.

72
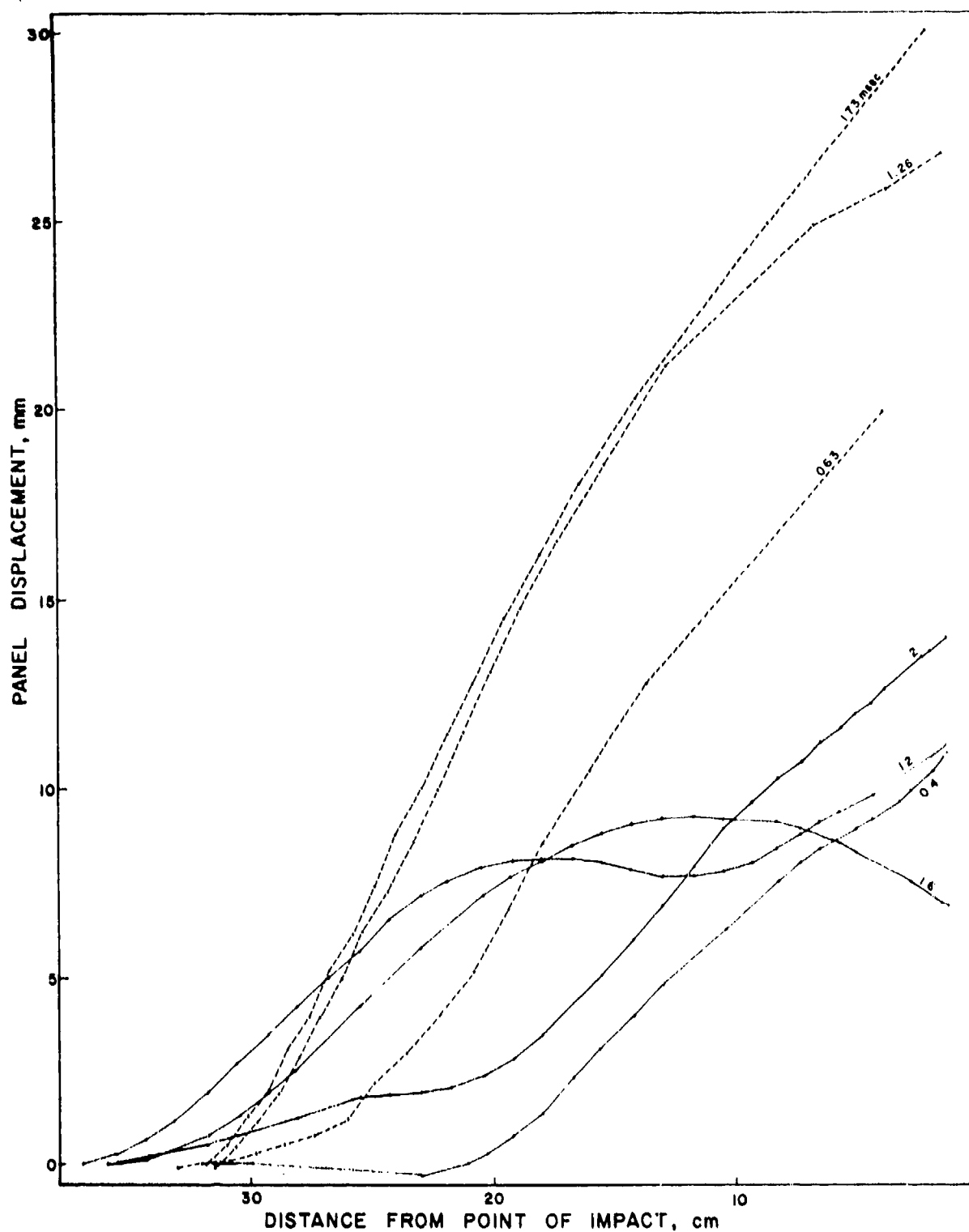
Figure 4.9. Comparison of measured (dashed lines) and predicted (solid lines) displacement for FD8 (configuration 7L). (The measured profiles are referred to the original surface, translated outward to maintain zero displacement at the bolt centerline).

73

In order to assess the importance of this effect, CRT reran the calculation with a late-time constant pressure equal to 5 bars; this was the approximate average value of $1/2 \rho u^2$ when the CRALE calculation was terminated. The resulting displacements were significantly closer to the measured ones.

Another possible error was the decay of the loading function with range for $r > 10$ cm. The original model contained an exponential decay. Limited results from the individual AFTON calculations indicated, however, that integrated impulse in the loading function was nearly independent of the range beyond $r = 10$ cm. To see if this effect contributed to the errors in calculated displacement, another NONSAP calculation was run in which the total impulse was kept constant for $r > 10$ cm.

Each of these two corrections accounted for about half the discrepancy, and the rebound and inflection points were eliminated. We, therefore, believe that the presence of these two effects is an accurate diagnosis of the problem. However, there are still some difficulties with the analytic approach to displacement, principally in the revised calculations prediction that the peak displacement would occur at 1.2 ms, which was much too soon.

Another possible cause of the discrepancy was the difference between the shapes of the actual and model panels. The panel in the numerical work was round with a 37.5 cm radius, but the experimental panel was square with 60 cm on a side. Two lines of reasoning indicate that panel shape had only a minor effect on displacement and that the effect was to increase the numerical value. The round-trip travel time for the deflection wave from the impact to the edge was 2 ms. This is less than or comparable to the time of peak deflection, so from this argument it seems that panel shape should have had little effect on calculated displacement. A similar conclusion can be reached by considering the panel displacement resulting from a constant load. Handbook formulas are available for deflection of

74

circular and square membranes subjected to uniform loads with fixed boundaries.[3] For a circle, the peak deflection is

$$Y_c = 0.171 \frac{Pr^4}{Et^3} \qquad (19)$$

whereas for a square

$$Y_s = 0.0138 \frac{Pa^4}{Et^3} \qquad (20)$$

In these formulas, E is Young's Modulus, P is the load, r is the radius, a is the side length, t is thickness, and Poisson's ratio is 0.3. For a circumscribed circle (2r = a), Y_c/Y_s = 0.773. For the case at hand (r = 37.5 cm, a = 63.5 cm), Y_c/Y_s = 1.50. Thus, for late times, a circular panel should experience a larger deflection than a square one. The numerical results were the opposite.

We believe that the most probable major cause for the displacement discrepancies was the way that the late-time loading of the panel was handled. A more accurate treatment could be based on piston theory[1] and would express the driving pressure as a function of the panel velocity. The piston theory approach becomes increasingly accurate as radial pressure gradients decline; this is the case at late times. Piston theory could not be used with NONSAP without extensive recoding. Boundary effects and uncertainties in the loading function beyond 10 cm from the impact also probably contributed to the discrepancy.

4.3 PREDICTION OF FAILURE VELOCITY

Originally it was planned to predict the failure velocity a priori for all combinations of panels and projectiles of interest. For this purpose the hoop stress in the panels were

examined by the NONSAP code. However, it became apparent that
the dependence of peak hoop stress on impact velocity was rela-
tively weak, and material failure criteria used in the code
were probably not precise enough to identify failure. The
approach taken was to "calibrate" the failure criterion by
providing CRT with the results of one test case. Accordingly,
the failure velocity for configuration 7L was provided.

A failure criterion was established based on the
integral $\int(\sigma_\Theta - Y)\,dr$, where Y is the yield strength. The
critical value was taken as that computed for the 7L configura-
tion at the failure threshold. Part II of this report described
in detail how, using this technique, a number of failure pre-
dictions were made. The failure predictions are summarized
in Table XIV, where they are also compared with the experimental
data.

Overall, the success of failure predictions was judged
poor. Although many failure points were not checked by
experiments because the values were extremely high or low, the
data do allow a few critical comparisons.

TABLE XIV.   SUMMARY OF FAILURE PREDICTIONS

Designation	V_F Predicted	V_F Measured
7L	--------	1.65 ± .02
7S	1.92-1.97	>1.95
7L	1.33-1.41	<0.99
7S	1.48-1.58	0.99 ± .07
2L	1.60-1.64	>1.62
2L	1.45-1.46	<1.32
2S	1.60-1.64	1.77 ± .17*

*Determined for a spherical projectile.

For those cases in which a critical comparison is possible, viz 7S, 7L, and 2L, the predictions were significantly in error. We believe that a number of factors contributed to the inability of the analysis to predict failure:

- Peak stress in the panel was not resolved precisely enough in the impact region.
- Adequate triaxial tensile failure data for the panel materials were not used.
- Initial pressures were higher than predicted because of higher effective drag forces on the cubical projectiles and debris.
- Stress concentrations occurred at the corners of the perforation made by the cubical fragments. Especially in thin panels, this led to significantly lower failure thresholds than might otherwise have existed.

SECTION V
SUMMARY OF DATA FOR PANEL DESIGN

This section collects the results of experiments and calculations and formulates design guidelines. The design guides have regions of uncertainty, but we believe that they represent the best inferences that can be made from the presently available experimental and numberical data.

5.1 FAILURE CRITERIA

We analyzed failure of plain aluminum panels, since that was the easiest case, and we used the insight gained to treat graphite epoxy panels. Finally, we examined the data for foam-backed panels and stiffened panels.

5.1.1 Failure of Plain Panels

Failure criteria must be fixed by experimental data, since the calculations were not accurate enough to stand alone. For given panel, liquid, and projectile materials, the failure criteria must take the form

$$f\ (V_F, D, W) = \text{constant} \qquad (21)$$

The constant in Equation 21 was termed the failure constant and is denoted by F. The principal problem was to determine the form of the function F so that F could be evaluated and failure criteria could be extrapolated from the data. By assuming that the inaccuracies in the numerical failure predictions were caused mainly by inaccuracy in the failure constant, we used the numerical results to determine $\partial V_F/\partial D|_W$ and $\partial V_F/\partial W|_D$. This assumption could not be rigorously defended, but it could be partly justified by the following arguments: (1) The calculations reproduced the pressure in the water; thus, they probably correctly treated

78

the important physical phenomena that led to panel strain and failure. (2) The most likely cause of error was inadequate failure criteria for aluminum. In most models this would only affect the value of the constant in Equation 21 (see discussion below).

The data by themselves were complete enough to determine empirically the failure constant or the functional form of F. Therefore, we considered a small number of reasonable physical models for penetration that resulted in particular forms for F. We selected forms that did not contain any additional empirical parameters. The relative validity of these forms could be distinguished from the data by the degree to which F was indeed constant.

To derive phenomenological models, we assumed that the panels failed because of forces exerted at early times near the impact site. If a displacement δ occurred at the edge of the perforation and the displacement only extended for a distance r beyond the perforation, then the hoop strain would be approximately $2\delta^2/r^2$. To reveal the gross dependence of hoop strain, ε_θ, on impact variables, we used $\delta = \frac{1}{2} at^2$. The acceleration, a, was found from the force/unit mass on the panel, $\overline{P}t/\rho_t W$. Here ρ_t is panel density, and $\overline{P}$ is the average pressure exerted on the panel during time t. The width of the affected region of the panel was r = Ct, where C is the shock speed in water. Thus,

$$\varepsilon_\theta = \frac{P^2 t^2}{2\rho_t^2 C W^2} \tag{22}$$

The impulse delivered to the water during the penetration ($o \leq t \leq W/V$) was approximately

$$\int (P_H \frac{D}{W} + \rho V^2) dt = \frac{P_H D^2}{C_p W} + \rho W V \tag{23}$$

79

where P_H is the pressure resulting from a one-dimensional impact, ρ is the liquid density, and C_p is the speed of sound in the projectile. The shock was assumed to attenuate approximately as $1/r$ and to be of duration D/C_p; the duration of the penetration was W/V. P_H could be related to V by an impedance-match solution[4], the results of which are shown in Figure 5.1. Over the range of interest, the pressure in the water was almost a linear function of impact velocity given by

$$P_H = A_H V \tag{24}$$

$$A_H = 68 \ \frac{kbar}{km/s} \tag{25}$$

When the right-hand side of Equation 23 was evaluated for thin panels, the first term was found to be about three times the second; for thick panels, the first was about 30 times the second. Thus, for early times, the shock pressure dominates the drag pressure. Substituting Equation 23 for Pt in Equation 22 and ignoring the drag term gave

$$\varepsilon_\theta = \frac{A^2 V^2 D^2}{2\rho^2 C^2 C_p^2 W^2} \tag{26}$$

If failure was associated with a maximum value of ε_θ, then the form of Equation 26 would become

MODEL I $\qquad\qquad\qquad F_1 = \frac{VD}{W} = \text{constant} \qquad (27)$

As expressed in the form of Equation 27 and throughout this report, large values of the failure constant are associated with materials that are relatively resistant to failure.
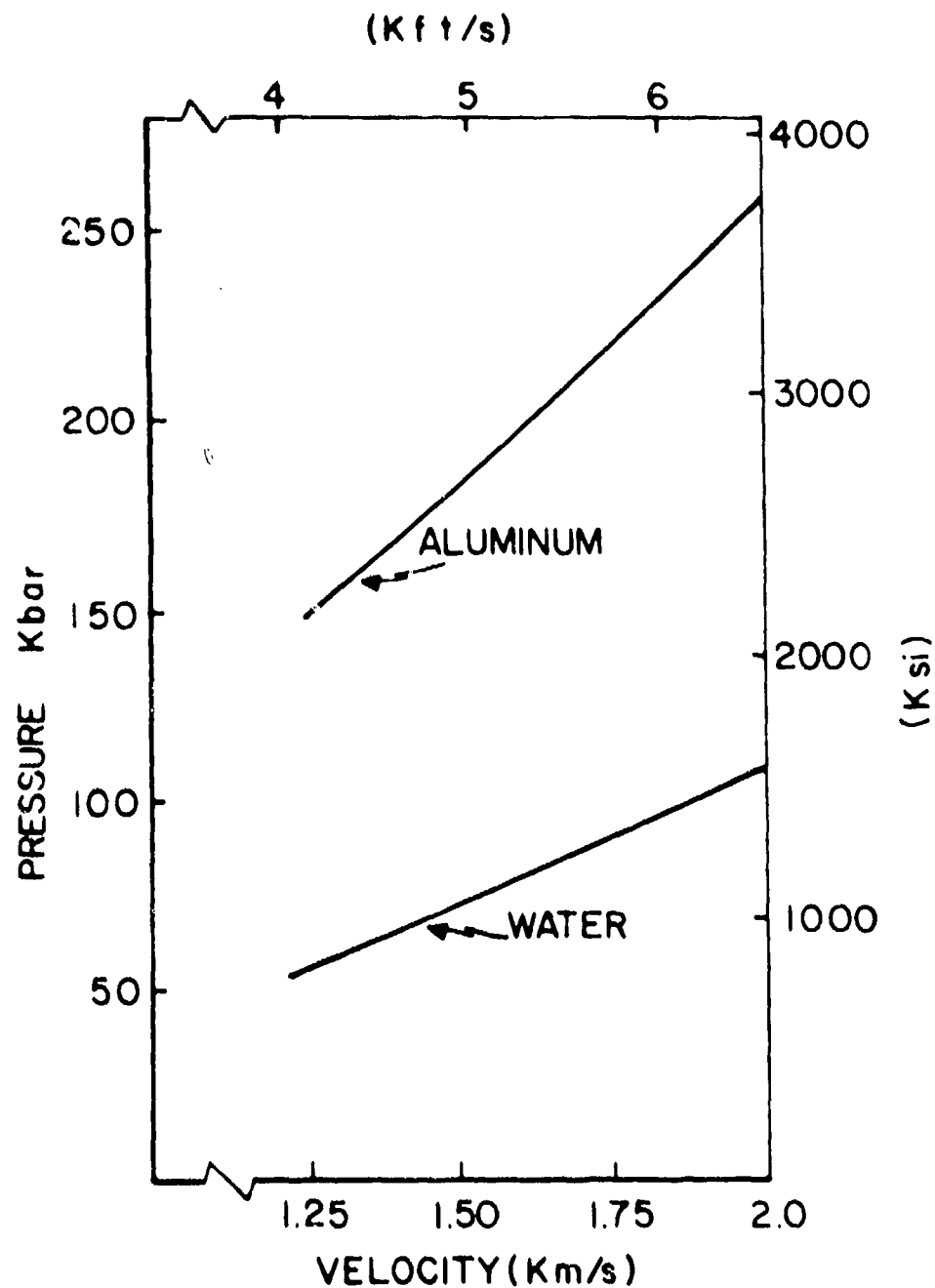
Figure 5.1. Theoretical one-dimensional impact pressure for impact of a steel projectile on a water-backed aluminum plate.

81

A simpler model resulted from assuming that failure is proportional to the impact energy, $\frac{1}{2} \rho_p D^3 V^2$, divided by the panel volume, $L_p^2 W$ (where L_p is the panel edge dimension). This model led to the failure criterion

MODEL II
$$F_2 = \frac{V^2 D^3}{W} = \text{constant} \tag{28}$$

Note the higher powers of V and D than in Equation (27).

Model III was based on prompt shock energy. The energy per unit volume in a shock wave is $\int Pu \, dt$. At any given position in our tank, this value was proportional to $P_H u_H t_s$, where u_H is the particle velocity associated with the initial shock pressure and t_s is the shock duration. If we substitute the Rankine-Hugoniot relationship,[5]

$$u_H = \frac{P_H}{\rho_o C_o} \tag{29}$$

and $t = D/C_p$ gave

$$P_H U_H t = \frac{P_H^2 D}{\rho_o C_o C_p} \tag{30}$$

Failure would be caused by this energy being imparted to a wall section of thickness W; this observation led to the failure criterion

MODEL III
$$F_3 = \frac{V^2 D}{W} = \text{constant} \tag{31}$$

We could have formulated other models involving more adjustable constants and corresponding to a more sophisticated view of the failure process. However, the data base

82

was insufficient to provide a value for more than one empirical failure parameter. The analysis for selecting among models I, II, and III is presented in Table XV.

In order to evaluate the models, it was necessary to construct the largest possible data set. Although some numerical failure predictions were inaccurate, we assumed that the errors were systematic (such as would result from an erroneous failure criterion for aluminum). In that case, numerical results could still be compared with each other in order to determine the dependence of failure on parameters which were treated correctly. We made the following sets of comparisons of the entries in Table XV: 1-2, 1-4, 3-4, 6-7, 8-11, 10-12. The entry on line 10 was not used because the failure velocity was anamolous with respect to the other calculations. Of the six comparisons, average (absolute) values of percentage differences in the failure constant for models were as follows:

Model I: 23%
Model II: 37%
Model III: 10%

Model III was clearly the best. Moreover, since it contained V to the second power, the expected error in V_F (all else being equal), is only about 5 percent. Model I was almost as good as Model III, if one ignored the comparison between the experiments in 1-3. However, this is a crucial comparison because it involves a large contrast in V.

Design curves for prevention of failure in plain panels are given in Figures 5.2-5.6. Model III was used in these figures, and the failure constant was evaluated separately for each curve for which there was an experimental data point. For curves that did not go through data points, average values of the failure constant were used. Table XVI summarizes the recommended values for the failure constant. Note that the

TABLE XV

EVALUATION OF FAILURE CRITERIA
(units used are mm and μs)

| Line | Configuration | | | V_F | Source | Values of Failure Constant | | |
	ID	D	W			Model I (VD/W)	Model II (V^2D^3/W)	Model III (V^2D/W)
1	7L	11.41	6.35	1.65	experiments	2.96	637	4.89
2	7S	8.97	6.35	1.95	numerical	2.75	432	5.37
3	7L	11.41	1.6	1.33	numerical*	9.48	1642	12.6
4	7S	8.97	1.6	0.99	experiment	5.55	442	5.5
5	7S	8.97	1.6	1.53	numerical*	8.58	1055	13.1
6	GS	11.08	4.8	1.47	experiment	3.39	612	4.99
7	GS	11.08	3.18	1.09	experiment	3.79	508	4.14
8	2L	14.25	6.35	1.65	numerical*	3.7	1241	6.11
9	2S	11.08	1.6	2.08	experiment	14.4	3678	30.0
10	2S	11.08	1.6	1.62	numerical*	11.22	2231	18.2
11	2S	11.08	6.35	1.96	numerical*	3.42	840	6.70
12	2L	14.25	1.6	1.46	numerical*	13.0	3855	19.0

*May be in error by 50 percent.

84

Figure 5.2. Design summary for bare 7075-T6 aluminum panels struck by single cubical fragments. Failure velocity versus panel thickness for various mass fragments, based on $v^2 D/W = 5.19$ km^2/s^2.
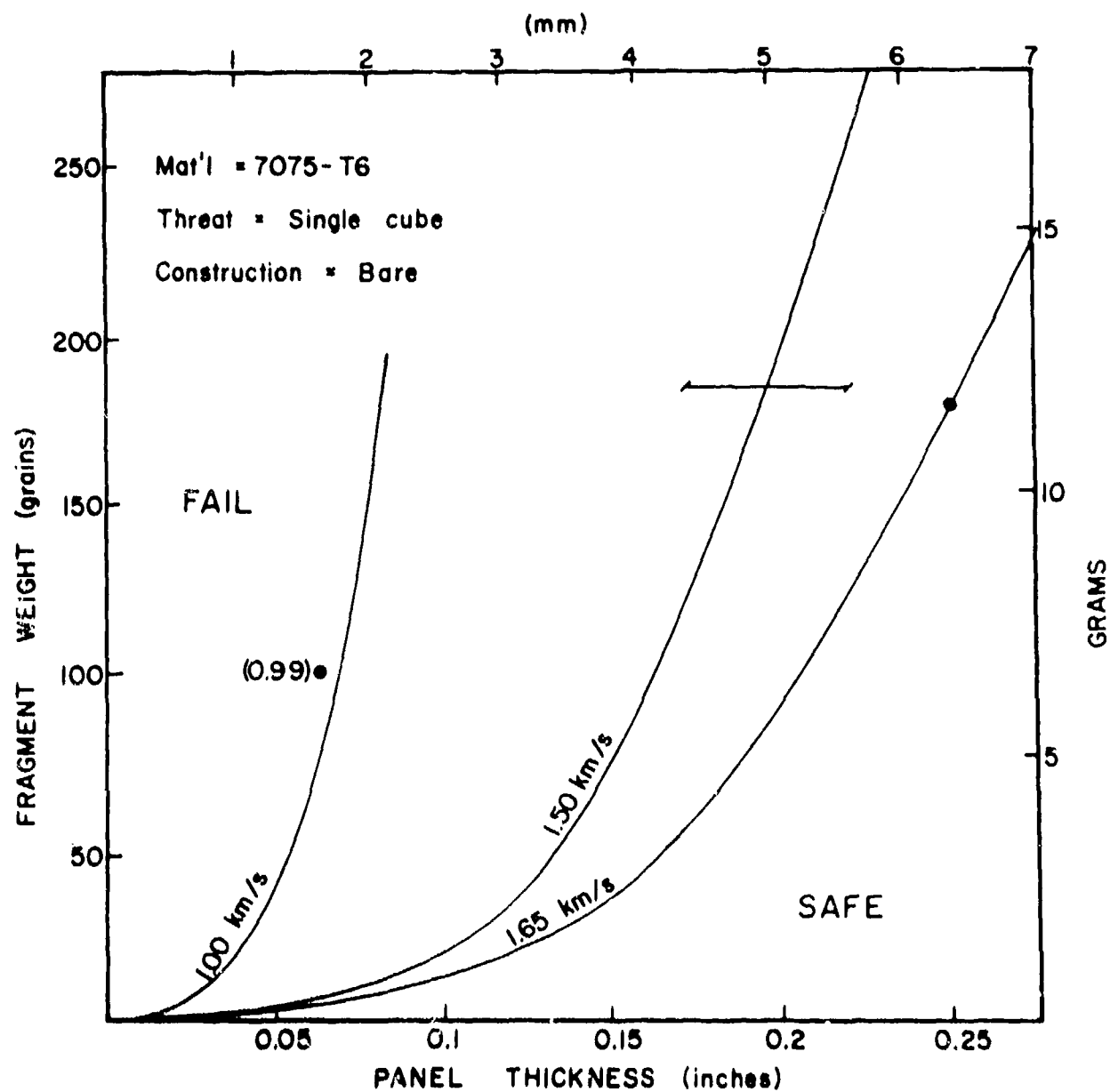
Figure 5.3. Design summary for bare 7075-T6 aluminum panels struck by single cubical fragments. Fragment mass versus panel thickness for various velocities, based on $v^2 D/W = 5.19$ km^2/s^2.
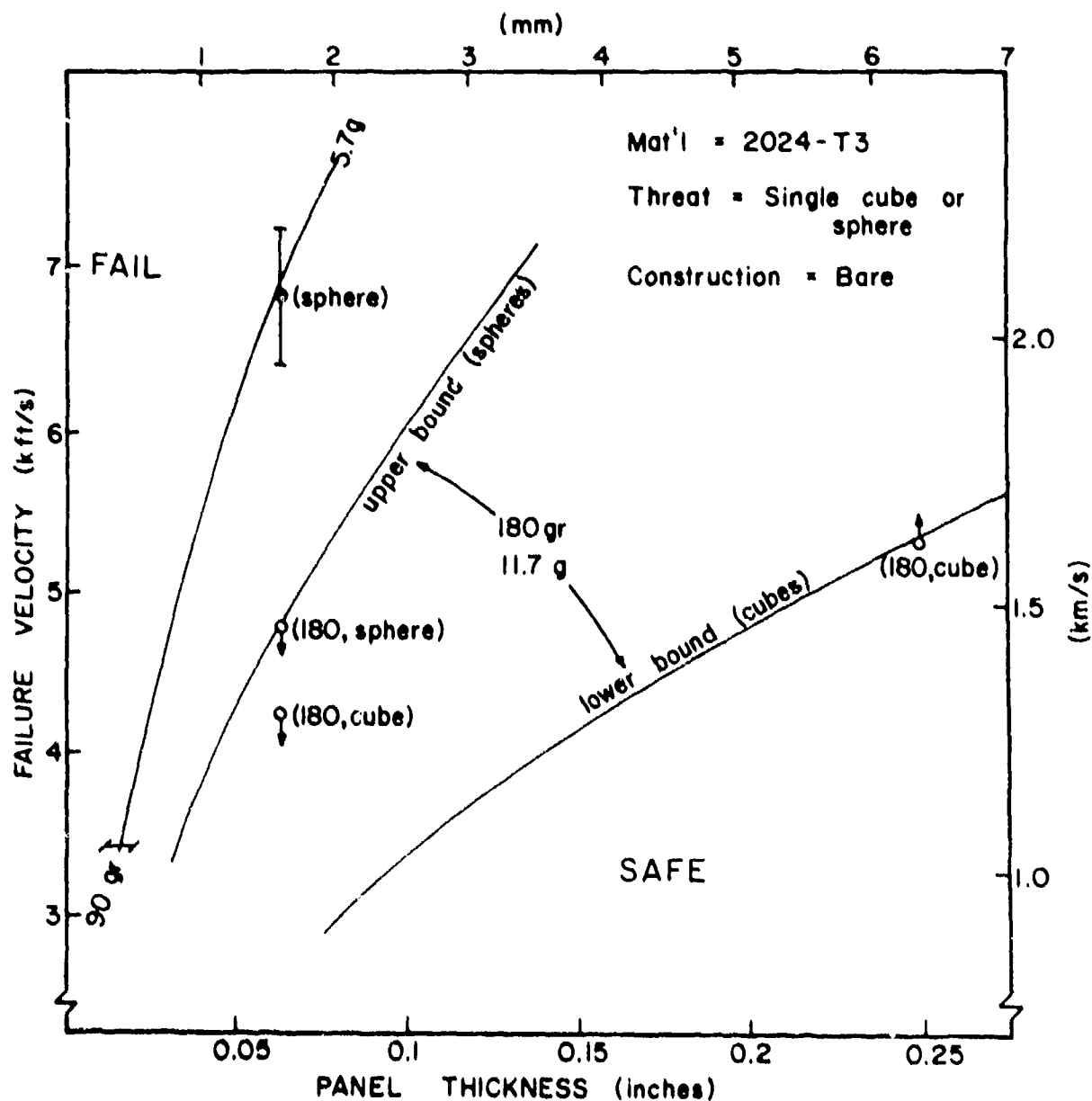
Figure 5.4. Design summary for bare 2024-T3 aluminum panels struck by single cubical fragments. Failure velocity versus panel thickness for various mass fragments, based on $v^2 D/W = 30$ km^2/s^2 for 90 g cubes, 19 km^2/s^2 for 180 g spheres, and 12 km^2/s^2 for 180 g cubes.
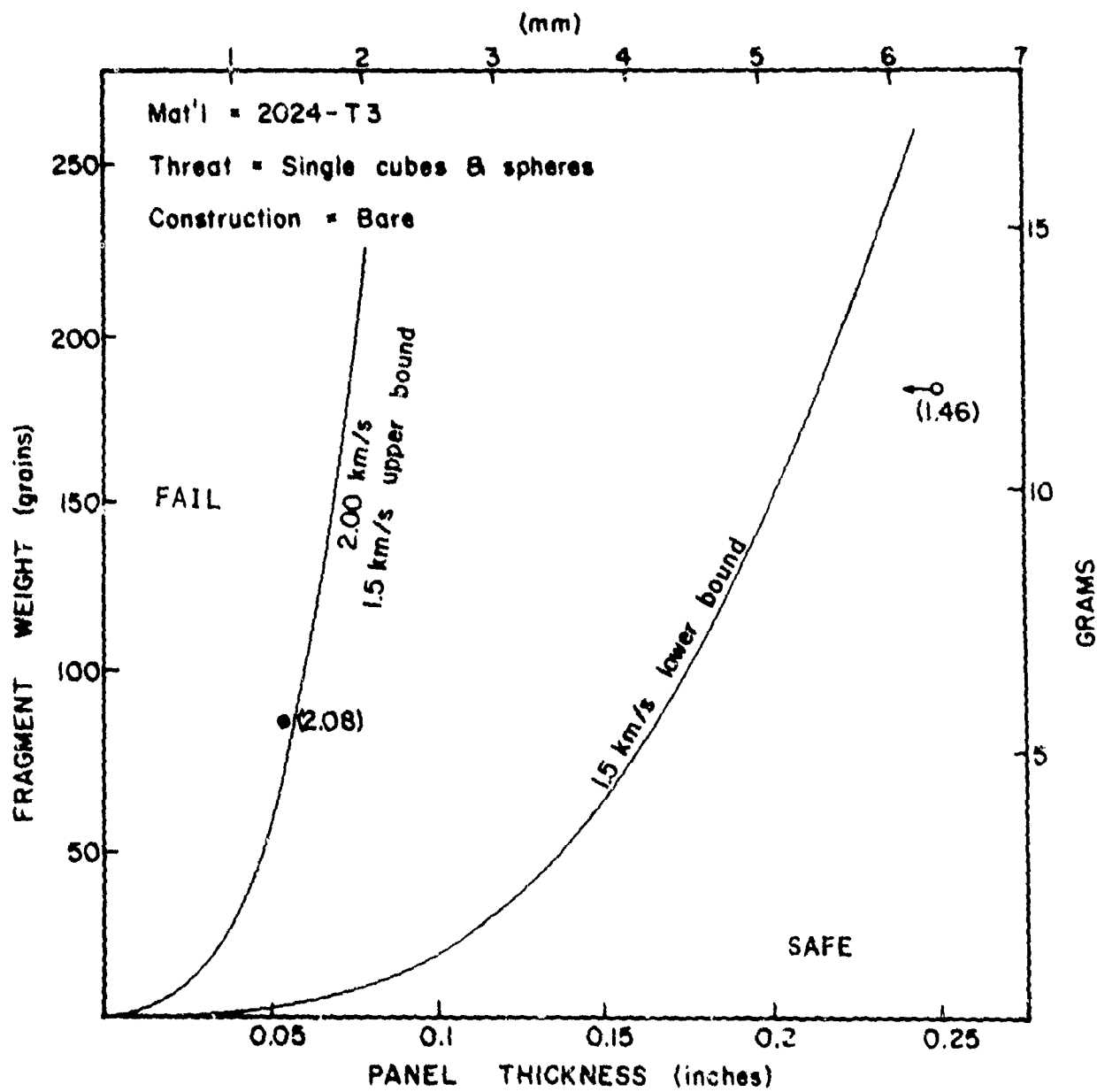
Figure 5.5.   Design summary for bare 2024-T3 aluminum panels struck by single cubical fragments. Fragment mass versus panel thickness for various velocities, based on $v^2 D/W = 30$ km^2/s^2 for 90 g projectiles and 19.0 km^2/s^2 for 180 g projectiles.
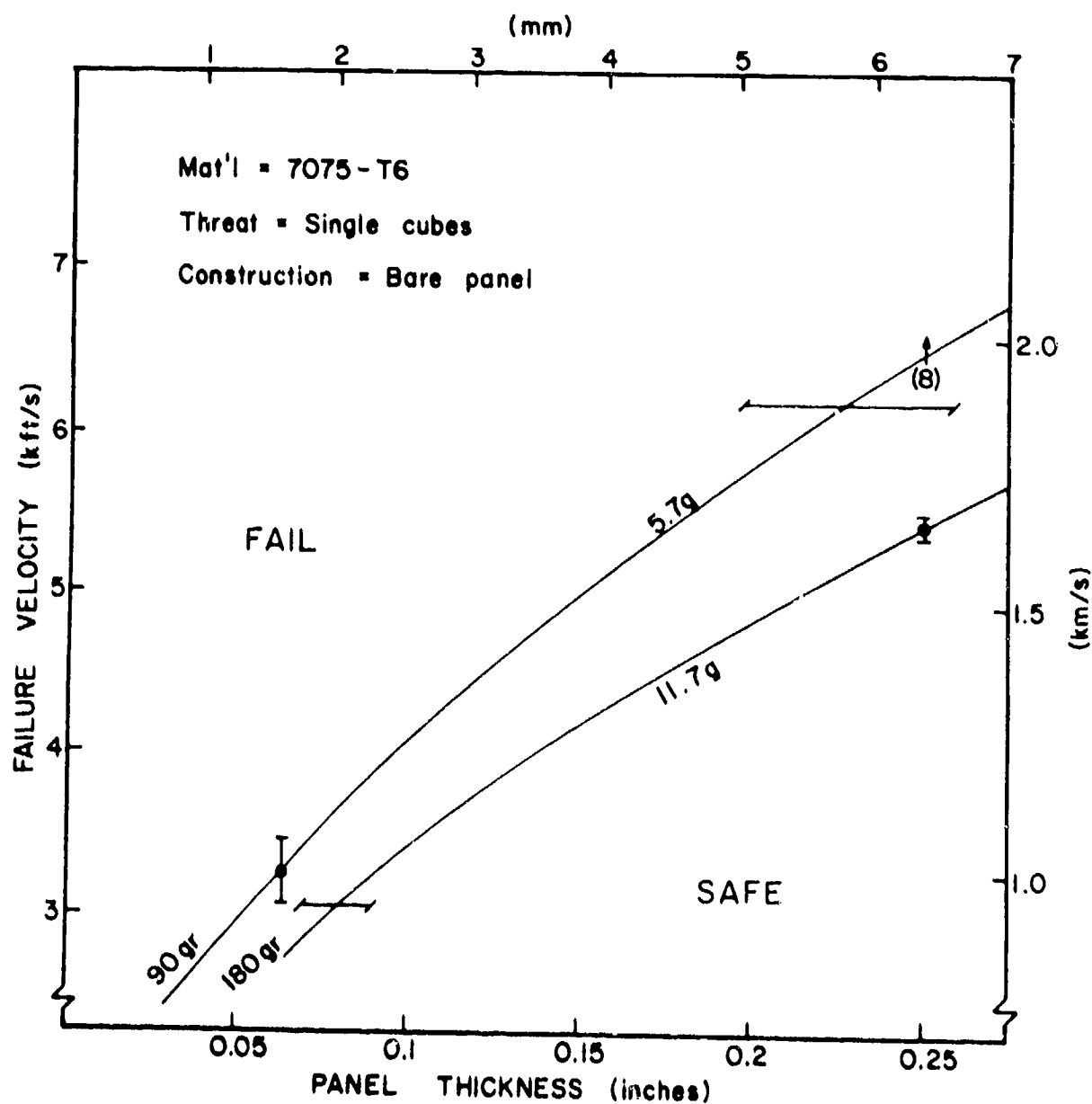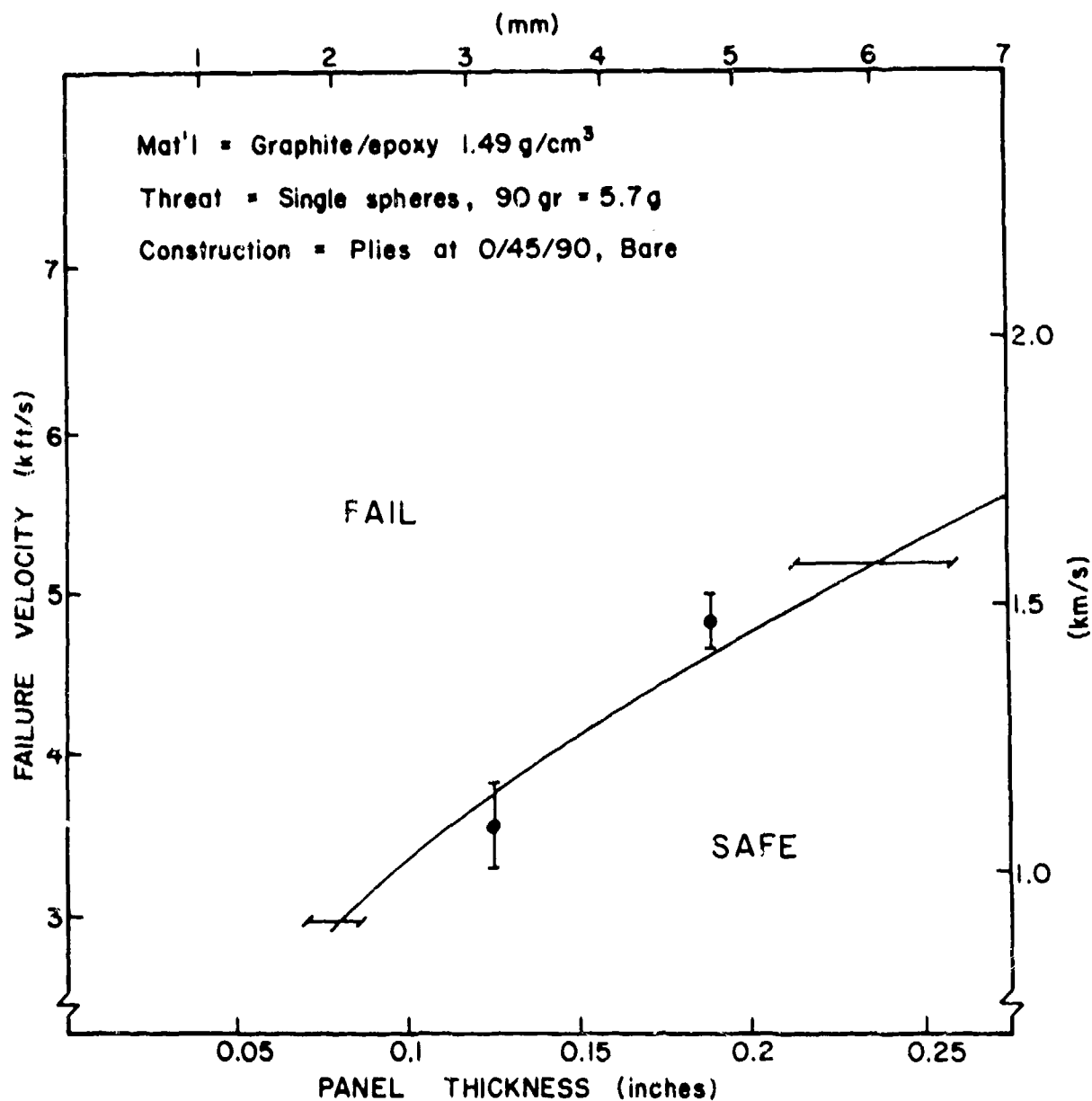
Figure 5.6. Design summary for graphite epoxy panels struck
by single cubical fragments. Failure velocity
versus panel thickness for 5.7 g fragments, based
on $v^2D/W = 4.53$ km^2/s^2.

parameter D in this table represents cube edge or sphere diameter.[*] Experimental data points for failure velocity are shown as filled circles with error brackets; open circles with an arrow are used where the failure threshold was only bounded on one side. Numerical results of relatively high confidence are shown as open circles with parenthesis. Uncertainty ranges are indicated on the curves when appropriate. Uncertainty along any curve grades from the uncertainty in data points to the uncertainty range indicated for the curve.

TABLE XVI
RECOMMENDED VALUES OF FAILURE CONSTANT

$$\frac{V^2 D}{W} = F_2$$

Material	F_2 (km/s)^2
7075-T6 aluminum	5.19 ± 0.3
2024-T3 aluminum	30.0 + 5.7 (for 90-grain fragments)
	19.0 (for 180-grain fragments)
graphite epoxy (1.49 g/cm)^3	4.52 ± 0.47

Figures 5.4 and 5.5 for 2024-T3 aluminum presented some special difficulties. First, the available data were for both cubical and spherical projectiles. Second, the value of the failure constant from line 9 of Table XV, 30 mm^2/µs, leads to a failure velocity prediction for 2L (spherical pro- jectile of 1.83 ± 0.17 km/s, (shot FTA9, Reference 2). The source of this discrepancy may be that certain assumptions embodied in Model 3 are not valid when configurations 2S and 2L are compared; for example, the failure may have been slower

---

[*]The rationale for this is that in models I and III, D repre- sents the distance waves must travel in the projectile to encounter free surfaces and generate relief waves.

than predicted because the 2024-T3 alloy was relatively more ductile than the 7075-T6 alloy. Longer time scales imply that drag forces were relatively more important, hence, that failure was more dependent on a higher power of D, as in Model 2. We also noted that the failure constants for both 2S numerical and 2s experimental (lines 9 and 10 of table XV) were significantly higher than those for $\underline{2L}$, 2L, and $\underline{2S}$. To model failure for the 2024-T3 aluminum struck by the large projectiles, we used the failure constant from line 12 as an upper bound ($19.0 \text{ mm}^2/\mu s^2$). We believe this lower bound to be very conservative because it practically coincides with the failure criterion for 7075-T6 panels struck by 180-grain fragments. Cubical fragments are evidently more lethal than spherical fragments; we took this factor into account in Figure 5.4 by using cubical fragment data for the lower bound and spherical fragment data for the upper bound. In Figure 5.5, because of the large differences in failure constants, the upper bound for the 1.5 km/s curve fell above the 2.0 km/s curve; as this is physically unreasonable, the two curves were drawn coincident.

5.1.2 Failure of Graphite Epoxy Panels

Model II fitted the limited data for graphite epoxy panels very well. The results are shown in Figure 5.6. The data set provided a good test for the model because failure thresholds were determined for two different panel thicknesses struck by the same projectile.

5.1.3 Failure of Foam-Backed Panels

Foam was extremely effective for preventing gross panel failure. In fact, in all of the configurations that the University has examined to date, failure has been experimentally produced in only one foam-backed case--7LF. Numerical predictions of failures in foam-backed panels have also been unsuccessful.

The experimental and numerical results presented in Section 3 and Part II of this report showed that failure did not initiate immediately after impact in foam-backed panels. Therefore, the initial shock wave was not the failure mechanism in foam panels. Model III was not appropriate for this situation.

Rather, we examined the total impulse delivered to the panel.

The numerical calculations showed that the total impulse at a given range, r, is proportional to $Ve^{-\alpha r/D}$. When one intergrates from the impact site out to large r,

$$\frac{\text{total impulse on plate}}{\text{plate thickness}} \sim \frac{VD}{\alpha W} \tag{32}$$

From the numerical work,

$$\alpha = 0.185 + .35 \exp(-.03\rho_e W_e) \tag{33}$$

where W_e and ρ_e are the equivalent wall (panel plus foam) density and thickness. The exponential is mainly determined by the foam properties, not the panel properties, so this term was regarded as constant. Then the term α could be included in the constant F_1, and Equation 32 became

$$F_1 = 11.55 \text{ km/s}. \tag{34}$$

This value was used to construct the graphs shown in Figures 5.7 and 5.8. The model predictions are consistent with the data. A "best guess" uncertainty range of ±15 percent was assumed for F_1. Comparison of Figure 5.7 with Figure 5.2 illustrates that the presence of foam more than doubles the failure velocity.

Failure of foam-backed 2024-T3 panels required higher impact velocities than could be experimentally achieved. A reasonable extrapolation of Equation 34 would be to multiply F_1 by 1.35, since the strain-energy to failure of 2024-T3 aluminum is 35 percent higher than that of 7075-T6. However, this process yielded a prediction of V_F for the 2SF configuration of 1.67 km/s, whereas the observed value is $V_F > 2.38$ km/s. At this time, we do not feel that it would be useful to predict failure thresholds for foam-backed 2024-T3 alloy. The best we can do is to restate the observed lower limits for failure:
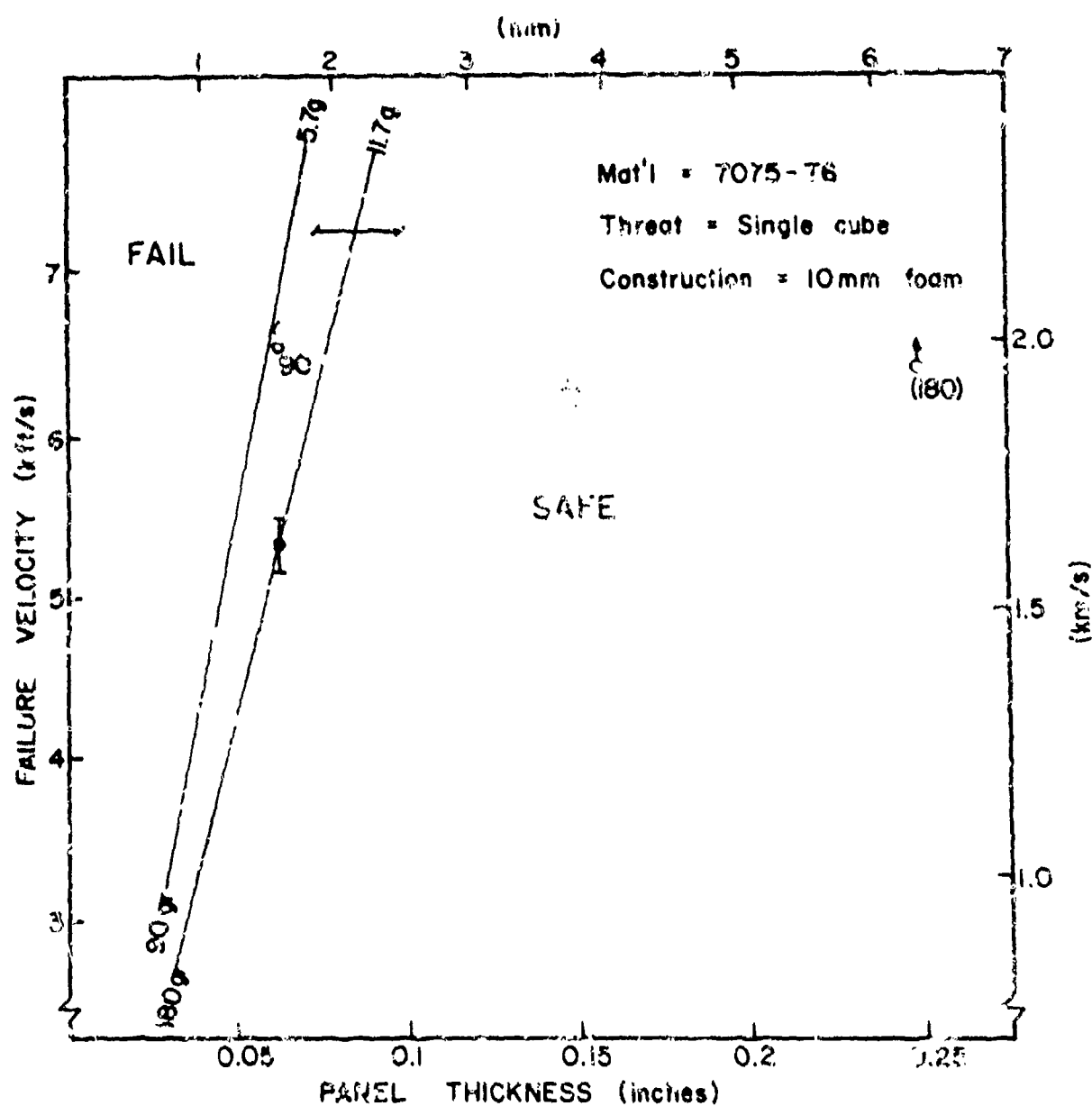
92

Figure 5.7. Design summary for 7075-T6 foam-backed panels struck by single cubical fragments. Failure velocity versus panel thickness for various mass fragments, based on VD/W = 11.55 km/s.
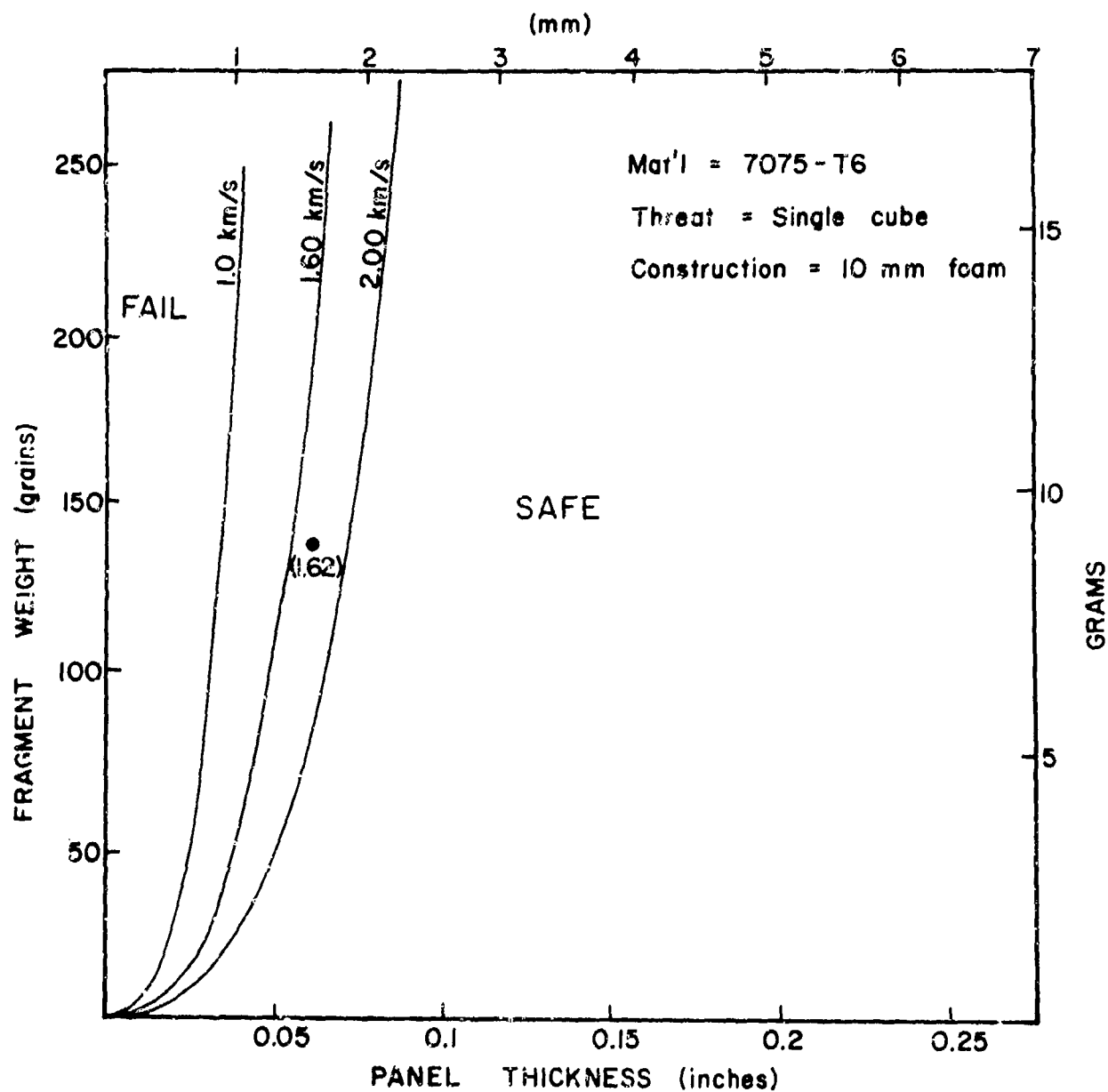
Figure 5.8. Design summary for foam-backed 7075-T6 panels struck by cubical projectiles. Fragment mass versus panel thickness for various velocities, based on VD/W = 11.55 km/s.

94

$$2LF \qquad V_F > 1.69 \text{ km/s}$$

$$2SF \qquad V_F > 2.38 \text{ km/s}$$

The data in Figures 5.7 and 5.8 will also yield a conservative design for 2024-T3 panels.

5.1.4 Failure of 2024-T3 Panels Stiffened With 6063-T6 Hat Sections

Addition of stiffeners changed the failure modes of panels, as we discussed in Section III. Massive tears no longer occurred; cracks only ran a short distance to stiffener rivet holes, then stopped. Failure was associated with stiffener crushing and rivet failures. A distinct failure threshold existed, below which permanent stiffener deformation was negligible and no rivets failed, and above which serious plastic deformation of stiffeners occurred and many rivets failed.

The stiffeners used in the study were made from 6063-T6 aluminum, which has a handbook yield strength of 1.4 kbar 21 (ksi). The results described below are probably not applicable to stiffeners made from stronger alloys (2024-T3 has a yield strength of 3.2 kbar). The construction of the test panels is shown in Figures 2.3 and 2.4.

Only one value of panel thickness was included in the test matrix, so the W dependence of f in Equation 21 could not be determined. However, since the observed failure was stiffener crushing, the panel thickness may or may not be a critical parameter.

Two failure points were determined. Of Models I through III, Model III fits the data more than twice as well as the others. This only showed adequate scaling for velocity and projectile size. The effects of variations in panel thickness and stiffener geometry could not be determined from the data. For this reason, the design curve in Figure 5.9

95

Figure 5.9. Design data for 2024-T3 aluminum panels protected
with "hat" stiffeners, based on $V^2D/W = 9.83 \text{ km}^2/\text{s}^2$.

96

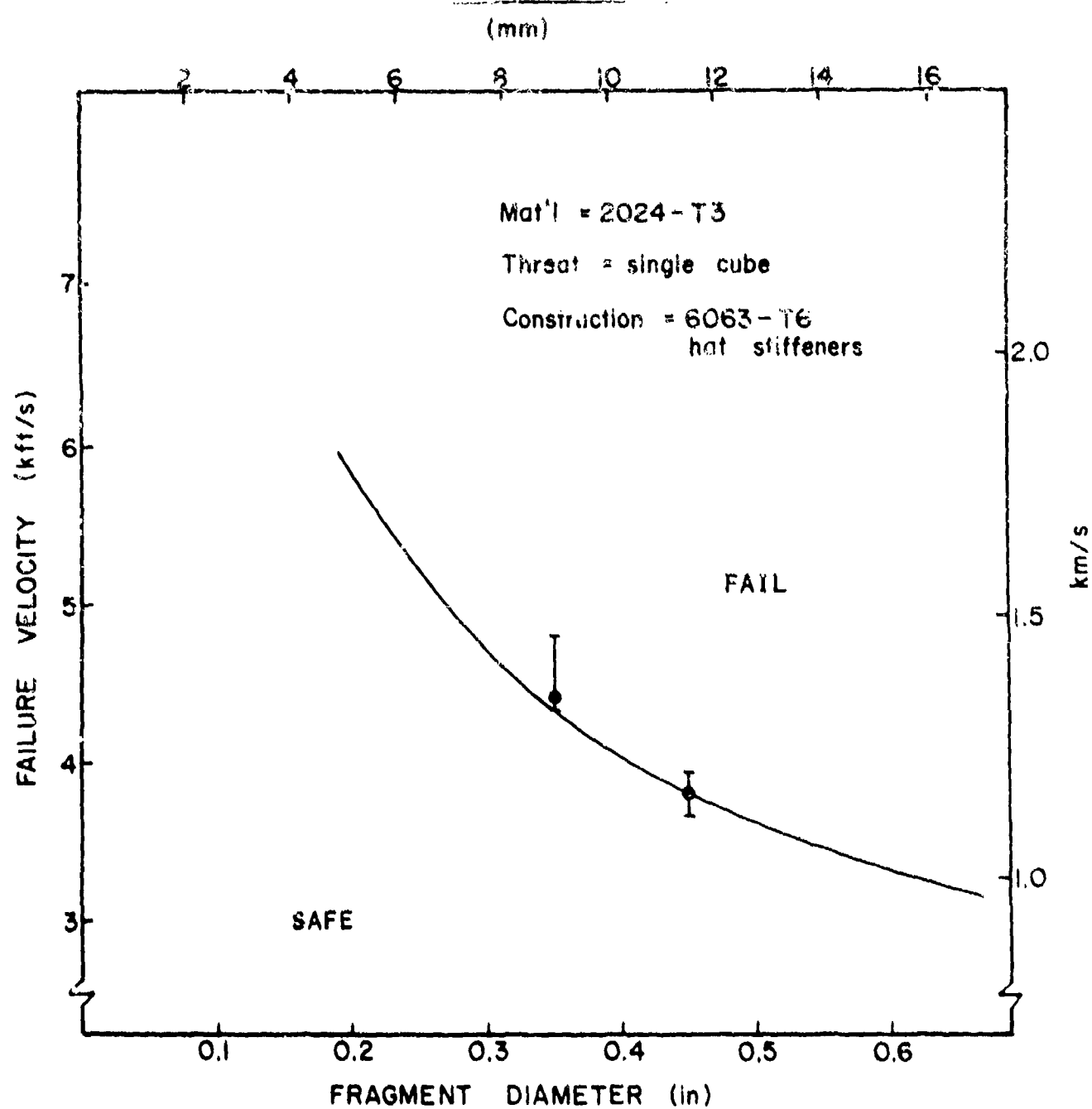is plotted as a fragment size versus fragment velocity. The average value of F_3 is 9.83 km^2/s^2.

The failure point for panels with foam between the stiffeners was not bracketed. From examination of the foam-backed panels that were shot, it appeared that foam between the stiffeners is not useful for protecting stiffeners from hydrodynamic ram damage. Increased protection could, however, be achieved by applying foam to the stiffeners themselves.

5.2 PANEL LOADING FUNCTIONS

The improved loading function developed by CRT is recommended for applications in which structural effects of hydrodynamic ram must be determined. The dependencies of impulse on projectile diameter, projectile velocity, and radial coordinate have been derived from a basically sound numerical analysis; and they fit the data as well as any reasonable model. Some discrepancies have been observed between pre-dicted impulses and experimental data; however, descrepancies have not been well enough determined to substantiate revisions of the model.

When we applied the model to a structural response code, we found it necessary to add a correction to the loading function to account for the resistance to inward panel motion caused by the water behind the panel. The size of the cor-rection and its dependence on impact parameters is yet to be determined. A late-time pressure of 5 bars was necessary to achieve reasonable correlation with observed displacements in a calculation of a 11.67-g projectile at 1.63 km/s. A physically reasonable assumption is that the velocity of the water is proportional to initial projectile impulse. This leads to scaling of the late time correction pressure for that case a factor $(M_p V/19)$. Here M_p is in grams, and V is in km/s. The resultant model is shown in Figure 5.10.

PRESSURE vs TIME graph with P_{max} peak at t_2, rising from t_1, then decaying curve labeled:

$$P = P_{max} e^{-\frac{t-t_2}{t_3}}$$

(axes: PRESSURE vertical, TIME horizontal, with t_1, t_2 marked)
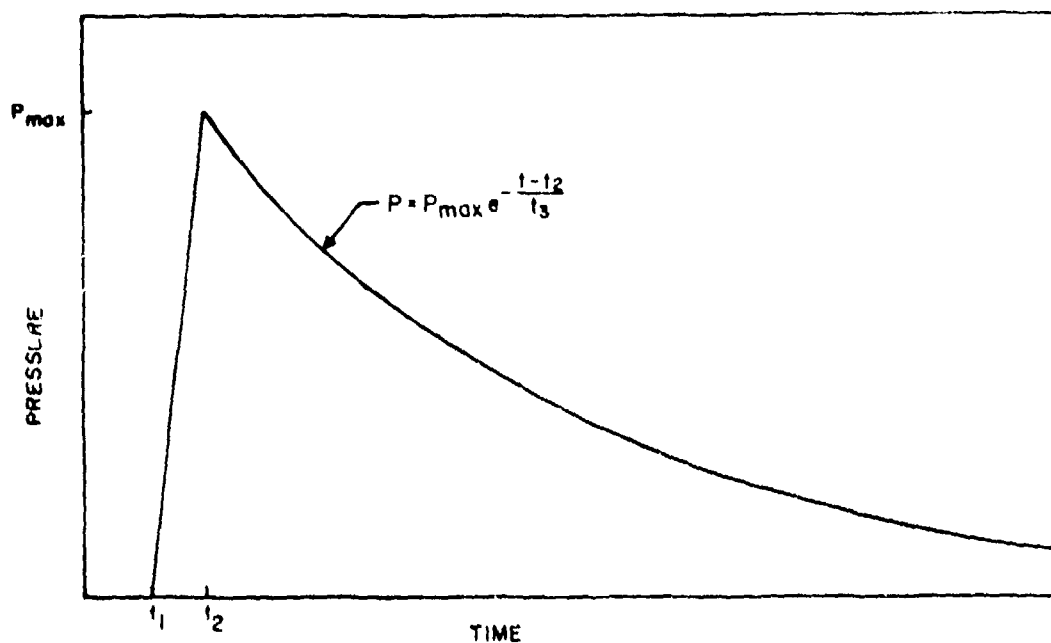
$$P_m = 3.68\delta V \left(R'/R_p\right)^{-\alpha}$$

$$\alpha = 1.15 + 0.6 \exp\left(-0.72 \rho_t W\right)$$

$$I = 0.03 \; \delta \; V \exp\left(-\beta R'/R_p\right)$$

$$\beta = 0.185 + 0.35 \exp\left(-0.63 \rho_t W\right)$$

$$t_2 = W/V + 6.25 \left(R - R_p\right)$$

$$t_1 = t_2 - \left(2W/0.63 + 1\right)$$

$$t_3 = \min \begin{cases} I/P_m - 0.5 \left(t_2 - t_1\right) \\ 10 \end{cases}$$

$$\delta = R'/r$$

$$R' = \begin{cases} r & r \leq 10 \\ 10 & r > 10 \end{cases}$$

Figure 5.10. Loading function model (symbols are defined in the Symbol Table at the beginning of this report).

5.3 DISPLACEMENT

Occasionally, the ease with which a solution is found
is commensurate with the solution's unimportance. Such is
the case of displacement, which for unfailed panels is probably
a relatively minor design parameter. Our data showed that
all unstiffened aluminum panels of 1.6-mm to 6.35-mm thickness
and of 10 cm x 10 cm linear dimension were displaced about
30 mm. Graphite epoxy panels of similar size were displaced
about 25 mm.

SECTION VI
SUMMARY AND CONCLUSIONS

For complex problems such as hydrodynamic ram, physical understanding is a great aid in the development of efficient optimum design techniques. Parts I and II of this report have continued the work begun in Reference 2, and taken together they present a generally adequate physical model for hydrodynamic ram damage induced by high-velocity fragments striking entrance panels. The experimental and numerical results from these programs have been used to compile design guidelines.

6.1 EXPERIMENTAL RESULTS

Failure data, displacement data, and pressure data have been obtained from laboratory experiments and finite difference calculations. Panels were made from 7075-T6 and 2024-T3 aluminum and from graphite epoxy; panel thicknesses were 1.6 to 6.35 mm. Protection included 10-mm-ballistic foam and stiffeners. Projectiles were 5.6-g and 11.7-g spheres and cubes.

Failures were always catastrophic, and failure thresholds were always abrupt. When cracks formed, they ran across the panels, except when stiffeners were present. In thin panels, cracks initiated at the corners of the perforation when cubical projectiles were used. The stiffeners used in this study sometimes failed by crushing.

6.2 PHYSICAL MODEL

Entrance panel damage caused by high-velocity fragments was primarily induced by the shock wave generated by the impact. The very high shock pressure resulted in impulsive loading of the panels. Cracks occurred at the entrance site almost immediately, and these were propagated by the displacement field. The dependence of failure on impact parameters could be approximately represented as

$$\frac{V^2 D}{W} = \text{constant}$$

where V is projectile velocity, D is projectile diameter, and W is panel thickness.

Stiffeners that suppressed displacement also suppressed crack growth. The effect of foam was to decouple the initial impact shock from the fluid and to lenghten the time over which the panel experienced impulsive loading; consequently, the peak stress at the entrance site was greatly reduced. Crack initiation was not as prompt in foam panels as in plain panels.

6.3 NUMERICAL RESULTS

The CRALE finite difference program was able to calculate pressure caused by shock and drag forces on the projectile. A simplified loading model based on the details of the CRALE results was developed. The results of driving the NONSAP structural response code with the simplified loading model, however, were disappointing. Neither displacement nor failure thresholds were correctly predicted. The error in displacement may be attributed to neglect of late-time water resistance to panel slow down and rebound.

6.4 DESIGN DATA

Design data were generated for all configurations studied. Design data included failure criteria and pressure loading functions. The failure data were based on experimental results, but numerical results were used to aid interpolation and extrapolation. The pressure loading functions were based on an analytic fit to the numerical results. Failure of stiffened panels was defined by stiffener crushing.

6.5 NEED FOR ADDITIONAL WORK

The aspect of phenomenology that is most seriously in question is the nature of the loading functions for foam-backed

panels. This subject should receive additional experimental and theoretical study.

Additional experimentally derived design data points should be obtained for the 7075-T6 and 2027-T3 panels examined here. Special attention should be directed to intermediate panel thicknesses and projectile sizes. Panels with stronger stiffeners than those used here should be tested.

The Finite element representation of hydrodynamic ram structural effects needs improvement. Effects of tear resistant bladders, impact obliquity, and projectile density should be examined.

Actual fuel tanks are likely to be struck by more than one fragment. Therefore, the single fragment work reported here should be quantitatively related to multiple-fragment effects.

APPENDIX A

EXPERIMENTAL DETAILS

A.1 BALLISTIC RANGE

The projectiles were launched with a 2-m-long, 20-mm-diameter launch tube. The powder was loaded into 12-gauge primed shot gun cases that were percussively detonated with a solenoid actuator. The ratio of launch energy to powder was approximately 1.2 kJ/g. Hercules 2400 was used for most shots; below 1000 m/s launch velocity, more reproducible results were obtained with Unique powder.

The cubes used in these tests were machined from 1020 steel. The hardness was Rockwell B72. The spheres were annealed ball bearings [52100 chrome manganese steel at a micrchardness of 280 HV (100 g load)].

The projectiles were carried by glass-fiber reinforced Lexan® sabots. Figure A.1 illustrates a launch package. The projectiles failed at launch velocities between 1.95 km/s and 2.0 km/s. We believe the failure to have been caused by manufacturing defects. These sabots were injection molded, and inadaquate heating of the mold resulted in some moisture collection in the center of each quadrant. Unfortunately, the problem was not diagnosed in time to have another batch of sabots fabricated.

The reported projectile velocities were computed from distances traveled between two radiographs. The radiographs were separated by about 46 cm; the second station was 80 cm from the target panel. The accuracy of the velocity determinations was about 0.8 percent, or about 12 m/s, typically. The projectile experienced a slight deceleration between the second radiograph and the target. Using an estimated drag coefficient for blunt cylinders of 1.67[1], the slowdown was calculated to be 0.96 ± 0.01 percent. This correction was ignored in the data tabulations.

Environmental data were also recorded for each shot. These included water temperature, room temperature, and barometric pressure. These data have not been reported here because no correlation with experimental results was detected.
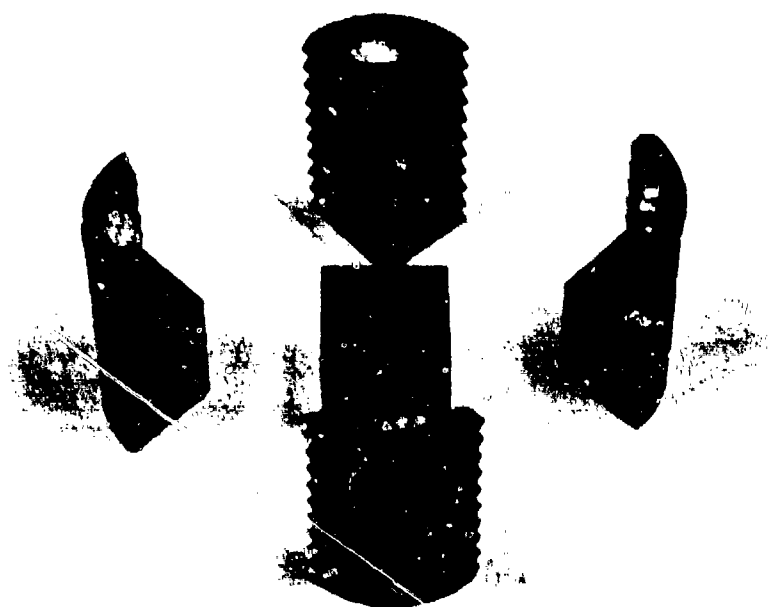
Figure A.1.   Four-piece sabot and cubical projectile.

A.2   MOIRÉ FRINGE DATA REDUCTION

The moiré optical apparatus consisted primarily of two
Ronchi rulings, commercially available lenses, a high-intensity
light source, and a high-speed framing camera. The apparatus
is shown schematically in Figure A.2. The mounting of the
optical elements was changed from that described previously[2]
to make the elements more rigid.

The light source was a "Press 50" flash lamp with an
intensity of more than 0.8 Mlm for at least 30 ms. This was
sufficient light for recording approximately 180 frames of
information at a framing rate of 6,000 f/s. The Ronchi
rulings were glass slides with evenly spaced, finely-ruled
lines separated by a distance equal to the line width. The
rulings had 78.7 lines per centimeter (200 lines per inch).
A Fastax high-speed framing camera was used to record the
moiré fringes.

There are two approaches to the analysis of data from the
moiré apparatus. The most direct way is to take a picture of
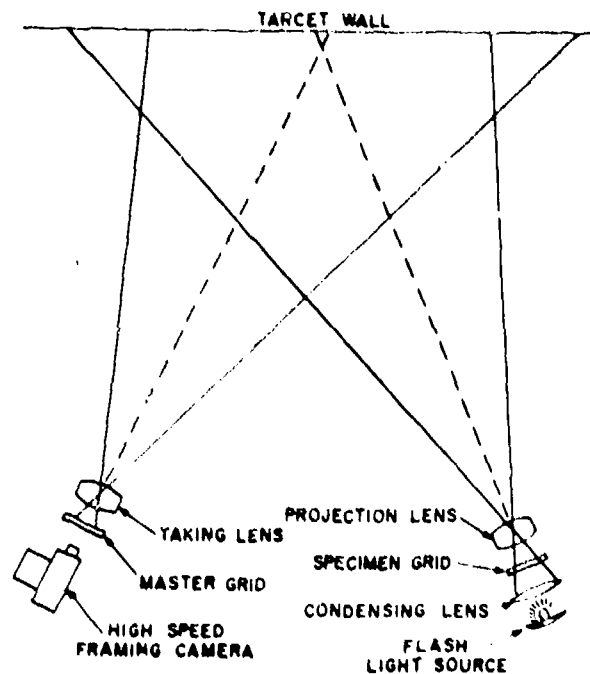the fringe produced on a reference structure. The resulting

105

Figure A.2. Optical diagram of moiré apparatus.

"map" of fringe location can be used to deduce panel dis-
placement. This technique was used in Reference 2.

In Reference 2, we also developed an analytical model
for the reduction of fringe data. That model was so compli-
cated that we did not find it useful. In this program the
apparatus was rearranged so that the moire triangle defined
in Reference 2 became isosceles. The analysis consequently
became much simpler. A computer program was written and used
for reducing all the displacement data in the report except
Shot FTC2.

Figure A.3 illustrates the geometry and defines the
geometric variables in the present moire triangle. The
equations of the principal lines S_RP_O and S_LP_O are

$$S_RP_O \qquad y = \frac{R}{S}\, x \qquad\qquad (A1)$$

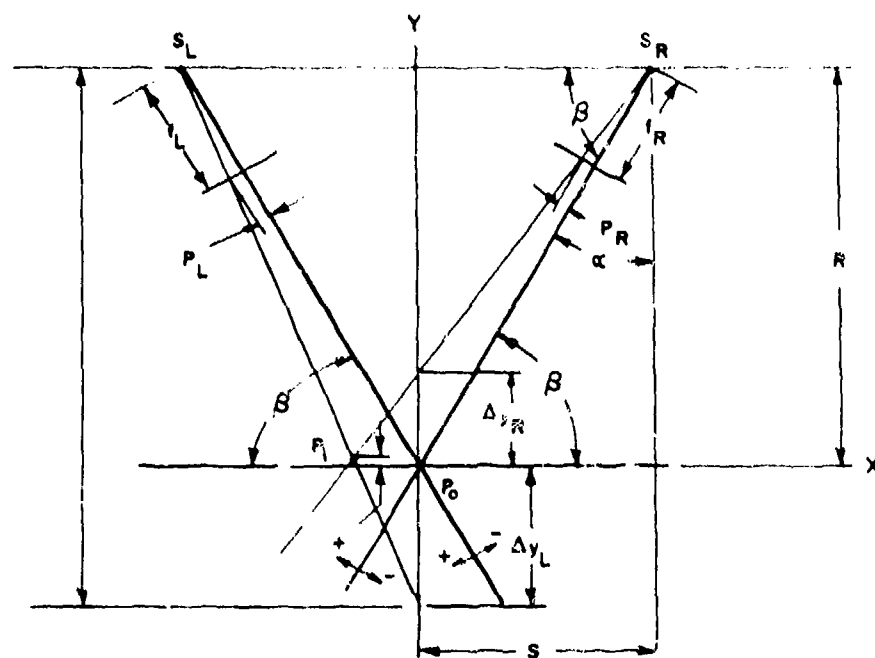$$S_LP_O \qquad y = -\frac{R}{S}\, x \qquad\qquad (A2)$$

Figure A3. New moiré triangle and definition of symbols. S_L and S_R are the source and convergence points, repsectively. The system is set up so that point P_o is on the target.

107

The equation of any other line from S_R is

$$y = m_R x + b_r \qquad \text{(A3)}$$

$$= \frac{\cot \alpha + P_R/f_R}{1 - (P_R/f_R)\cot \alpha} x + R - S \left(\frac{\cot \alpha + P_R/f_R}{1 - (P_R/f_R)\cot \alpha} \right) \qquad \text{(A4)}$$

The equation of any other line from S_L is

$$y = m_L x + b_L \qquad \text{(A5)}$$

$$= \frac{\cot \alpha + P_L/f_L}{P_L/f_L \cot \alpha - 1} x + R + S \left(\frac{\cot \alpha + P_L/f_L}{P_L/f_L \cot \alpha - 1} \right) \qquad \text{(A6)}$$

Various fringes were defined by the intersections of Equations A3 and A5. We designated the fringe through P_o as "fringe 0". Thereafter, fringe N was defined by $i_R - i_L$, where i_R and i_L are, respectively, integers equal to f_R and f_L divided by the Ronchi ruling pitch p. Note that fringes for which N >0 always lie above the x axis. The x and y coordinates of the fringe are given by

$$x_i = \frac{b_L - b_R}{m_R - m_L} \qquad \text{(A7)}$$

$$y_i = m_R x_i + b_R \qquad \text{(A8)}$$

Given N, β, R, f_R, f_L, and p, Equations A7 and A8 can be used to generate points on the fringes. These points were stored in a table and accessed by fringe number. Experimental data consisted of (x_i, N) pairs, where x_i was the position of fringe

N on the target surface. The program interpolated in the table
to find the corresponding y_i values. Absolute values and
values relative to the pre-impact panel shape were tabulated.
The program also translated the x coordinates to origins
centered on the tank center and on the impact point.

A.3. PRESSURE TRANSDUCERS

Pressure pulses produced in the water by impact were
measured by piezoelectric gauges. Previously (Reference 2),
we had used PCB Model 101A04 quartz transducers. These were
mounted in aluminum caps threaded onto 20-mm-diameter galvanized
steel water pipes and inserted into the tank from the top.
(The tips of the transducers protruded slightly from the caps
to eliminate the possibility of air bubble formation). The
closest of the transducers was about 30-cm away from the impact
point. These transducers performed well for frequencies less
than about 20 kHz.

The PCB gauges allowed us to compare experimental and
predicted pressure histories deep within the tank. Agreement
was satisfactory. However, the most difficult and important
aspect of the pressure prediction was to account for the
influence of the tank boundaries in the vicinity of the impact
site. Similar gauges were used in this program for the T_4
and T_5 transducer stations. However, for the T_1, T_2, and T_3
stations there were several reasons why the quartz transducer
assemblies were considered inadequate. Frequency components
approaching one megahertz were anticipated in this region,
and these could not be resolved with the PCB gauges. We
wanted to have the sensing element as near to the panel as
possible, and the bulky size of the quartz gauges made this
awkward. Finally, failure of the target panel was known to
be very sensitive to the pressure and flow in this region;
and emplacement of a large gauge and support structure would
alter these conditions.

High-frequency response is best achieved by minimizing the size of the sensing crystal and its mechanical support. Since the speed of sound in these materials is typically 6-mm/µs, dimensions of ∿3 mm or less would assure good frequency response up to one megahertz. This is only possible if the crystal is suspended in the water.

If the crystal is suspended in the water, it will be subjected to hydrostatic stress. This is not the usual application for piezoelectric crystals. The relevant piezoelectric equation is

$$P_i = d_i P \qquad\qquad (A9)$$

where P is hydrostatic pressure, p_i is the polarization vector, and d_i is the piezoelectric coefficients. Unlike the usual piezoelectric coefficients, d_{ijk}, that comprise a third rank tensor, the d_i in Equation A9 comprises a vector (since it relates a vector to a scalar). Elementary symmetry considerations show that $d_i = 0$ for any lattice with a center of symmetry. This includes quartz as well as the amorphous piezoelectric materials. In fact, the only common piezoelectric material for which $d_i \neq 0$ is tourmaline, whose point group is 3-m (trigonal). Further consideration of crystal symmetry shows that $d_1 = d_2 = 0$ for this point group, so d_i is in the direction of the triad axis[5]. The handbook value[6] of d_3 for tourmaline is -2.16 x 10^{-12} coulomb/newton.

We were only able to locate one domestic source for transducer quality tourmaline crystals: Susquehana Instruments in Havre de Grace, Maryland. This company assembled the electrical components to our specifications and calibrated the gauges.

The gauge design is shown in Figure A4. The sensing element was a tiny tourmaline crystal, typically 1-mm-thick. Twin electrical leads 0.2-mm in diameter were attached to the
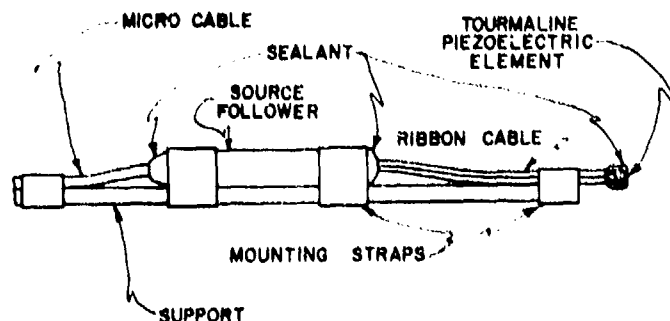
Figure A.4. Schematic drawing of gauge design.

crystal with conducting epoxy. This area was sealed with
insulating epoxy.   The twin leads ran 40-mm, where they
entered a piece of heat-shrinkable tubing. The opening was
sealed with an RTV compound. After another 30-mm, the leads
were attached to a commercial voltage follower (PCB Model
401M26). The unit converted the high impedance crystal voltage
to 100Ω output impedance. The rear of the amplifier was
connected to a coaxial cable. The shrink tubing closed and
was sealed onto this cable. The cable conducted the signal
out of the water to a recording oscilloscope. The main body
of the gauge was attached to a 6-mm copper tube; but the
crystal and 40-mm-long twin cable were free in the water,
facing the impact site. Calibration factors ranged from
0.96 bar/mV to 1.29 bar/mV.

REFERENCES

1. Hydrodynamic Ram Seminar, S. J. Bless and A. J. Holten, eds., AFFDL-TR-77-32, JTCG/AS-77-D-002, May 1977.

2. S. J. Bless, J. P. Barber, P. F. Fry, and R. K. Newman, Studies of Hydrodynamic Ram Induced by High Velocity Spherical Fragment Simulators, AFML-TR-77-11, June 1977.

3. R. J. Roark and W. C. Young, Formulas for Stress and Strain, 5th Edition, McGraw Hill, 1975.

4. See, for example, High Velocity Impact Phenomena, R. Kinslow, ed., Academic Press, 1970.

5. J. F. Nye, Physical Properties of Crystals, Oxford Clarendon Press, 1969.

6. W. P. Mason, "Properties of Transducer Materials," in American Institute of Physics, Handbook, Third Edition.